Study of the synthesis machanisms and optical properties of ZnO nanomaterials obtained by supercritical fluids route

Evgeniy Ilin

université de BORDEAUX

THÈSE

PRÉSENTÉE A

L'UNIVERSITÉ de BORDEAUX

ÉCOLE DOCTORALE DES SCIENCES CHIMIQUES

Par Evgeniy ILIN

POUR OBTENIR LE GRADE DE

DOCTEUR

SPÉCIALITÉ : Physico-Chimie de la Matière Condensée

Study of the synthesis mechanism and optical properties of ZnO nanomaterials obtained by supercritical fluids route

Sous la direction de Véronique JUBERA et Cyril AYMONIER

Soutenue le : 20 novembre 2014

Devant la commission d'examen formée de :

M. MAGLIONE, Mario	Directeur de Recherche, ICMCB, France	Président
M. IVERSEN, Bo Brummerstedt	Professeur, Aarhus University, Denmark	Rapporteur
M. BOUTINEAU, Philippe	Professeur, Université de Clermont Ferrand, France	Rapporteur
Mme. CHANEAC, Corinne	Professeur, Université Pierre et Marie Curie, France	Examinatrice
Mme. JUBERA, Véronique	Maître de Conférences, ICMCB, France	Co-Directeur de Thèse
M. AYMONIER, Cyril	Chargé de Recherche, ICMCB, France	Co-Directeur de Thèse

Acknowledgements

I would like to thank Mario Maglione, director of the institute for giving me the opportunity to do this investigation using all the ICMCB facilities.

I would like to aknowledge the tribunal members for their reading of this manuscript.

In the last three years of my Ph.D. research project, I have had the help and support of many people inside and outside of my research institution - ICMCB. These people should be acknowledged. All of them I have met on the way of my Ph.D. project in Bordeaux. It is necessary to mention that, I have sensed an interest in my life and work and their encouragement for me to succeed from everyone.

First and foremost, I would like to thank to my Ph.D. advisors which have invited me to this project and allowed me to work in ICMCB. I thank to my first advisor Dr. Veronique Jubera for her guidance and support. During these three years, I had been through several difficulties concerning my life in France and also my laboratory work. I am absolutely sure that without Dr. Jubera's encouragements and helps, it would be very difficult for me to go through these moments. I would like to especially note her patience which she has demonstrated during all this period. I also would like to thank to my second supervisor Dr. Cyril Aymonier for his supervising and support, and for many interesting and inspirational scientific discussions we have had. I have to say that Dr. Cyril Aymonier will be always in my memory as a brilliant example how to organize scientific project efficiently.

I would like to thank to all the people with whom I have had scientific collaboration during my Ph.D. Thanks to Samuel Mare, Alexandre Fargues and Alain Garcia for their support concerning my work on the equipments. Thanks to Eric Lebraund, Stanislav Pechev, Sonia Buffiere, Philippe Dagault, Stephane Touline, Patrick Martin, Mathieu Dumerq, Mark Dussaize, Michel Couzi, Helen Debeda, Sylvie Lacombe, Michel Le Bechec and Ross Brown for their collaboration concerning the physical methods I have used and tests systems which have been applied in this project.

I also would like to thank to all students and postdocs form groups of Dr. Cyril Aymonier and Dr. Thierry Cardinal for the warm welcome and pleasant stay during this time in Bordeaux.

Finally, I would like to thank to my friends whom I have met in Bordeaux, for this time which we have spent together, it is unforgettably, and you all are a part of my hart forever.

Bordeaux, France, November 2014 **Dr. Evgeniy ILIN**

Etude des mécanismes de synthèse et propriétés optiques de nanomatériaux de ZnO obtenus par voie supercritique

Les recherches portant sur l'oxyde de zinc (ZnO) à l'échelle nanométrique suscitent un grand intérêt en raison des propriétés uniques de ce matériau notamment dans les domaines de l'optique (émission ultraviolette ou visible), des capteurs chimiques, de la piézo-électricité[1]. ZnO est un candidat potentiel en tant qu'émetteur UV au même titre que GaN; il possède en effet une énergie de piégeage de l'exciton de 60 meV, ce qui permettait d'envisager son utilisation en tant que matériau à gain avec une réduction du seuil laser et une meilleure efficacité[2].

Ce travail de doctorat est dédié à la synthèse de nanoparticules de ZnO par voie supercritique, l'objectif étant d'obtenir une émission purement excitonique de ce composé en vue d'une utilisation dans le domaine de la photonique (source UV) mais aussi de le tester en tant que capteur chimique ou encore pour ses propriétés de photocatalyse.

Le manuscrit est divisé en quatre parties. Le chapitre I est un chapitre bibliographique dédié à la description des propriétés optiques de ZnO sur la base de la structure de ce semi-conducteur direct. ZnO est un semiconducteur de large bande interdite égale à 3,37 eV. A température ambiante et pression atmosphérique il cristallise selon le groupe d'espace $P6_3mc$ dans une maille de type würtzite de paramètre a=0,325 nm et c= 0,523 nm[3]. Les différentes voies de synthèses recensées sont décrites avec un focus particulier sur la voie supercritique qui reste à ce jour très peu exploitée.

[1]H. D. Sun et al. Appl. Phys, Lett., 2001, 78, 2464.
L. Vayssierer, Adv. Mater., 2003, 15, 464.
M. H. Huang et al. Adv. Mater., 2001, 13, 113.
H. D.Yu et al. JACS 2005, 127, 2378.
Z. L. Wang, J. Physics-Condens. Mat., 2004.16, R829.
[2]W. D. Yuet al. Cryst. Grow.& Des., 2005, 5, 151.
[3]M. L. Fuller, Science, 1929, 70, 196.

A l'échelle nanométrique une large variété de morphologies peut être obtenue tels que des nanotubes, bâtonnets, anneaux, tétrapodes comme illustrés sur la Figure 1[1,2].

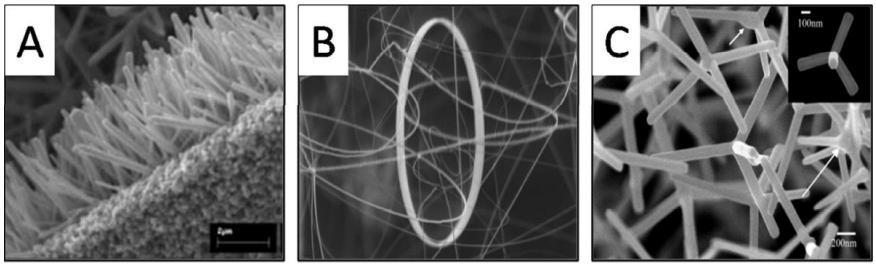

Figure 1- Diverses variétés de nanomatériaux de composition ZnO

Les propriétés optiques de matériaux massifs, nano-structurés ou pulvérulents ont été largement regardées. A température ambiante, ceux-ci présentent la majeure partie du temps une large émission dans le domaine du visible attribuable à l'existence de défauts tels que la présence d'impuretés, des lacunes d'oxygène ou des atomes de zinc en sites interstitiels. La profondeur des niveaux pièges associés a fait l'objet de calculs comme illustré sur la Figure 2.

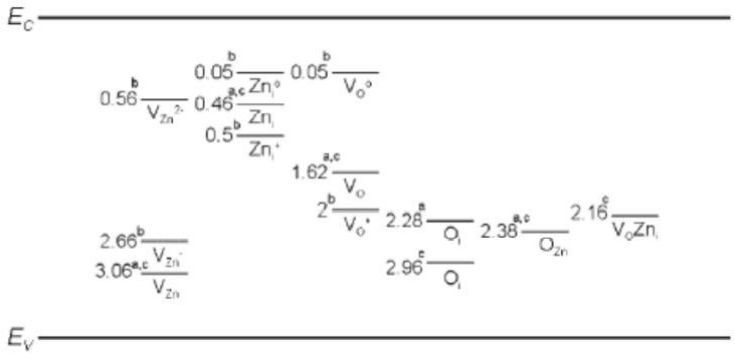

Figure 2- Localisation de niveaux pièges dans la bande interdite du ZnO[4].

Les matériaux massifs ou obtenus à partir de synthèses par voie physique ou chimique en phase vapeur présentent une émission ultraviolette fine dite émission excitonique liée à la recombinaison de paires électron-trou créées sous irradiation[5]. Des mesures plus fines à basse température laissent apparaître un spectre d'émission structuré composé de raies fines liées à l'existence de défauts

[4]A. B. Djurišić, et al. Ad. Funct. Mater., 2004, 14, 856
[5]C. F. Klingshirn, Semiconductor Optics, Third Edition., Springer, Heidelberg, 2006.

donneurs ou accepteurs d'électrons référencés en tant que centres D^0X, AX et au couplage de ces transitions avec des modes de vibration de phonons optiques[6]. Une mise en relation des propriétés d'émission avec les voies de synthèse clôture cette première partie.

Le chapitre II vise à décrire la méthodologie mise en place pour augmenter la production des particules de ZnO par voie supercritique en passant de l'échelle micro- à l'échelle milli-fluidique[7]. Les particules sont obtenues à partir d'acétylacétonate de zinc, de trioctylphosphine (TOP) et de H_2O_2 en milieu éthanol/eau (250°C, 25 MPa). Quatre types de réacteurs ont été utilisés, leur différence provenant de la taille des capillaires interne et externe permettant l'injection des réactifs dans la chambre réactionnelle (Figure 3).

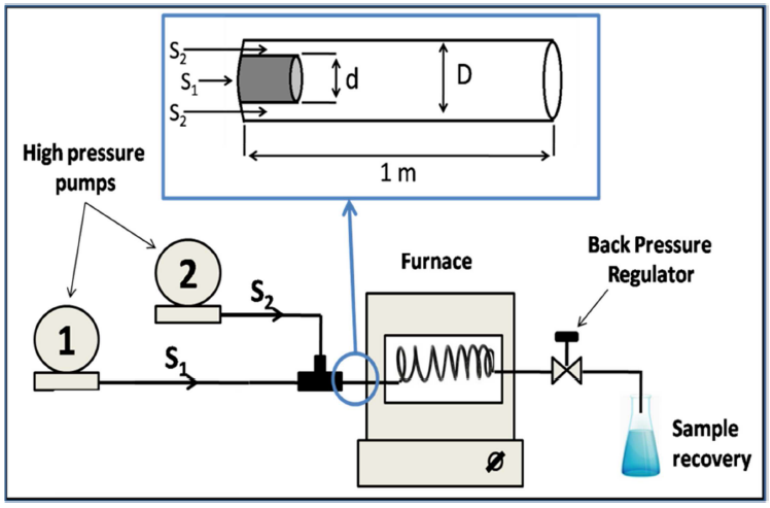

Figure 3- Dispositif expérimental

A ce stade, l'obtention de matériau en quantité suffisante permet la mise en œuvre de tout un panel de caractérisations physico-chimiques telles que la diffraction des rayons X, les spectroscopies infrarouge et Raman, l'XPS ainsi que les microscopies à balayage et à transmission. Le contrôle des différents paramètres de synthèse a permis l'obtention de particules de ZnO de symétrie hexagonale (type Würtzite). Les nanoparticules de ZnO sont enrobées de fonctions organiques

[6]R. Hauschild et al. Phys. Status Solidi C, 2006, 3, 976.
[7]E. Ilin, J. Mater. Chem. C, 2013, 1, 5058

telles que –OH, -CH_2, COO-, C-O, C=O et P=O dont l'origine provient de réactifs de départ (TOP et acétylacétonate de zinc). Leur quantité a été évaluée par ATG et représente environ 6% en masse. Les particules présentent différentes morphologies en fonction des dimensions des réacteurs de synthèse et des concentrations en réactifs mais possèdent les mêmes propriétés optiques avec une émission purement excitonique UV. Selon l'interaction entre le TOP et les nuclei en présence, des morphologies purement sphériques ou des mélanges de populations de particules sphériques et de bâtonnets ou de triangles sont obtenues (Figure 4).

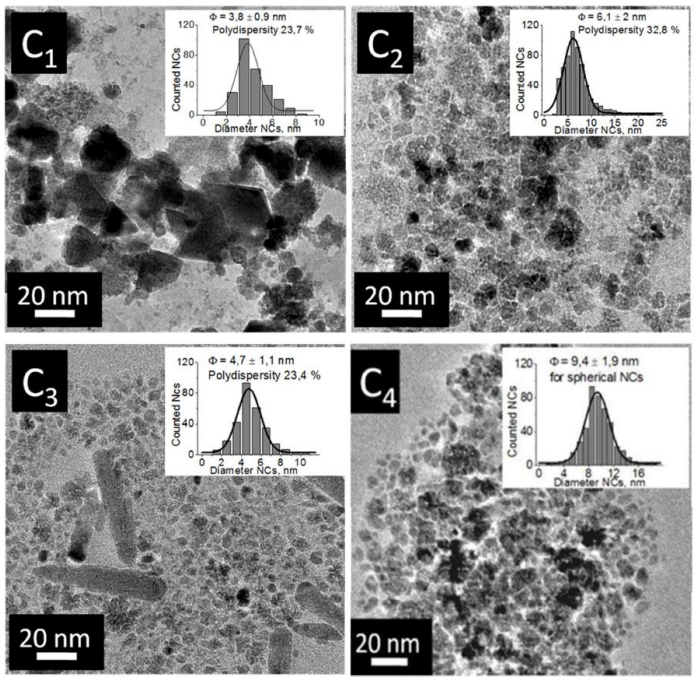

Figure 4- Images MET obtenues sur des particules synthétisées dans les différents réacteurs.

Le régime hydrodynamique des réacteurs utilisés est caractérisé par deux facteurs qui sont le rapport de vitesse des fluides, R_H et le nombre de Reynolds R_e. R_H détermine la forme du flux interne et peut être calculé. Il détermine ainsi le type de régime dans lequel le système se trouve (Figure 5, Tableau 1).

Figure 5- Géométrie des flux internes dans les réacteurs en fonction de la valeur de R_H.

Tableau 1 - Paramètres hydrodynamiques des réacteurs testés

Scale	Reactor	Flow rate ratio	R_H	R_e	ZnO NCs morphology
Micro	C_1	2.75	1.22	45	Spherical, triangles
	C_2	2.74	0.44	57	Spherical
	C_3	2.78	0.40	132	Spherical, nanorods
Milli	C_4	2.78	0.85	32	Spherical

Les effets de concentrations en H_2O_2 ont aussi été étudiés. Ainsi, la morphologie sphérique est préférentiellement obtenue pour des concentrations importantes en H_2O_2, les faibles quantités de ce réactif entrainant la précipitation de particules triangulaires ou de bâtonnets. La taille (5-20 nm) et la morphologie peuvent finalement être contrôlées par le régime hydrodynamique et la concentration en peroxyde. Dans tous les cas, aucune émission visible liée à la présence potentielle de défauts de cœur ou de surface n'est détectée[7].

Le mécanisme de formation des nanoparticules est décrit dans le chapitre III. Le temps de séjour dans le réacteur est le paramètre clé qui a été regardé pour comprendre la formation et la croissance des nuclei de ZnO. La compréhension du mécanisme est aussi primordiale au regard des propriétés optiques obtenues. La structure, la morphologie et les propriétés de surface ont été étudiées et caractérisées par DRX, Raman, HR MET, ATG, FTIR et XPS. Les nanoparticules obtenues à l'issue de temps de séjour de 30 et 40s (séjour long) dans le réacteur sont des nano-cristaux de ZnO de symétrie hexagonale. En revanche pour des temps plus courts de 6 à 10s, les matériaux obtenus sont de type ZnO_2 de symétrie cubique à faces centrées (Figure 6). Dans tous les cas, les particules sont sphériques et leur taille augmente avec le temps de séjour dans le réacteur. Les particules de type ZnO_2 se décomposent au-delà de 195°C ce qui a été confirmé par ATG et DRX.

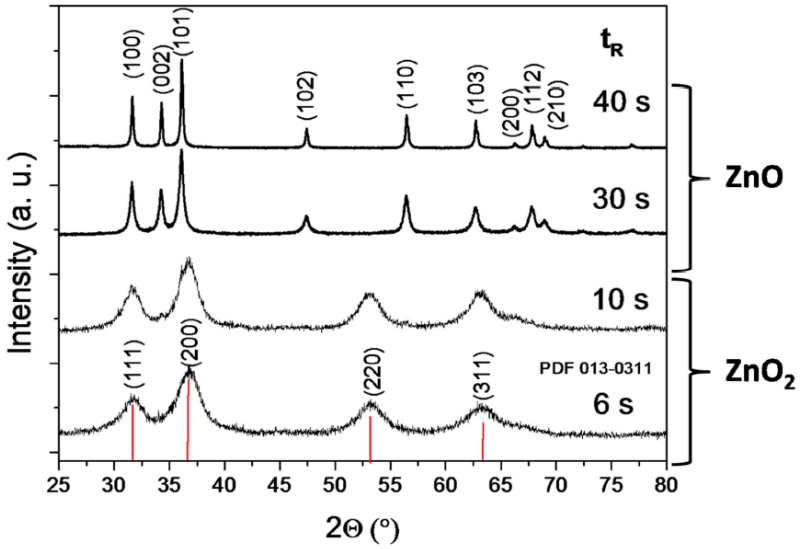

Figure 6 - Evolution des diffractogrammes de rayons X en fonction du temps de séjour dans le réacteur.

Le peroxyde de zinc apparait comme un précurseur à la formation de ZnO qui croit après décomposition de celui-ci. Les profils de température dans le réacteur ont été simulés au moyen d'une méthode numérique de traitement du modèle de Graetz-Nusselt[8].

$$\rho c_v \frac{\partial T}{\partial t} + [\rho v c_v \nabla T] = \nabla(\lambda \nabla T) - T\left(\frac{\partial p}{\partial T}\right)_p (\nabla . v) + \phi_\mu \qquad \text{(eq. 1)}$$

Les différentes techniques de caractérisation employées ont montré que les particules de ZnO formées possèdent un état de surface de type ZnO_2 qui neutralise les défauts de surface potentiels normalement à l'origine d'émission visible d'objets de cette taille obtenus à basse température par des voies de chimie douces. Le mécanisme de formation des nanoparticules peut ainsi être illustré sur le schéma de la Figure 7.

[8]Y. Roig. Ph.D. thesis, University of Bordeaux 1, 2012.

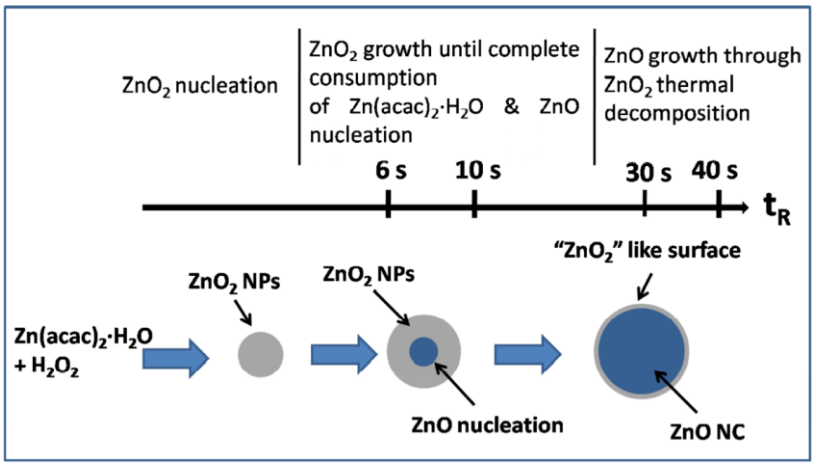

Figure 7- Schéma de croissance des nanoparticules de ZnO à partir de la décomposition du peroxyde de zinc.

Une synthèse réalisée sans H_2O_2 ou encore un traitement thermique des particules à 350°C laisse apparaître, en plus de l'émission ultraviolette attendue, une émission visible prouvant le rôle de H_2O_2 et de la couche de surface stabilisée sur les nanoparticules dans la non-émission de défauts. La microscopie électronique à transmission haute résolution montre des particules très bien cristallisées ce qui explique l'observation d'une émission UV unique.

La compréhension de l'émission UV passe par des mesures hautes et basses températures. Cette étude est décrite dans le chapitre IV. Une comparaison approfondie est faite avec les propriétés de diverses particules et couches décrites dans la littérature mais aussi à partir de l'acquisition de spectres de luminescence réalisés sur monocristaux (matériau prêté par le CELIA).

Les mesures obtenues à basses températures (hélium liquide) montrent une émission UV structurée caractéristique de la recombinaison électron-trou. Aucune émission n'est détectée dans le domaine du visible (Figure 8).

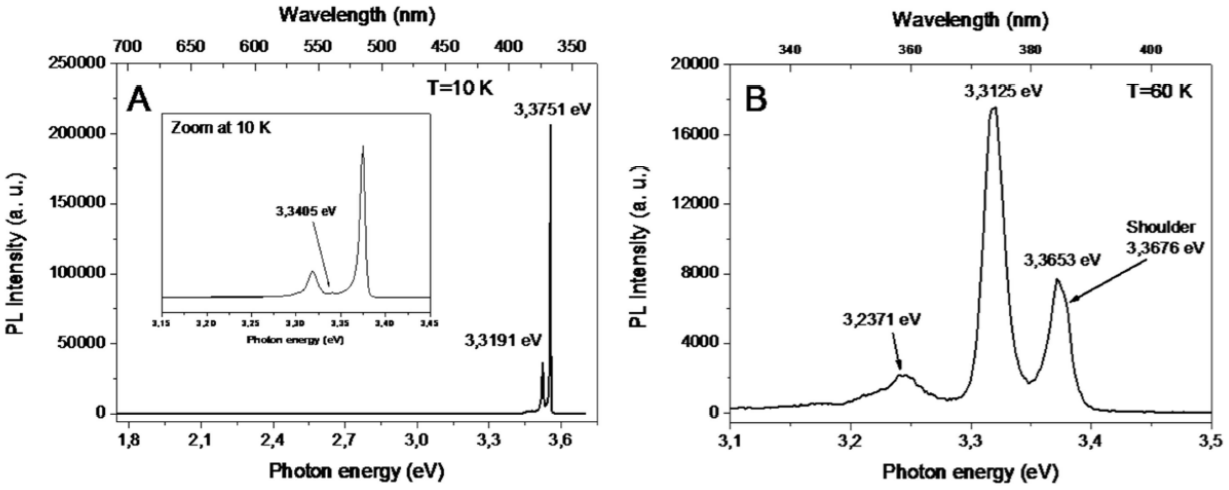

Figure 8 - Luminescence ultraviolette des nanoparticules de ZnO.

Les différents pics ont été attribués à des excitons libres nommés FX_A, FX_B et à leur couplage avec des modes de vibration enregistrés par spectroscopie Raman : le mode de phonon optique E_{2high} de ZnO ou les modes de vibrations, $E_{2high}+A_1(LO)$ et/ou $2E_{2high}$[9]. Aucune émission attribuée à des excitons liés n'a été observée: cette émission est généralement due à l'existence de défauts accepteurs ou donneurs du ZnO. Une augmentation en température révèle un meilleur couplage avec les modes de vibrations, les pics d'émission associés étant alors plus intenses (Figure 8B).

La spectroscopie des particules obtenues pour des temps de séjour faibles (particules de type ZnO_2) présente la même répartition spectrale que celle obtenue pour des temps longs. En effet, ces particules contiennent vraisemblablement un cœur de ZnO non détectable en DRX en raison de sa taille. La luminescence de ZnO si existante, serait alors réabsorbée par le ZnO_2 qui possède une bande interdite plus petite. L'évolution de l'émission a été enregistrée en fonction de la température. La Figure 9 montre ainsi le décalage des pics d'émission vers les basses énergies.

[9]T. C. Damen et al. B. Tell, Phys. Rev., 1966, 142, 570.
C. A. Arguello et al. Phys. Rev., 1969, 181, 1351.
J. M. Calleja et al. Phys. Rev. B, 1977, 16, 3753.
R. Ciscó et al. Phys. Rev. B, 2007, 75, 165202.
R. Hauschild et al. Phys. Stat. Sol., 2006, 3, 976.
T. S. Jeong et al. J. Appl. Phys., 2014, 115, 053521.
Y. S. Park et al. Phys. Rev., 1966, 143, 512.

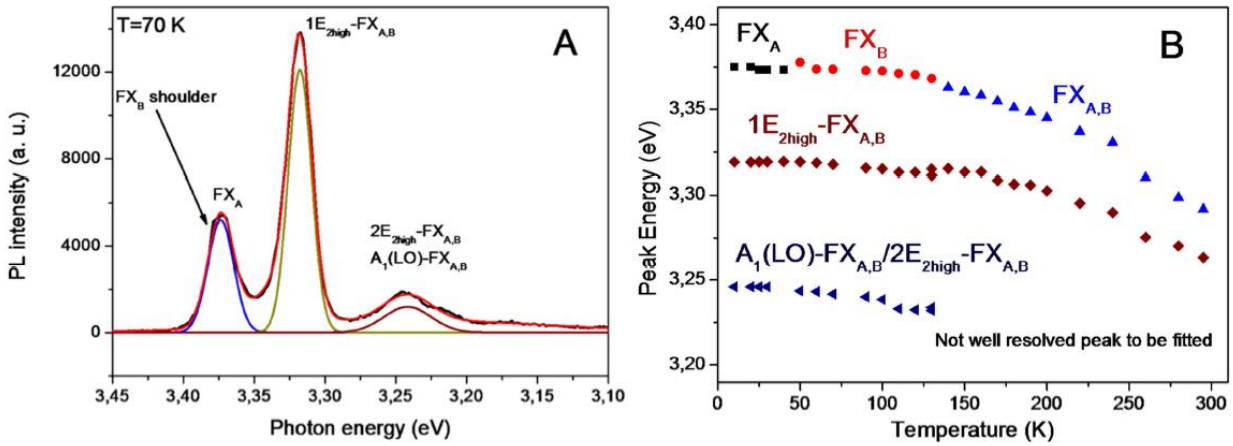

Figure 9 - Analyse des spectres d'émission en fonction de la température

Il a aussi été possible de calculer la variation de la bande interdite du matériau avec la température à partir de la formule de Varshni[10]. Le résultat est illustré ci-dessous :

$$E_g(T) = E_g(0) - \frac{\alpha T^2}{T + \beta} \qquad \text{(eq. 2)}$$

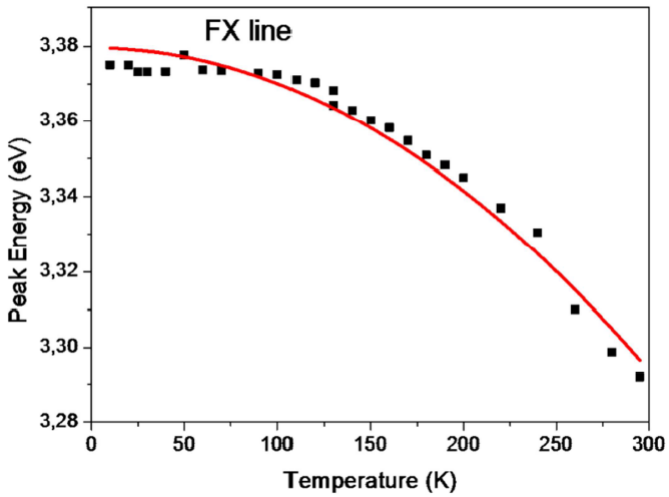

Figure 10 - Ajustement de la position de l'exciton libre F_{XAB}, avec la formule de Varshni

[10]Y. P. Varshni, Physica, 1967, 34, 149.

Les mesures de durée de vie réalisées en collaboration avec le CELIA confirment la nature d'excitons libres des pics enregistrés mais une étude plus approfondie sera nécessaire à une exploitation complète des données recueillies.

Pour conclure, la voie de synthèse supercritique choisie a permis d'obtenir des quantités de nanoparticules de ZnO bien cristallisées et ne présentant qu'une émission ultraviolette. L'existence d'une couche de ZnO_2 en surface de ces particules permet d'obtenir un matériau de composition vraisemblablement stœchiométrique en oxygène et dont les défauts de surface potentiellement émetteurs sont neutralisés/passivés. Les propriétés optiques résultantes sont dues à la recombinaison de paires électron-trous (excitons libres) et à leur coupage avec des modes de vibrations. Le schéma proposé ci-dessous permet de repositionner les propriétés optiques des nanocristaux synthétisés en régime micro- milli-fluidique parmi celles de matériaux massifs ou nano-structurés trouvés dans la littérature[11].

[11]T. Makino et al. Appl. Phys. Lett., 2000, 76, 3549.
S. W. Jung et al. Appl. Phys. Lett., 2002, 80, 1924.
C. H. Ahn et al. Appl. Phys. Lett., 2009, 94, 261904.
W. Y. Liang et al. Phys. Rev. Lett., 1968, 20, 59.
W. I. Park et al. Appl. Phys. Lett., 2003, 82, 964.
W. I. Park et al. J. Mater. Res., 2001, 16, 1358.
D. C. Reynolds et al. Phys. Rev. B, 1998, 57, 12151.
D. W. Hamby et al. J. Appl. Phys., 2003, 93, 3214.
W. I. Park et al. J. Electronic Matter., 2001, 30, L32.
W. I. Park et al. J. Appl. Phys. Lett., 2001, 79, 2022.
V. Kharanovskyy et al. Nanotechnol., 2013, 24, 215202.
M. A. Borysiewicz et al. J. Luminescence, 2014, 147, 361.
R. Zhang et al. Sol. St. Sci., 2009, 11, 856.
D. C. Reynolds et al. Phys. Rev. B, 1999, 60, 2340.
S. F. Chichibu et al. J. Appl. Phys., 2003. 93, 756.
H. J. Ko et al. Appl. Phys. Lett., 2000, 76, 1905.
J. Grabowska et al. Phys. Rev. B, 2005, 71, 115439.
C. Z. Xing et al. Chem. Phys. Lett., 2011, 515, 132.
J. S. Reparaz et al. Appl. Phys. Lett., 2010, 96, 053105.
S. L. Chen et al. Appl. Phys. Lett., 2013, 102, 121103.

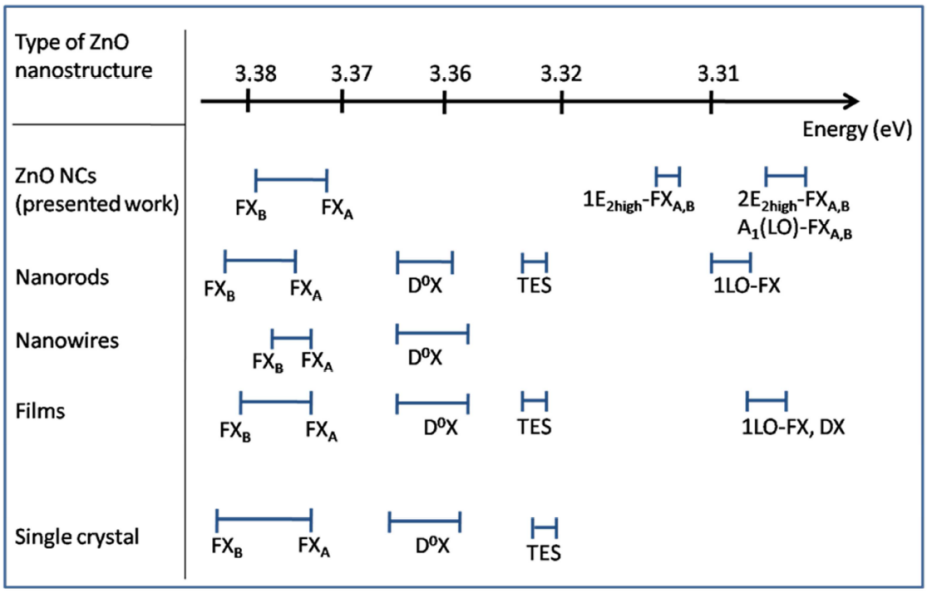

Figure 11 - Schéma positionnant les énergies d'émission UV des différents centres répertoriés dans différents matériaux.

Le positionnement des raies observées indique clairement que la voie micro- milli-fluidique optimisée dans le cadre de ce travail pour l'obtention de nanocristaux de ZnO donne des objets aux propriétés optiques uniques.

De premiers tests de photocatalyse (collaboration IPREM Pau) sont en cours de réalisation et permettront de déterminer l'efficacité de ces objets en termes de dégradation de composés organiques à l'état gazeux ou mis en solution.

Table of contents

General introduction

Zinc oxide (ZnO) nanomaterials attract a great interest accelerating research in this field in recent years due to their unique properties and potential applications in ultraviolet (UV) light emitters, optochemical sensors, spin electronics, transparent electronics and piezoelectronic devices [1-5]. ZnO has been proposed to be a UV emitting phosphor more efficient than GaN thanks to its larger excitonic binding energy of 60 meV, which leads to reduce UV lasing threshold and yields higher UV emitting efficiency at room temperature [6]. According to this, design of new nanostructured ZnO materials is one of the critical points in Materials Science for the development of applications based on their peculiar properties.

This PhD thesis is devoted to a new supercritical fluids based strategy for synthesis of UV-emitting ZnO nanocrystals which are very promising for broad applications in photonics but also in optochemical sensing or photocatalysis. The manuscript is divided in four chapters as described below.

Chapter I is devoted to a literature survey. Before listing some general properties of ZnO material concerning its crystal structure and energy band gap properties, three synthetic approaches which were developed for the fabrication of ZnO nanostructures are discussed and the associated optical properties are described. Nature of visible as well as the UV luminescence is exposed.

Chapter II describes the scale up of the supercritical fluids based set up, developed for the continuous synthesis of ZnO nanocrystals from micro- up to millifluidic reactors [7-8]. At this stage, the aim is, to obtain a larger quantity of these nanocrystals in order to deeper characterize

their physico-chemical properties. Then the morphology control of these nanocrystals playing with different operating parameters is shown.

Chapter III is devoted to the evaluation of ZnO nanocrystals formation mechanism in the supercritical fluids based approach. ZnO nanocrystals formation was investigated as a function of the residence time in our supercritical fluids based reactor in order to understand the nucleation and growth of the material. ZnO NCs formation mechanism is necessary to better understand the optical properties of these objects.

Comprehensive photoluminescence investigations carried out for ZnO nanocrystals are demonstrated in Chapter IV. Room and low temperature measurements are described and compared to the emission of several types of ZnO particles and crystals to fully attribute the specific lines which constitute the structured emission spectrum. The photoluminescence investigation is completed by decay time characterizations performed in collaboration with CELIA.

Finally, the progress concerning the fabrication of high quality ZnO nanocrystals, deep investigation of their physico-chemical characteristics and their optical properties are summarized in “General conclusion” section. This section also provides potential applications for this nanomaterial.

References

1. K. Nomura et al. Science, 2003, 300, 1269.
2. R. Könenkamp et al. Appl. Phys. Lett., 2004, 85, 6004.
3. M. S. Wang et al. Mater. Chem. Phys., 2004, 84, 228.
4. S. J. Pearton et al. Semicond. Sci. Technol., 2004, 19, R59.
5. Y. Ushio et al. Sens. Actuators A, 1994, 17, 221.
6. P. Yang et al. Adv. Mater. (Weinheim, Ger), 2002, 12, 323.
7. Y. Roig et al. Angew. Chim. Int. Ed., 2011, 50, 12071.
8. E. S. Ilin et al. J. Mater. Chem. C, 2013, 1, 5058.

Chapter I

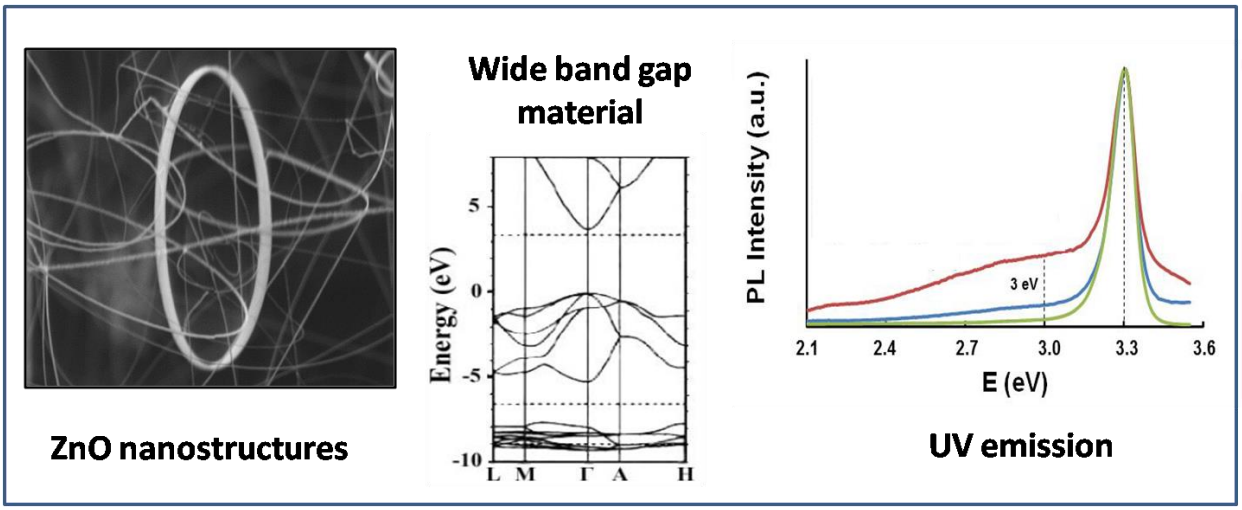
ZnO nanostructures
Wide band gap material
Energy (eV)
5
0
-5
-10
L M Γ A H
PL Intensity (a.u.)
3 eV
2.1 2.4 2.7 3.0 3.3 3.6
E (eV)
UV emission

I. Zinc oxide

Introduction

ZnO is a II-IV wide direct band gap semiconductor with a large band gap energy of 3.37 eV, which makes ZnO suitable for short wavelength optoelectronic applications. On the other hand, the exciton binding energy of ZnO is high and equal to 60 meV [1], which ensures an efficient excitonic emission at room temperature. Moreover, this binding energy in ZnO is much higher than in GaN which is 25 meV. ZnO can be a possible alternative to GaN in optoelectronic applications.

At nanoscale ZnO can be obtained with a large variety of morphologies, such as nanorods [2], nanowires [3], nanotubes [4], nanorings [5] and tetrapods [6] depending on the synthetic method as illustrated in Figure I-1.

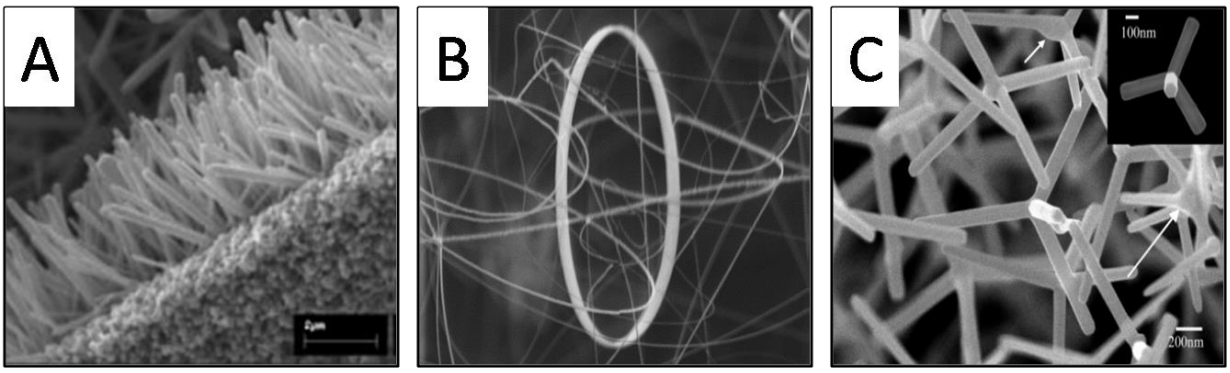

Figure I-1. Morphologies of ZnO nanostructures: nanorods (A), nanorings (B) and tetrapods (C).

As it is well known, all the applications of this material are originated from its physico-chemical properties. Therefore, in order to know about ZnO characteristics, details concerning structural, electronic and optical properties are introduced in this chapter.

I-1. Crystal structure

ZnO exists in three different crystal structures, such as: (i) rocksalt, a cubic structure with *m3m* symmetry [7], (ii) blende, a cubic structure with *43m* symmetry [8] and (iii) würtzite, a hexagonal structure that belongs to *6mm* symmetry [9] (Figure I-2).

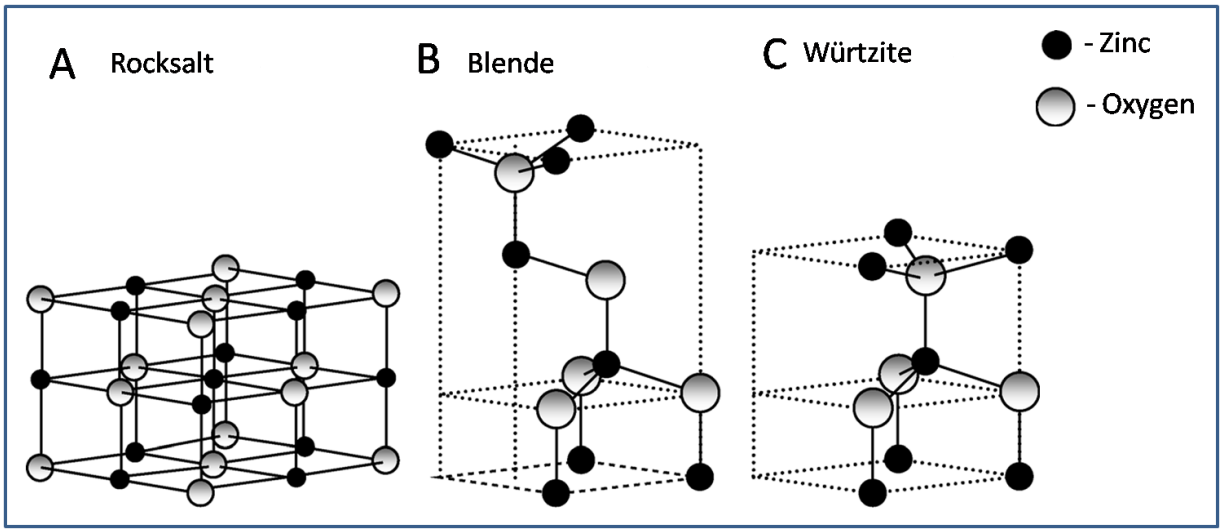

Figure I-2. ZnO crystal structures: rocksalt (A), blende (B) and würtzite (C).

Among them, ZnO is crystallizing in the würtzite structure at ambient temperature and pressure. Würtzite phase belongs to the space group $P6_{3mc}$; the lattice parameters are a=0.3249 nm and c=0.5229 nm. This structure can be described as a succession of-planes composed of tetrahedral coordinated Zn^{2+} ions in a closed packed structure. The volume occupied by the atoms of Zinc and Oxygen is only about 52 % in the lattice and leaving free empty spaces around 2.85 $Å^3$. It could be also noted that this space can be occupied by other transition metals atoms such as Co^{2+} [10], Mn^{2+} [11]; V^{2+}, Al^{3+} [12] when they are introduced by the synthetic methods. The doping of würtzite structure has a strong influence on ZnO conducting and optical properties.

I-2. Electronic structure and general optical properties

ZnO as a semiconducting material has a wide band gap. Electronic band gap structure of ZnO material has been calculated by a number of researchers [13-14]. Figure I-3 shows the result of band gap structure calculations which were based on the quantum methods such as Local Density Approximation and incorporating atomic self-interaction corrected pseudopotentials (SIC-PP) for the Zn *3d* electrons configuration.

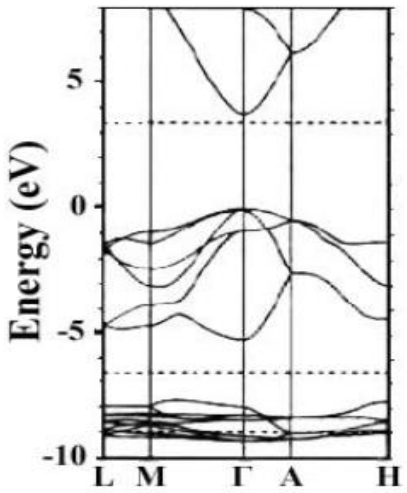

Figure I-3. Band structure of ZnO.

The band structure is shown along high symmetry lines in the hexagonal Brillouin zone. The valence band maxima and the lowest conduction band minima occur at the *Γ* point k = 0 showing that ZnO is a direct band gap semiconductor. In this energy band diagram, the first 10 bands which have energies around -9 eV derived from the Zn *3d* levels. The next 6 bands from -5 to 0 eV correspond to oxygen *2p* levels. The top lines in the diagram are strongly Zn located and correspond to empty Zn *3s* bonding states. Finally, the band gap as determined from this calculation is equal to 3.7 eV. This is close to the experimental value of 3.4 eV.

The band gap value of ZnO could be also measured using optical absorption where the excitation of an electron from the valence to the conduction band can be provided by the absorption of photon

from light which has enough energy to excite an electron. Finally, the observed absorption is directly related to the materials band gap value.

The structural and electronic properties of ZnO determine the optical features of this material. It is well known that ZnO at room temperature has two types of emissions in its photoluminescence (PL) spectrum located in the ultraviolet (UV) and visible range. Figure I-4 shows room temperature PL spectra of ZnO nanostructures obtained with different types of morphologies. These spectra demonstrate various shapes depending on ZnO morphology.

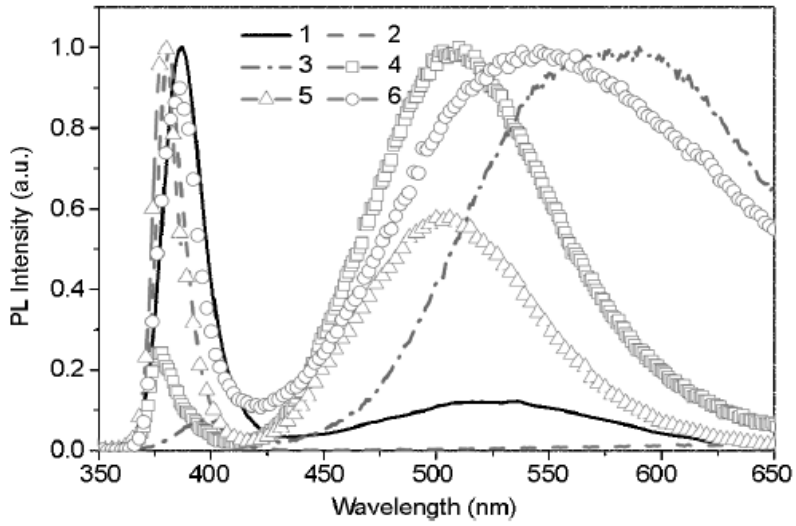

Figure I-4. Room temperature PL spectra of different ZnO nanostructures: 1-tetrapods, 2-needles, 3-nanorods, 4-shells, 5-highly faceted rods and 6-ribbons/combs [15].

For example, ZnO needles and tetrapods exhibit mostly UV emission, while ZnO ribbons/combs nanostructures demonstrate a strong PL emission in the visible range. Moreover, many reports [15] show that the size variation of ZnO nanostructures and the presence of defects have a strong influence on optical properties. Thereby, the luminescence of ZnO nanostructures depends on their size and morphology. In other terms, an applied preparation technique for the synthesis of ZnO nanostructures can strongly influence the optical properties of this material. A discussion

concerning different synthetic routes to obtain of ZnO nanostructures is provided below regarding the corresponding optical behavior.

II. Optical properties of ZnO

Introduction

Optical properties of bulk ZnO materials and nanostructured particles have been studied by photoluminescence (PL) spectroscopy. The dominant part of luminescence spectra of this material has been measured at room temperature. As it was mentioned before, the emission spectrum of ZnO, at room temperature, exhibits the emission band located in the UV domain ($\lambda \approx$ 360 to 380 nm i.e. 3.18 to 3.43 eV) which is attributed to the excitonic recombination and/or a large emission band centered at $\lambda \approx$500-600 nm i.e. 2.07 to 2.48 eV which is attributed to the crystal and surface defects [16-17]. Low temperature (including helium temperature) PL investigations have been performed for a better understanding of the emission origin. In this paragraph, an introduction concerning the nature of UV and visible emission in ZnO is provided.

II-1. UV emission of ZnO

Photoluminescence emission of ZnO in the UV region could be explained by the "excitonic model" which is developed for the explanation of optical properties of direct gap-semiconductors [18]. At 0 K the valence band (VB) of ZnO is fully occupied by electrons, and at the same time, the conduction band (CB) is completely empty. The electrons can be excited from VB to CB due to absorption of photons which have energies higher than the ZnO band gap energy. As a result of this process, the negative charged electrons are moving to the CB leaving positive charged holes in the VB (Figure I-5-A). The electrons and holes can interact through their Coulomb potential and form hydrogen or positronium-like states below the band gap.

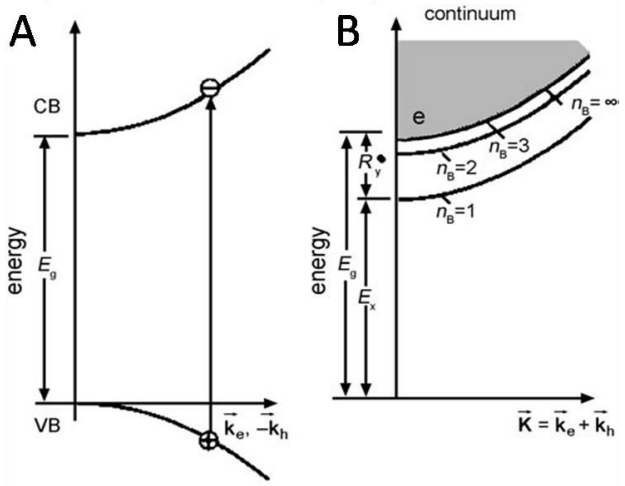

Figure I-5. Band-to-band electron transition (A), excitonic states energy diagram (B) [18].

These states are called excitons, which can be presented as a quasiparticle of excitation or as the quanta of the excitation. There are two types of excitons which are characterized by the average distance between electrons and holes i. e. the excitonic Bohr radius a_B: (i) Wannier excitons where a_B is larger than the lattice constant and (ii) Frenckel excitons which exist in insulators or organic crystals where electrons and holes reside in the same unit cell. The excitonic Bohr radius for ZnO is equal to 1.8 nm.

The other characteristic constant of excitons is the excitonic binding energy or Rydberg energy (R_y^*) (eq. 1). In ZnO, R_y^* is about 60 meV [19]. The total energy of free exciton (E_{ex}) depends on the main quantum number n_B and translational vector $\boldsymbol{K}$. The total energy of exciton is decreasing with increasing quantum number. Ionization of exciton takes place when its quantum number is going to continuum (Figure I-5-B) [18].

$$E_{ex}(n_B, \mathbf{K}) = E_g - \frac{R_y^*}{n_B^2} + \frac{\hbar^2 \mathbf{K}^2}{2\pi M} \qquad \text{(eq. 1)}$$

With E_g the band gap energy, n_B-*1, 2, 3 …*the main quantum number, $\hbar$ the Plank's constant, M the translational mass of the sum of effective electron-electron and electron-hole masses. Eq. 2

shows that free excitons can have different energies, thereby different types of excitonic emissions can be observed. Free excitons into the crystal lattice can also interact with phonons and polaritons. Exciton-phonon interaction takes place due to the moving of the excitons through the potential field which is created by vibrations of crystal lattice i.e. phonons. Interaction of excitons with phonons has also an emission called, for example, longitudinal-optical (LO) phonon replica.

At low temperature, PL spectra of ZnO usually consist from several emission lines in the UV region (Figure I-6). At 110 K, there are two emission lines which are attributed to recombination of free excitons, so-called - FX_A and FX_B around 3.37 eV and their local phonon replicas at 3.3 eV and 3.225 eV (Figure I-6-A). Each free excitonic emission could have its own phonon replica due to the exciton-phonon interaction. With increasing temperature the homogeneous broadening increases (Figure I-6-B). Finally, at room temperature, only one unstructured emission can be observed (Figure I-6-C) as a result of the evolution of the excitonic emissions and corresponding phonon replicas [20].

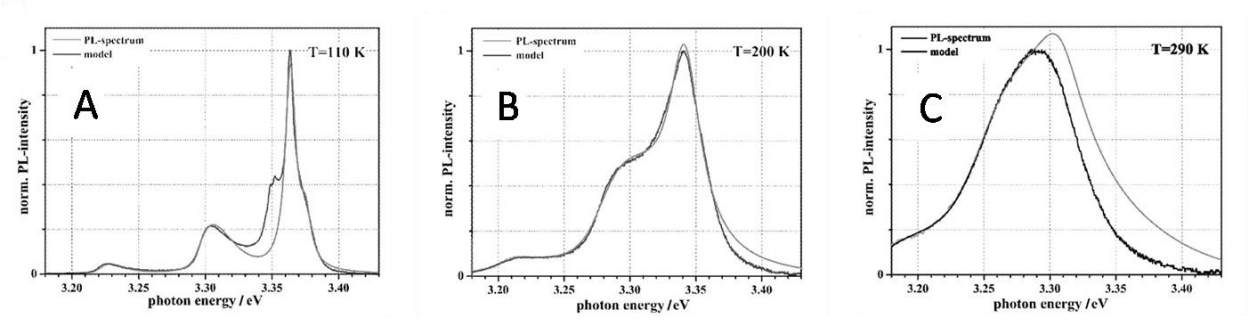

Figure I-6. Low temperature PL spectra of ZnO at 110 K (A), at 200 K (B) and at room temperature (C) [20].

The other type of exciton associated emission which is observed for ZnO at low temperature is related to the bounding of excitons with some centers, impurities or defects which can be present in the crystal such as ionized or neutral donors (D^+, D^0) or neutral acceptors (A^0). These boundings are forming the so-called D^+X, D^0X and A^0X bound-exciton complexes (BEC) [21-22]. BEC

emission in ZnO typically have a very narrow shape of the luminescence lines located between 3.35 and 3.37 eV (Figure I-7).

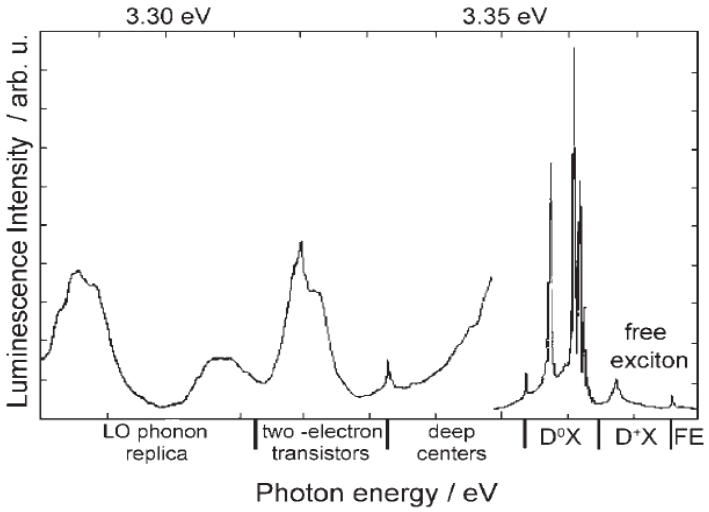

Figure I-7. Emission spectra of ZnO, bound exciton complexes [19].

Low temperature PL properties of ZnO nanostructures have been studied, for example, by Ahn et al. [23]. They have demonstrated low temperature PL measurements for ZnO nanorods and nanopencils (length and diameter of 10.23 μm, 230-340 nm and 1.9 μm, 35-55 nm for nanorods and nanopencils, respectively). In the case of nanorods, at low temperature, PL spectra have free excitonic emission (FX_A (3.38 eV), FX_B) donor bound excitonic emission (D^0X (3.36 eV)) and phonon replicas (FX-LO (3.31 eV)). With increasing temperature, PL spectra show dissociation of D^0X to FX which leads to slower attenuation of FX and FX-LO. Free excitonic emissions (FX) and their phonon replicas (FX-LO) start to dominate at temperatures above 100 K (Figures I-8-A and B). In the case of nanopencils, with increasing temperature, the band-gap change of FX emission is faster than in ZnO nanorods and red-shift in FX-LO peak positions is slower than in the case of ZnO nanorods (Figures I-8-C and D). Such difference can be explained by the influence of surface defects on the exciton-phonon interaction. The final UV-emissions of these nanostructures were localized at different positions (Figure I-9). It was observed a red shift from

nanorods and nanopencils due to the presence of in-plan tensile stress or different contributions of excitonic emissions and their phonon replicas.

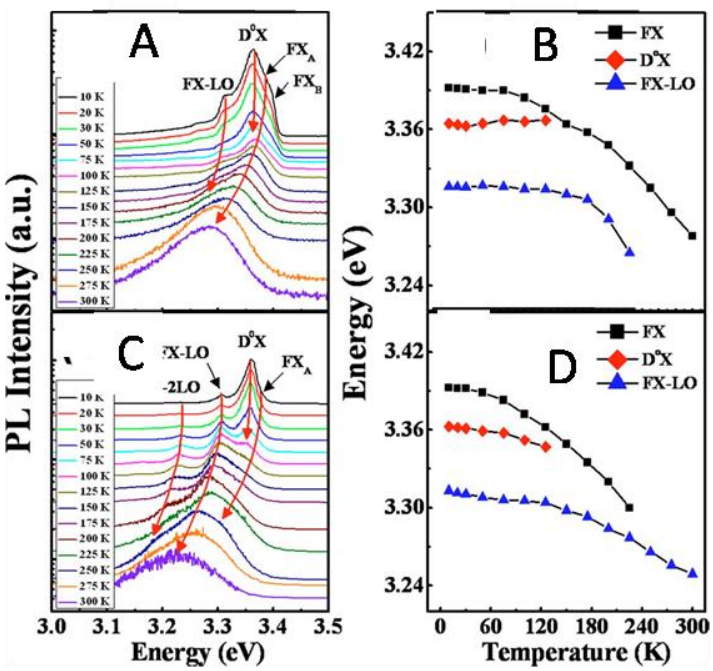

Figure I-8. Low temperature PL measurements of nanorods (A and B) and nanopencils (C and D) [23].

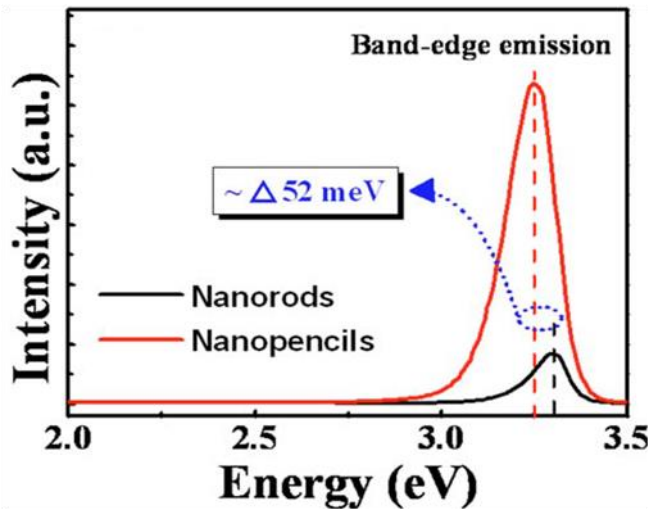

Figure I-9. Room temperature PL spectra of ZnO nanorods and nanopencils [23].

The increase of the density of excitons which can be obtained through the excitation of the materials by, for example, short and intense laser pulses can induce new phenomena. This is known as "High Excitation Effect" [19]. The processes which take place under the increase of exciton

density are shown in Figure I-10 [18]. At low density regime there are free excitons and bound exciton complexes (consider above). At intermediate density regime there are new processes such as elastic/inelastic excitonic scattering. Excitons can scatter elastically under energy and momentum conservation (eq. 2) [18].

$$\hbar\omega_{pn} = E_x(n_B = 1, \mathbf{k} = 0) - E_x^b(1 - \frac{1}{n_{Bf}^2}) - \frac{\hbar^2}{M}\mathbf{k}_{i1}\mathbf{k}_{i2} \qquad \text{(eq. 2)}$$

With E_x the energy of the exciton ground state, M the translational excitonic mass, $\boldsymbol{k}$ the wavevector. In the case of inelastic scattering one exciton is scattered to the higher energy state with the main quantum number n_B=2, 3, 4 … or to the continuum i.e. could be ionizated until electron and hole. The other exciton, in this case, could be scattered down and leaves the sample as a luminescence photon (Figures I-11-A and B) [18].

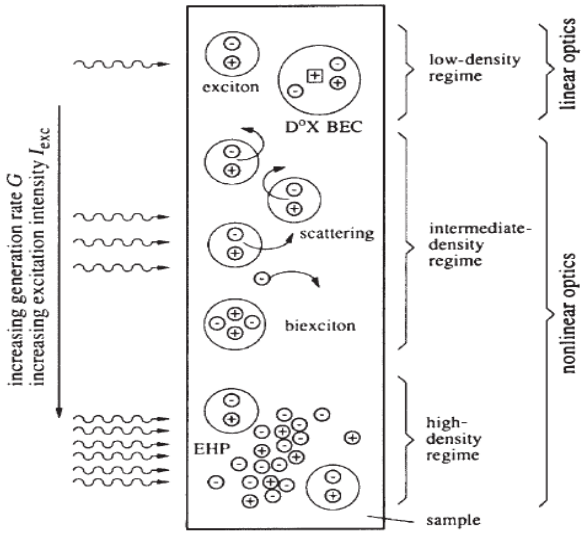

Figure I-10. Scheme of semiconductors behavior under different excitation densities [18].

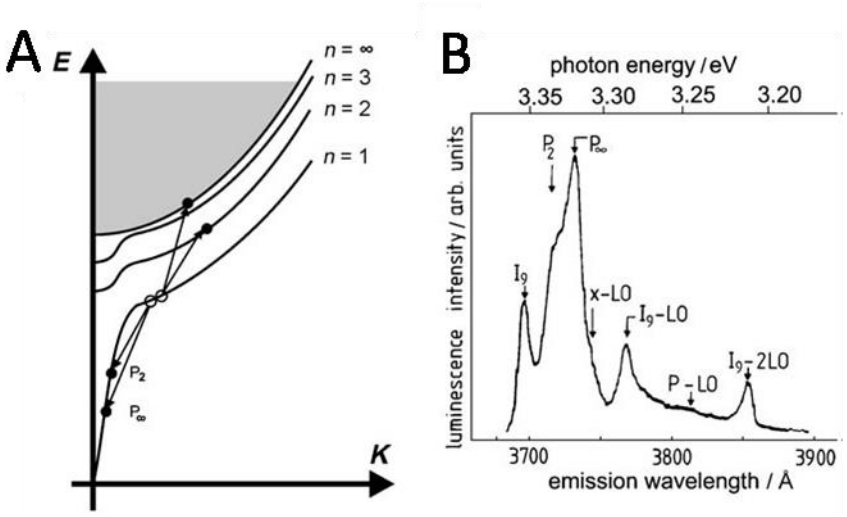

Figure I-11. Scheme of the inelastic scattering of the excitons (A), the observation of the inelastic scattering on the luminescence spectrum (B) [18].

The other process which takes place at low temperature and intermediate excitation density regime is the formation of biexciton as an analog of hydrogen or positronium molecule. This process can occur by the collision of two free excitons or by the absorption of two photons starting from crystal ground state or from absorption of one photon by free exciton. In the case of the formation of biexciton from two free excitons the binding energy of two free excitons should be dissipated to the formation of biexciton in the form of a phonon or photon emission. The formation of biexciton by the absorption of photon by one free exciton is called induced absorption [18]. It occurs at a photon energy which is shown in eq. 3:

$$\hbar\omega_{ia} = E_x - E_{xx}^b - \frac{\hbar^2 k_i^2}{4M} \qquad \text{(eq. 3)}$$

With E_x the total energy of exciton and E_{xx} the total energy of biexciton. Figure I-12 shows all processes which occur under increasing excitation densities of the beam at low temperatures [24]. At low excitation density regime, the formations of the BEC are presented. At the intermediate excitation density regime P-band (inelastic scattering of the excitons) is indicated around 3.32 eV. At high excitation density regime, one unstructured emission band has been observed. This band

is called the M-band. M-band is explained as a radiative recombination of a BEC under emission of the acoustic phonons.

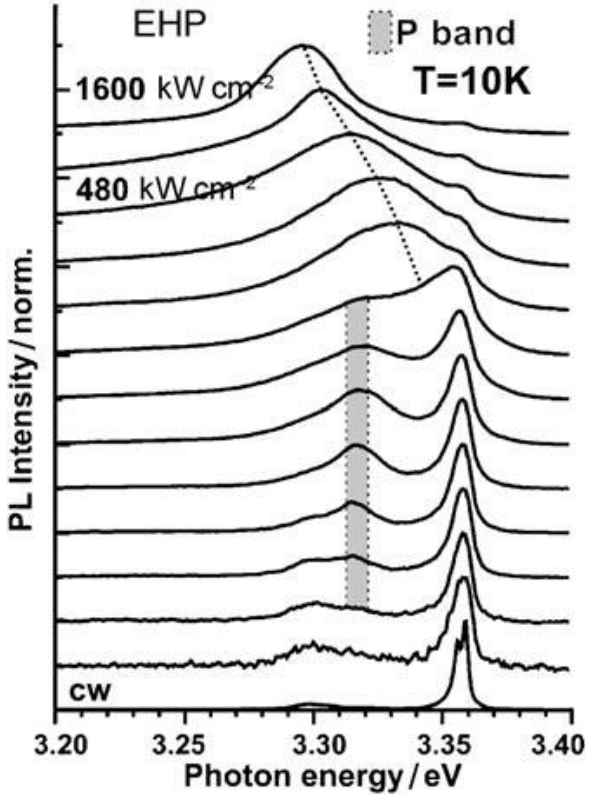

Figure I-12. Normalized luminescence spectra of ZnO under increasing excitation at low temperatures.

II-2. Visible Emission of ZnO

PL spectra of ZnO nanostructures have a number of different bands in the visible spectral domain at room temperature. These bands could be attributed to the PL emissions of different types of crystal and surface defects. A number of emission lines have been reported at 405, 420, 446, 466, 485, 510, 544, 583 and 640 nm [16]. The natures of the electronic levels of the defects have been calculated by a number of groups. One example is illustrated on Figure I-13 [25-27].

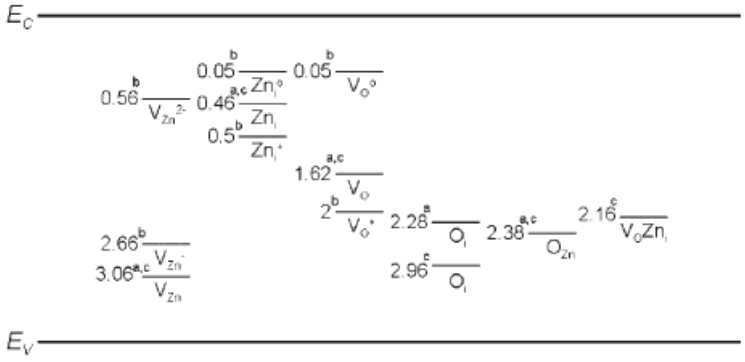

Figure I-13. Calculated defect emissions in ZnO [16].

Green emission is one of the most observed defect emissions in ZnO nanostructures [16]. Green emission usually appears at 2.5 eV in undoped ZnO. In some studies, this type of PL emission in undoped ZnO has been attributed to copper impurities [28]. Moreover, green emission is also reported in Cu doped ZnO nanowires [29]. However, the attribution of the nature of green emission to copper impurities cannot explain the defect emission in all ZnO nanostructures especially where defect emission exhibit very strong dependence on annealing temperature and atmosphere which would be more consistent with the other types of intrinsic defects than Cu impurities. The other explanation of the nature of green emission band in ZnO has been proposed by Lin et al. [29] as antisite oxygen, this conception was based on band structure calculations. There are also a number of studies which propose some other propositions concerning the nature of green emission in ZnO nanostructures such as intrinsic defects – donor-acceptor transitions [30], zinc vacancy [16], surface defects [31] and recombination at $V_o^{\bullet\bullet}$. In the last case, these $V_o^{\bullet\bullet}$ centers appear due to surface trapped photogenerated holes, followed by recombination with electron in an oxygen vacancy $V_o^{\bullet}$. The singly ionized oxygen vacancy $V_o^{\bullet}$ is the most cited proposition. For example, green emission of ZnO is increasing during annealing at temperature above 600 ˚C [32]. Such behavior was attributed to out-diffusion of oxygen atoms and as a result concentration of oxygen vacancies is started to be higher [28, 31]. The donor-acceptor transition hypothesis used to explain the green emission has also been challenged [33]. On the other hand, while the Zn vacancy

hypothesis is supported by the study of the effect of O and Zn ions implantation [16], a blue rather than green emission would be expected based on the theoretically predicted energy levels for Zn vacancy [26]. The influence of surface defects on the green PL emission in ZnO has been investigated by a number of studies [31, 34-37]. For example, Gong et al. [36] have studied the optical properties of colloidal-synthesized spherical ZnO nanoparticles prepared with from 1-octodeceine (OD) and different ration mixtures of OD - trioctylamine (TOA) and trioctylphosphine oxide (TOPO). It has been shown that green PL luminescence of ZnO samples from the mixture of TOA/OD and TOPO/OD is largely suppressed compared with that from pure OD. The green emission band is situated due to oxygen vacancies which are located on the surface of ZnO nanoparticles. By modifying surface states (achieved by introducing TOA and TOPO to the regular solvent OD), the green emission band can effectively be quenched. In this study, room temperature PL spectra of ZnO spherical nanoparticles exhibit the near-band-edge UV emission, and the defect related green luminescence is only observed for the small spherical nanoparticles (Figure I-14). Such behavior shows that the green emission is associated with defects near the surface, and thus it is quenched with the increasing of the diameter. Polarized luminescence measurements from aligned ZnO nanorods also show that green PL emission could be originated from the surface of ZnO nanorods [38].

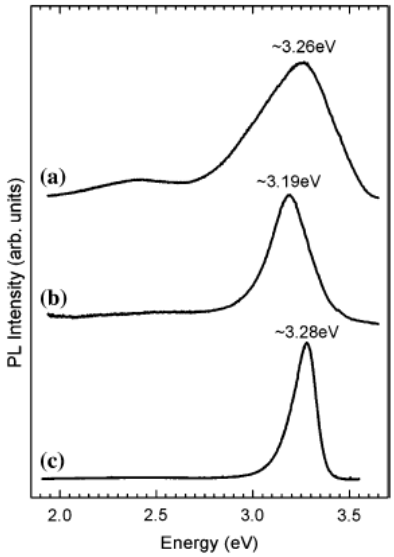

Figure I-14. Room temperature PL spectra of ZnO, small spherical nanoparticles with 5 nm in diameter - a, large spherical nanoparticles with 12-14 nm in diameter - b and bulk ZnO – c [36].

Yellow defect emission at ~2.1 eV is also one of the commonly reported visible emissions in ZnO nanostructures [16, 39-41]. This type of PL emission usually situated in the ZnO samples prepared by the aqueous solutions of zinc nitrate and hexamethylenetetramine [40-42]. Yellow PL emission in ZnO nanostructures is usually attributed to the oxygen interstitial. The Li-impurities is also could be an explanation of this emission [41]. The deep levels responsible for green and yellow emissions are different [41-42]. Yellow emission in ZnO is not located at the surface instead of green emission [44]. The orange-red emission which is situated at ~1.75 eV is also observed in ZnO nanostructures [27, 44-45]. Moreover, yellow and orange-red emissions can have similar deep levels but different initial states (conduction band and shallow donors) [46]. These two visible emissions can present different dependences on the excitation wavelength [47]. Fan et al. [44-45] reported that the visible emission in ZnO nanowires and nanosheets consisted of two components and has a maximum at ~540 and ~610 nm. The emission in ZnO nanosheets has been attributed to surface dislocations [45]. Some the other attributions of orange-red PL emissions have been done for different ZnO nanostructures. For example, the emission at ~626 nm on ZnO nanorods was attributed to oxygen interstitials [43] and the orange emission at the region 640-650 nm in ZnO

needles and nanowires to zinc vacancies [48-49]. The different hypothesizes for the visible emission in ZnO nanostructures have been applied by Djurišić et al. [49]. They reported the investigations of defect emission before and after annealing at different temperatures of three types of ZnO nanostructures such as shells, needles and rods. These ZnO nanostructures emit three different green, yellow and orange-red defect emissions respectively. The temperature dependence of these defect emissions for two different excitations wavelengths (325 and 390 nm) are shown in Figure I-15.

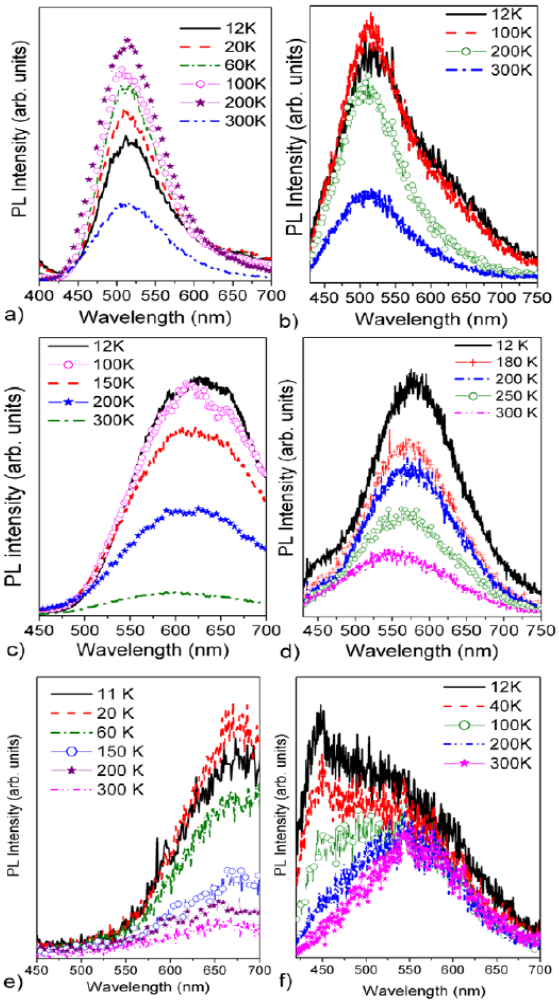

Figure I-15. Temperature dependent PL spectra at the visible region of different ZnO nanostructures excited at 325 and 390 nm for shells – a and b, rods – c and d, needles – e and f [49].

In the case of shells (green emission), no significant shift of the emission peak can was observed with temperature (Figure I-15 A and B). Such behavior probably indicates that this emission originates from the donor-acceptor transitions. ZnO rods (yellow emission) (Figure I-15 C and D), for both excitation wavelengths, have a blue shift with increasing temperature. ZnO nanorods in this study were prepared by hydrothermal method and yellow emission in this case could be attributed to $Zn(OH)_2$ or OH groups, instead of the commonly assumed interstitial oxygen defects. On the other hand, ZnO needles exhibit different behavior. As it is shown in Figure I-15 E and F, orange-red emission is decreasing with temperature increasing under 325 nm excitation. In the case of 390 nm excitation two emission peaks – blue and green appear at low temperature. The emission of the blue peak decreases with temperature increasing and finally this peak disappears at 200 K, while that of the green peak remains the same. The different PL bands were attributed to multiple negative charged defects.

ZnO nanostructures can exhibit different types of PL emission in the visible domain of spectra. The most common and often visible emission in this material is green emission. This type of visible emission is most controversial and there are a number of hypothesizes which could be applied for the explanation of this phenomena. Therefore, the origin of the green emission is still an open question and the real nature of this emission requires further study.

III. Synthesis of ZnO nanostructures

Introduction

In the last decades, a number of synthetic methods have been reported for the preparation of ZnO nanostructures with different physico-chemical characteristics in term of size, size distribution, morphology and optical properties. In respect to the optical properties of ZnO nanostructures, the synthetic techniques could be divided in three different approaches such as high temperature gas phase methods, low temperature liquid phase methods and still supercritical fluids. The high temperature gas phase methods allow obtaining high quality ZnO nanostructures due to its high operating temperature. ZnO nanostructures mainly demonstrate a high and efficient UV photoluminescence; however the size and morphology control of ZnO nanostructures is a difficult in this approach. Low temperature liquid phase approach allows producing ZnO nanostructures with well controlled size and morphology due to the invitation of different surfactant systems. On the other hand, the low operation temperature of this approach leads to different surface and bulk defects and as a consequence, a strong visible emission appears in PL spectra. The third recent approach namely “supercritical fluids” route has been developed at ICMCB. This approach allows obtaining ZnO nanocrystals with an efficient UV emission; this method couples the advantages of liquid phase approach for the design and high temperature approach for the crystallinity. This section provides some of the most representative examples of the synthetic techniques reported in literature for designing of ZnO nanostructures with regard to their optical characteristics.

III-1. High temperature gas phase approach

High temperature gas phase approach for the synthesis of ZnO nanomaterials includes several methods such as mainly chemical vapor deposition (CVD) and physical vapor deposition (PVD).

CVD is one of the common growth methods for bulk ZnO [50], thin films [51], nanowires and nanorods [52]. This method is based on spraying of molecular compound of Zn^{2+} such as zinc acetylacetonate [53] and also spraying of Zn using a reduction of ZnO by different reduction agents [54-56]. In a CVD method, the precursor is transported via the vapor phase to the reaction chamber and adsorbed on a heated substrate followed by decomposition of the precursor forming nanostructures or films. This system is heated to the high temperature to cause pyrolysis of the precursor and oxide formation. In this process, a vapor liquid solid (VLS) mechanism is the most usable technique to construct nanowires and nanorods. In a typical VLS process, a metal catalyst is forming eutectic liquid droplets determining the diameter and the growth direction of the target nanorods because the size of these droplets is unchanged during the process. For example; Huang et al. [57] have reported ZnO nanowires (Figure I-16) formation with a diameter in the range between 80 and 120 nm and the lengths between 10 and 20 µm through the VLS mechanism.

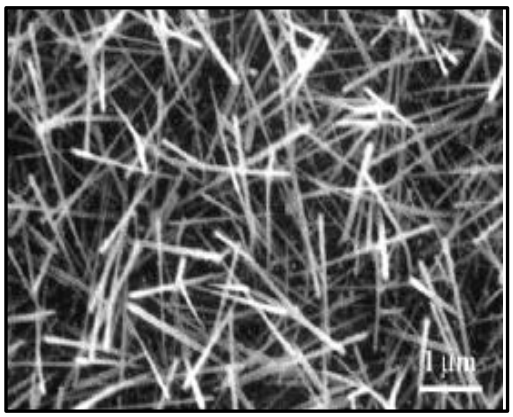

Figure I-16. a) SEM image of ZnO nanowires using CVD method by Huang et al. [57].

Huang reported that Zn vapor was generated using carbothermal or hydrogen reduction of ZnO. ZnO nanowires were grown on Au-coated silicon substrates by heating a 1:1 mixture of ZnO and graphite powder to 900-925 °C under a constant flow of argon for 5-30 min.

PVD is another widely used high temperature gas phase technique, which is very similar to the CVD method except that vapor phases undergo chemical reactions. A typical PVD process concludes a physical evaporation of the vapor species afterwards; the vapor species are transported and condensed on a substrate which is placed in the hot zone of the furnace. The material is moving through the energetic and entropic environment and deposed from its surface. The vacuum in deposition chamber allows particles to move freely. An electric resistance heater is used as a thermal evaporator to melt the material in order to produce vapor. The vapor is thermodynamically diffusing to the substrate in a high vacuum in order to avoid any reactions with or scattering of other gas atoms in the chamber. For example, Tigli and Juhala [58] have applied PVD for the synthesis of ZnO nanowires on a silicon substrate with a diameter in the range between 50 and 120 nm and with a length of 2-7.1 μm. Jimenez-Cadena et al. [59] obtained ZnO nanowires, nanosheets and branched nanostructures with this method (Figure I-17).

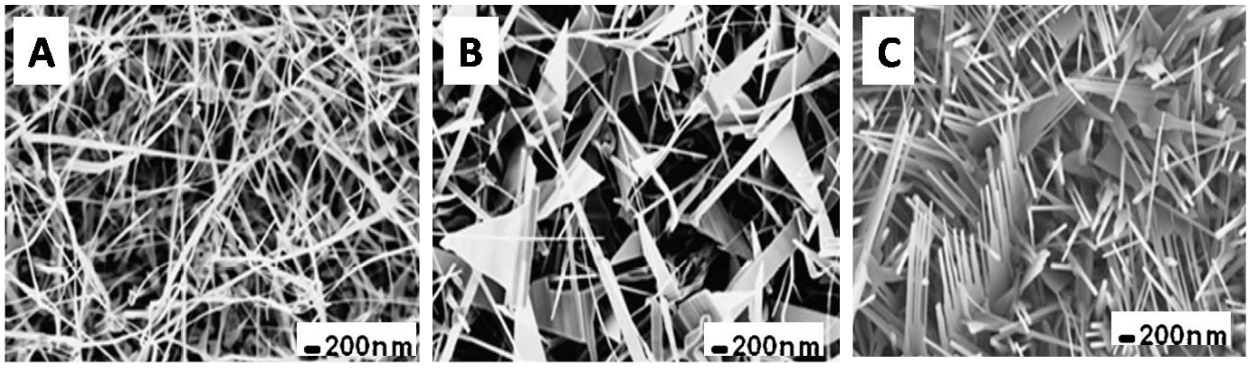

Figure I-17. ZnO nanostructures synthesized by PVD: nanowires (A), nanosheets (B) and branched nanostructures (C) [59].

III-2. Low temperature liquid phase approach

Aqueous solution growth is a well-known methodology for the synthesis of metal oxide nanoparticles; this technique is also called precipitation method. The wide range of metal oxide nanoparticles such as Fe_3O_4 [60-67], Fe_2O_3 [68-70], TiO_2 [71] and ZnO [72] have been synthesized by this method.

This methodology is based on precipitation in aqueous solution of different precursors such as chlorides, nitrates, sulfates by adding bases. This method includes the simultaneous occurrence of the nucleation, growth, coarsening and/or agglomeration processes. These processes which are participating to the whole reaction could be modulated by a stabilizing agent.

Jolivet et al. [73] have reported the formation mechanism of metal oxide nanoparticles in precipitation process. According to these authors, the metal cations issued for the dissolution of metal salts in aqueous solution can form two different complexes, such as *aqua* ($[M(OH)_h(OH_2)_{N-h}]^{(z-h)+}$) and *oxo* complex ($[MO_{N-h}(OH)_h)^{(2N-z-h)-}$. Condensation of *aqua* complexes proceeds by olation with elimination of water and formation of hydroxo bridges:

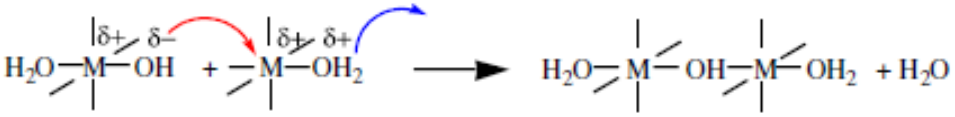

(eq. 4)

For *oxo* complexes where is no water molecule in the coordination sphere of the complex therefore these complexes do not have leaving groups. In this case, condensation has to proceed via a two-step associative mechanism leading to the formation of oxo bridges:

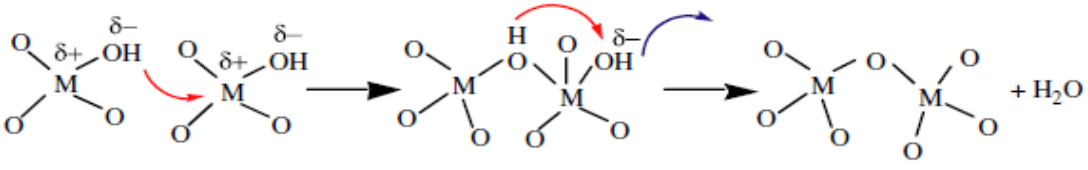

(eq. 5)

Aqueous solution growth of highly oriented ZnO nanowires and other nanostructures has been reported by many authors (Table I-1). Usually, a solution of $Zn(NO_3)_2$ and hexamethyltetramine (HMT) is used for the synthesis of ZnO nanoparticles with this method:

$$(CH_2)_6N_4 + 6H_2O = 6HCHO + 4NH_3 \quad (1)$$

$$NH_3 + H_2O = NH_4^+ + OH^- \quad (2)$$

$$2OH^- + Zn^{2+} = ZnO_{solid} + H_2O \quad (3)$$

Table I-1 Different precursors and bases for the aqueous solution growth of ZnO nanostructures with various morphologies.

Growth Solution	Morphology of ZnO nanostructures	Ref.
Zinc nitrate and HMT	Aligned nanowire arrays	[74]
Zinc nitrate and HMT	Nanorods, nonotubes	[75-77]
Zinc nitrate, HMT, citrate	Oriented nanocolumns, nanoplates	[78]
Zinc nitrate, HMT, Zinc acetate	Highly aligned nanorods	[79]
Zinc nitrate, triethanolamine, HCl (pH 5)	Oriented nanorods	[80]
Zinc nitrate, thiourea, ammonia, NH_4Cl	Nanowires	[81]
Zinc acetate, NaOH, citric acid	Disk-like, flower-like, nanorods	[82-83]
Comparison of different growth solutions	Star-like nanorods	[84]
Zinc sulfate, ammonium ions, NaOH	Nanobelt arrays, ordered nanowires	[85-86]

Aqueous solution growth is the low temperature method for the synthesis of various metal oxide nanostructures including ZnO. This methodology allows controlling morphology of ZnO nanostructures by the changing operating parameters such as the nature of precursors, pH, temperature, solvent etc. This method also allows inviting different surfactant systems for the stabilization of the final nanomaterials. A wide range of morphologies of ZnO nanoparticles could

be obtained playing with the operating temperature of the process and with the concentration and/or the nature of surfactants.

Another low temperature liquid phase technique is water-in-oil (W/O) microemulsions (also called "reverse micelle solution") which are transparent, isotropic, thermodynamically stable liquid media. In this method, fine microdroplets of the aqueous phase are trapped within assemblies of surfactant molecules dispersed in a continuous oil phase. The surfactant-stabilized microcavities (typically in the range of 10 nm) provide a confinement effect that limits particle nucleation, growth and agglomeration [87].

For example, Singhal et al. [88] have applied this strategy for the synthesis of ZnO nanoparticles. The principle of this method lies in the preparation of two different microemulsions. First emulsion is constituted of microdroplets of zinc precursors (zinc acetate, zinc nitrate, zinc sulfate) in water which are stabilized by surfactant molecules in a continuous oil phase. Second emulsion usually contains water microdroplets of bases such as ammonium hydroxide in the same continuous oil phase. These two microemulsions are mixed together in order to precipitate $Zn(OH)_2$. Zinc hydroxide can be easily decomposed to ZnO nanoparticles by heating at the temperature of 398 K [89]. Also, the other bases can be used in this method. For example, a large number of ZnO nanoparticles with different morphologies such as sticks, triangles and circles have been obtained by using trioctylamine as base [90-92]. Figure I-18 shows these ZnO nanoparticles.

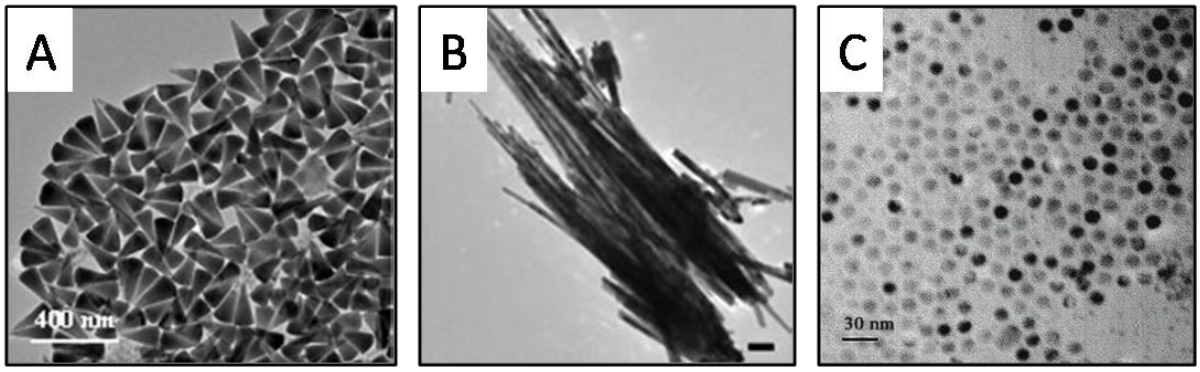

Figure I-18. ZnO nanoparticles with different morphologies prepared by inverse microemulsion method: triangles [91] (A), sticks [90] (B) and microspheres [92] (C).

In addition, the inverse microemulsions method is a particular case of the aqueous solution growth for the synthesis of the nanomaterials. The mechanism of the formation of nanostructures is similar in both cases. The formation of the metal oxide nanoparticles is going by the precipitation into micelles playing the role of "nanoreactors". The most important point of the inverse microemulsions is that the size of the droplet can determine the size of the final nanoparticle. Thereby, the principle control of the size and size distribution of the nanomaterials can be provided by the size control of the emulsion droplets. As in the case of aqueous solution growth, microemulsions method has many possibilities to provide the morphology control of nanomaterials playing with the operating parameters of the process.

Another low temperature technique for the synthesis of ZnO nanostructures is the organometallic method. This method is based on the decomposition of the metal-carbon bonds of organometallic precursors. The decomposition of metal-carbon bond usually takes place by oxidative agents such as O_2 and H_2O which are present in the reaction media. High energy of metal-carbon bonds makes these reactions exothermic. Thereby, metal oxide nanoparticles can be prepared at low temperature. In the first step, the decomposition of the organometallic precursor gives molecular complex which can grow. Finally, these nuclei evolve by two different ways such as absorptions of atoms on the core or clusters coalescence.

The organometallic method was adopted for the synthesis of ZnO nanoparticles. ZnO nanocrystals have been obtained by the decomposition at 250°C of zinc (II) 2-ethylhexanoat in diphenyl ether and in the presence of amines as surface capping agents [93]. Choi et al. [94] have reported the synthesis of hexagonal pyramid-shaped ZnO nanocrystals by using hydrolysis of Zn-oleate complex. This complex can be easily prepared from $ZnCl_2$ and sodium oleate. Chen et al. [95] have demonstrated the growth of ZnO triangles through the reaction of Zn stearate with excess amount of alcohol in hydrocarbon solvents (noncoordinating solvents) under elevated temperatures. Organometallic precursors, which are based on cubane structures [96], have also been used for the synthesis of ZnO nanoparticles [97]. Thermolysis of alkyl-alkoxyzinc heterocubanes [$MeZn(O^tBu)_4$] as precursor at 350°C leads to the formation of ZnO nanoparticles [97-99]. During this reaction ZnO nanostructure is preorganized at a molecular scale due to the occurrence of a central Zn_4O_4 motif (Figure I-19).

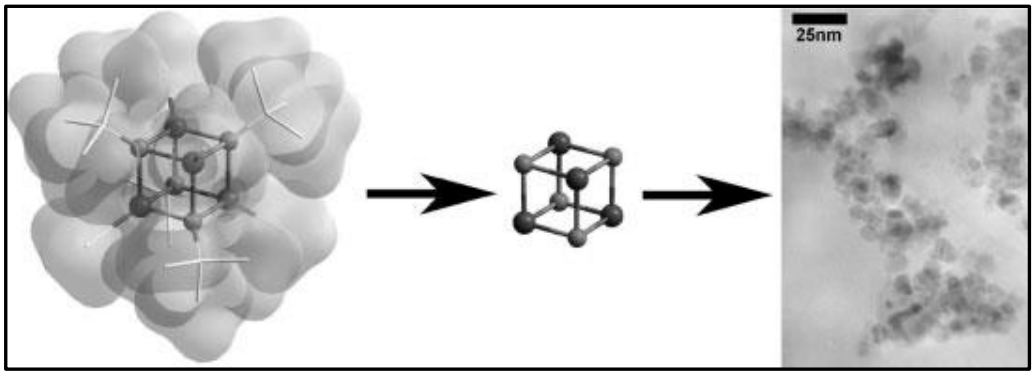

Figure I-19. Scheme of the transformation of an organometallic precursor to ZnO.

Boyle et al. [100] have demonstrated precursor structural influence on ZnO nanoparticle morphology. In this work, the effect of nuclearity was determined for the final nanoparticle morphology and size: four representative nuclearities mono-, di-, tetra- and hepta- nuclear were chosen and used to form ZnO nanoparticles. The mononuclear precursor formed polydispersed spherical nanoparticles of würtzite, whereas the nanoparticles generated from the other samples

were nanorods (Figure I-20, A-D). This method allows the production of single particles with size larger than 10 nm and rods with average size from 50 to 100 nm.

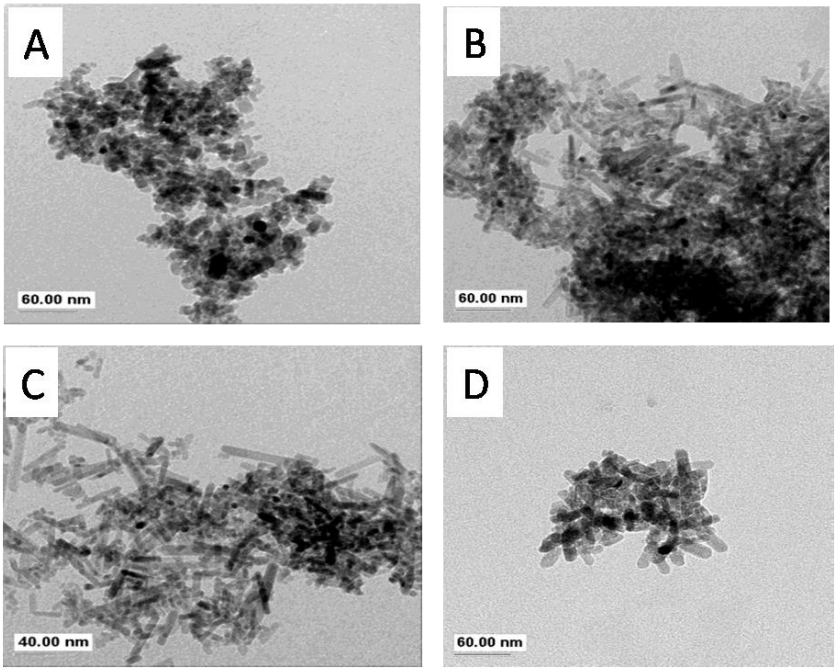

Figure I-20. ZnO morphology [100]: spherical nanoparticles (A) and rods (B-D).

ZnO nanoparticles have also been obtained by the decomposition of precursor which contains the alkyl or alkoxides groups in the presence of trioctylphosphine oxide (TOPO). For example, ZnO nanoparticles with size of 3 nm were prepared by thermolysis of [$EtZnO^{i}Pr$] as a single molecular precursor and TOPO at 160°C [101]. In this reaction, TOPO as stabilizing agent leads to a control of size evolution over a time. Two-steps approach has also been developed for the organometallic synthesis of ZnO nanoparticles [102-104]. For example, Rataboul [104] has reported a strategy based on the decomposition of organometallic precursor such as [$Zn(C_6H_{11})_2$] in wet anisole at 130°C in order to obtain Zn nanoparticles followed by thermal oxidation of Zn nanoparticles to form ZnO nanoparticles without coalescence and size change. Recently, this group has reported the one-step method for the synthesis of ZnO nanoparticles using the decomposition of [$Zn(C_6H_{11})_2$] in moist air [105]. Also, ZnO nanoparticles have been synthesized by the decomposition of organometallic precursor $Zn(c\text{-}C_6H_{11})_2$ under moistly air and in the presents of

long-alkyl-chain amines as surfactant agent [106]. This method yields to obtain spherical ZnO nanoparticles with a size of 3 and 6 nm and also nanorods with a mean diameter of 3-4 nm and length about 120 nm. Glaria et al. [107] have obtained ZnO nanostructures using $Zn(c\text{-}C_6H_{11})_2$ as a precursor in the presence of Li and Na co-precursors as a growth controlling agents. They demonstrated that Li containing co-precursor induce a modification of the growth of ZnO nanoparticles while, no effect is observed when Na co-precursor is used. Indeed, spherical nanoparticles were observed when Li co-precursor was added while; nanorods were formed with Na co-precursor as already observed in the same experiments without using alkali-metal containing precursors. In addition, organometallic method allows production of ZnO nanostructures with a small size and narrow size distribution with different morphologies. The small size of the nanoparticles obtained with this method can be explained by the specific mechanism of nanoparticles formation i. e. nucleation due to the decomposition of high energy carbon-metal bounding.

Another very often used liquid phase technique for the synthesis of ZnO nanostructures is the sol-gel method. Sol-gel is a well known chemistry for the synthesis of metal oxide nanoparticles. Regardless of the type of the metal oxide particles, this procedure involves several steps: (i) formation of a stable solution of the alkoxide or salt based precursor such as Zn chlorate, nitrate and acetate (sol); (ii) an increase of medium viscosity by polycondensation or polyesterification of a formed alcohol-bridge network (gel); (iii) aging of the gel (syneresis, condensation reactions are active until a solid is formed); (vi) drying of the gel, in order to remove all the solvent volatile compounds retained in the network; (v) dehydration, the surface M-OH are removed by thermal treatment avoiding the re-hydration of the gel and (iv) densification and decomposition of the gel. Spanhel et al. [50] have reported the sol-gel technique which is based on the dissolution of a zinc salt by ultrasonication, adding a lithium hydroxide (LiOH) and heating at temperature below then 100°C. The problem of this synthetic method is an evolution of particle size over time. There are

two possible ways which can describe the growth of ZnO nanoparticles. These are Ostwald ripening and aggregation. The particles of the fresh sample have a size close to 3.5 nm and after 5 days their size are increased until 5.5 nm. The method of Spanhel et al. was modified by Haase et al. [108] by controlling the amount of water in the mixture of the reagents; ethanol was used as solvent. This synthesis was performed at 0°C leading to particles of 2 nm in size. ZnO nanoparticles were continued to grow or age after the synthesis even when stored at 0°C. The average diameter of the particles evolves rapidly from 2 until 7 nm over 5 days. The rate of nanoparticles growth is controlled by the concentration of the precursors, dissolved species and their reactivity, which depends on the particle surface and the solution composition. The growth also takes place in a washed sol which has been redispersed from a pure ZnO precipitate. ZnO nanoparticles can be formed by several processes such as hydrolysis (1) and condensation (2) of the dissolved species. Hydrolysis of ZnO nanoparticles (3) which is equivalent to ZnO dissolution also takes place [108].

$$Zn - OAc + H_2O/OH^- = Zn - OH + HOAc/OAc^- \quad (1)$$

$$Zn - OH + Zn - OAc = Zn - O - Zn + HOAc \quad (2)$$

$$Zn - O - Zn + H_2O \rightarrow Zn - OH + Zn - OH \quad (3)$$

The morphology of ZnO nanoparticles can be changed during the synthesis. For example, Pacholski et al. [109] show spherical particles of ZnO which were prepared by the decomposition of zinc acetate in an alcoholic medium in the presence of KOH, but after the refluxing of the mixture for a few hours, spherical nanoparticles are transformed to nanorods. In addition, sol-gel method is a simple, green and cheap technique for the production of a big scale of ZnO nanomaterials. This method allows obtaining ZnO nanostructures with small size, narrow size distribution and also to control the size of nanoparticles by the storage or temperature etc.

Another very often used liquid phase technique for the synthesis of ZnO nanostructures is solvo/hydrothermal method. This technique allows preparation of ZnO nanoparticles with size larger than 100 nm. Usually, these reactions are carried out in the autoclaves and batches in order to achieve higher temperature then boiling point of the solvents. This method was adopted for the synthesis of ZnO nanoparticles with different types of morphologies (Table I-2).

Table I-2. ZnO nanoparticles with different types of morphologies prepared by solvo/hydrothermal method

Growth solution	Morphology of ZnO nanoparticles	Ref.
$Zn(Ac)_2 \cdot H_2O$, citrate potassium, ammonia	Doughnut shaped	[110]
$Zn(NO_3)_2$, hexamethyltetramine	Nanorods	[111]
Diethyl zinc, Polystyrene	Spheres	[112]
Zn powder, 5%O_2 in Ar	Nanowires	[113]
ZnO, Carbone, Ar	Pillars	[114]
ZnO, Carbone, 2% O_2 in Ar	Nanorods	[115]
NaOH, H_2O_2 and zinc foil	Nanorods	[116]

For example, Burawati at al. [117] have demonstrated the synthesis of the spherical ZnO nanoparticles in water medium using zinc nitrate hexahydrate. This synthesis was carried out in an autoclave at 120 ˚C after reaching pH equal to 7.5 by the ammonium hydroxide. Lu et al. [118] obtained crystalline ZnO powder by the decomposition of $Zn(NO_3)_2$ in the presence of ammonia base using different operating temperatures such as 100, 150 and 200 ˚C for 2 hours. In this study, the growth of ZnO nanoparticles was investigated as a function of temperature and pH. Also, ZnO nanoparticles were prepared using zinc chlorate and sodium hydroxide in a hydrothermal growth process using different organic template agents [119]. Some changes in morphology of ZnO

nanoparticles were observed. For example, the rod-like ZnO nanoparticles have been transformed to polyhedral-like structures increasing temperature. Also, it was shown that morphology of ZnO nanoparticles depends on the nature of an organic template when temperature was maintained at 160 ˚C. Musić et al. [120] have reported a simple procedure of ZnO nanoparticle preparation using tetramethylammonium hydroxide as a precipitation agent at pH~14. Solvo- and hydrothermal method of ZnO nanostructures growth allows to prepare a wide range different size and shape nanoparticles due to variations of nature of precursor, bases, pH and also by adding of surfactant agents. Playing with different solvents could also change the morphology of final ZnO nanoparticles.

As it was discussed above, high temperature gas phase and low temperature liquid phase approaches for the fabrication of ZnO nanostructures have their specialties such as high operating temperature used in high temperature gas phase approach which leads preparation highly crystalline ZnO nanostructures and possibility to use different surfactant systems in low temperature liquid phase approach allows having good size and morphology control of ZnO nanostructures. However, a poor size and morphology control in the case of high temperature gas phase approach and low crystallinity of the material obtained using low temperature liquid phase approach make it difficult to obtain ZnO nanostructures with a various size and morphology keeping good crystallinity i.e. high optical quality. Recently, the synthetic approach based on supercritical fluids was developed for the fabrication of ZnO nanostructures. This approach allows production of ZnO nanostructures with high crystallinity thanks to high operating temperature and their good size and morphology control due to a possibility to invite different surfactant systems. All details concerning this approach are discussed in next section of this paragraph.

III-3. Supercritical fluids approach

Supercritical fluids (SCFs) were applied to the synthesis of nanomaterials at the beginning of the 1990s. This technique is based on the specific properties of the fluids in supercritical conditions. A fluid started to be supercritical when it reaches the critical temperature (T_c) and pressure (P_c). Supercritical domain of the fluids combines both characteristic properties of a liquid and gas. Figure I-21 shows a schematic representation of density and organization of molecules of a pure fluid in solid state, liquid, gas state and also supercritical domain. The density of the gas state becomes equal to that in a liquid state and the interface disappears. The macroscopic behavior of the fluids in the supercritical domain is characterized by mechanical and thermal instabilities [121-124].

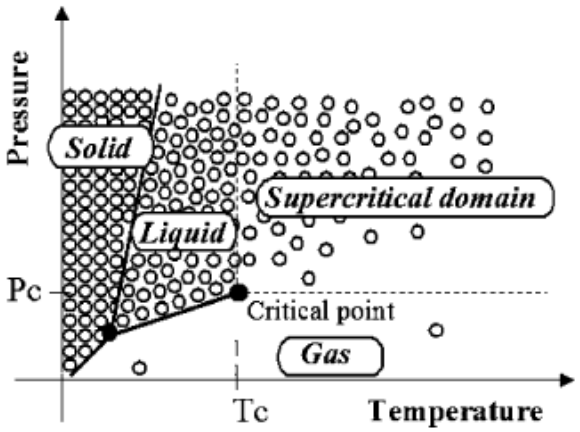

Figure I-21. Schematic representation of microscopic behavior of a pure fluid in T-P plane phase diagram [122].

Since the beginning of the 1990s, Supercritical fluids offer continuous, scalable, fast and facile routes towards well-crystallized tailor-made oxide nanoparticles. This method has already been used to synthesize various inorganic materials (metals, semiconductors, nitrides, oxides, etc.) with controlled size, complex shapes and compositions. In the last 20 years, the use of supercritical water as solvent was extended to other fluids to synthesize nanostructures, especially alcohols [123]. Supercritical fluids allow providing the process which is based on the transformation of a

metal precursor. This process was applicable for the synthesis of different metal oxide such as Cu_2O, Cr_2O_3, Al_2O_3, Ga_2O_3, CeO_2, $Ba_{1-x}Sr_xTiO_3$ ($0 \leq x \leq 1$), $BaTi_{1-x}Zr_xO_3$ ($0 \leq x \leq 1$), ZnO… in a range of temperature between 200 up to 400 ˚C and at about 20-25 MPa [125-133].

The operating parameters in SCFs synthesis play very important role on final properties of the material. According to that, the control of operating parameters in SCFs is one of the most important challenges in this way of materials preparations, especially in the case of nanomaterials synthesis. Recently, a number of publications show different possibilities for supercritical fluids reactor's design. For example, Demoisson et al. [134] have reported the design of the continuous reactors for the synthesis of nanomaterials in supercritical water. More recently, Marre et al. [135] reported a number of different flow-through microreactors which allow working with supercritical microfluids. It allows a perfect control of the operating parameters during the synthesis of different types of nanomaterials. Recently, in situ synchrotron powder diffraction techniques were adopted for the investigation of the inherent properties of SCFs such as their characteristic density fluctuations [136], a catalyst in an oxidation process in supercritical CO_2 [137], the fundamental behavior of metal salts in SCFs [138]. The first real time in situ synchrotron powder diffraction characterization of nanoparticles formation in SCFs has been reported by Jensen et al. [139]. They were studied the crystallization of anatase TiO_2 nanoparticles in supercritical CO_2. It was demonstrated that the nanoparticles formation follows the same progression as it is observed in the case of solvothermal method but on a much shorter time scale and at lower temperature. Thereby, SCFs technology offers the production of the nanomaterial into a new time domain which is much faster than for traditional methods.

Continuous supercritical fluids method was adopted for the synthesis of ZnO nanomaterials using different solvents such as water, methanol and ethanol. Sue et al. [140] reported continuous synthesis of ZnO nanoparticles in supercritical water using a flow type apparatus for rapid heating

of zinc nitrate precursor and KOH at 30 MPa and temperatures ranging from 573 to 673 K. ZnO nanoparticles with different sizes were obtained depending on temperature and residence time. They also used to change the diameter of the reactor's flow tube from 0.15 up to 2.38 mm. In this case the size of ZnO nanoparticles was increasing form 23 up to 57 nm. They attribute this changing in size of nanoparticles to the increase in heat-up time from the mixing point of $Zn(NO_3)_2$ and KOH to the mixing point with preheated water.

The organic solvents could be more usable as supercritical fluids than water for the synthesis of ZnO nanostructures due to their lower critical points (T, P). For example, Veriansyah et al. [141] have reported continuous synthesis of surface-modified ZnO nanoparticles in supercritical water and methanol at 400 ˚C, 30 MPa and a residence time of ~40 s (Figure I-22 A-D).

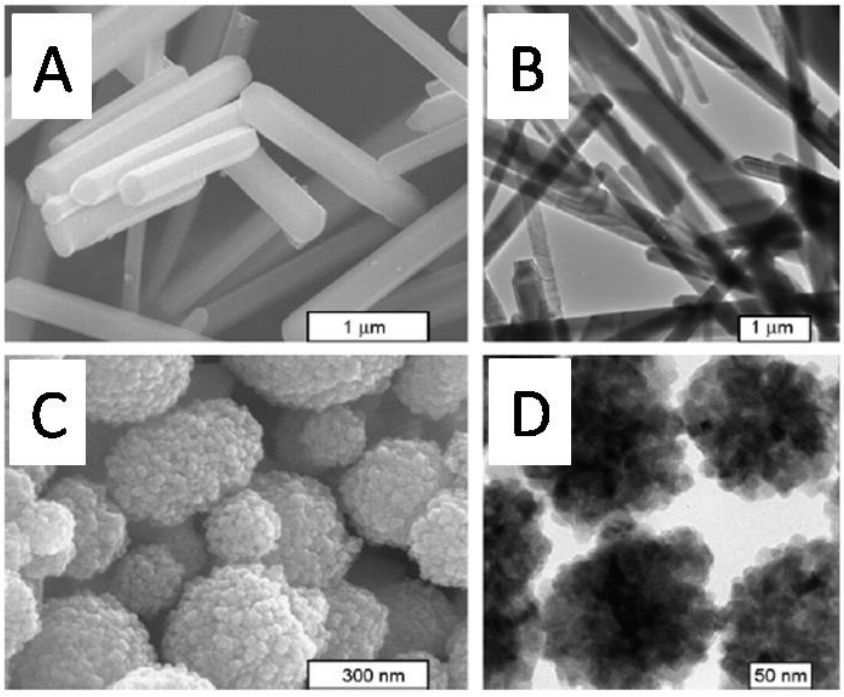

Figure I-22. ZnO nanoparticles obtained by Veriansyah et al. [141].

They were using oleic and decanic acid as surfactant. It was found that the surfactants changed the size and morphology of ZnO nanoparticles. When the molar ratio of oleic acid to Zn precursor was 30, 10 nm size ZnO nanoparticles with low degree of aggregation were produced. It was also noted

that the use of supercritical methanol and the surfactants changes the shape and size of nanoparticles. For example, nanorods shape particles with a clear faced were obtained when supercritical water was used whereas spherically shape particles with 130-360 nm in diameter were obtained with supercritical methanol. Synthesis of ZnO nanoparticles with different size and shape in supercritical water and methanol using oleic acid as surfactant was also reported by Han et al. [142]. They have shown that with the absence of surfactant, ZnO nanoparticles with a mean diameter of 15 nm formed secondary aggregates with a diameter about 150 nm, while interstitial zinc and oxygen vacancies were found to be a major defect. On the other hand, in the presence of oleic acid they form isolated nanoparticles with a mean diameter of 10 nm without interstitial zinc. ZnO nanoparticles obtained by supercritical water had nanowires shape. Figure I-23 shows spherical nanoparticles from supercritical methanol and nanowires from water.

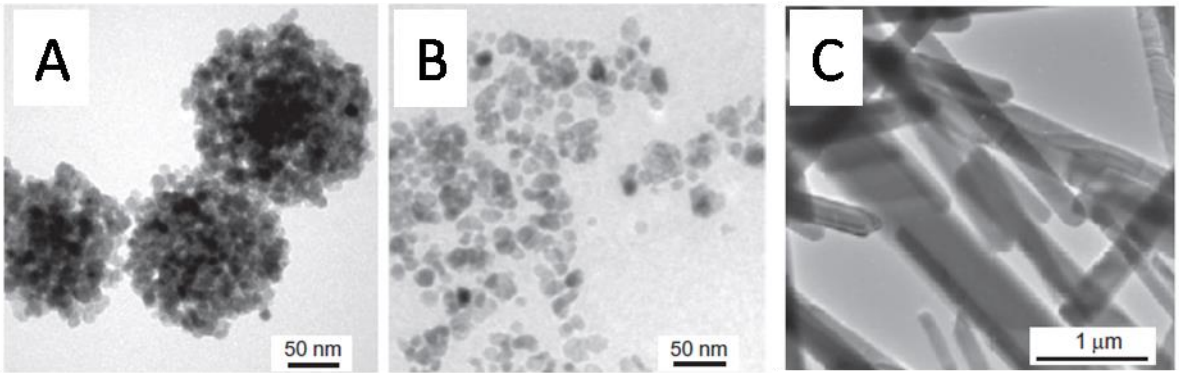

Figure I-23. ZnO nanostructures obtained by Han et al. [142].

At the ICMCB, ZnO nanocrystals were obtained in supercritical ethanol using an original continuous co-flow set-up (Figure I-24) [143]. This process was provided by the transformation of zinc acetylacetonate monohydrate $Zn(acac)_2 \cdot H_2O$ in the presence of H_2O_2 and ligands such as trioctylphosphine (TOP), oleylamine (OL) and oleic acid (OA). In these conditions, small spherical ZnO nanocrystals were formed with a size about 3.7 nm (Figure I-25). Room temperature photoluminescence spectra of obtained ZnO nanocrystals were also investigated and it was shown

that all spectra exhibit only UV emission at 377 nm which has been attributed to the excitonic recombination.

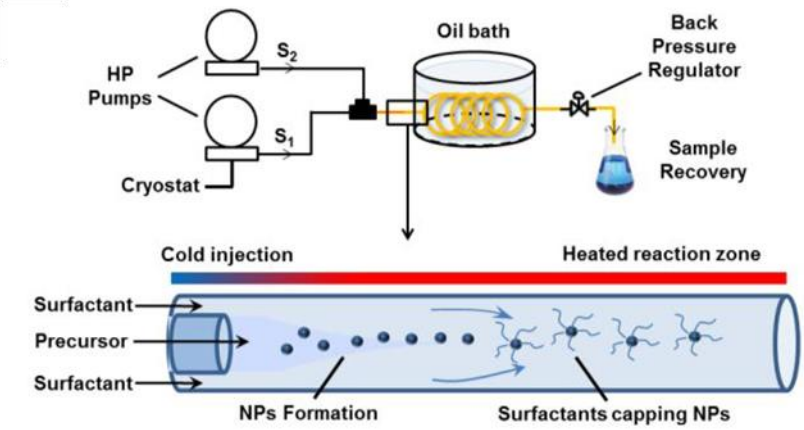

Figure I-24. Experimental supercritical microfluidic technique developed for the synthesis of ZnO nanoparticles [143].

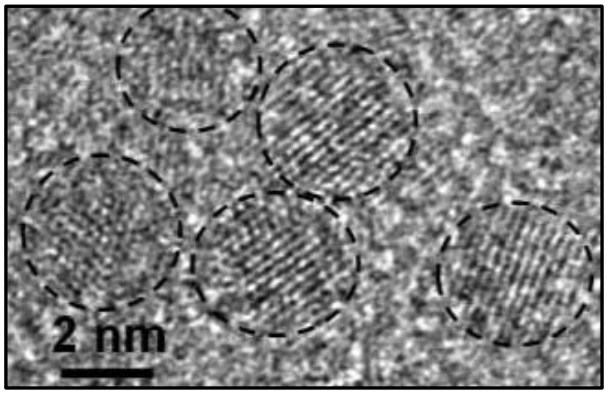

Figure I-25. HRTEM image of ZnO nanocrystals with a size about 3.7 nm [143].

In addition, SCFs approach allows the preparation of a high quality ZnO nanomaterial with a good control of size and morphology of this material. It should be noted that the continuous methods in SCFs approach allow obtaining of the material with a very low production time, for example, as in the case of Roig production time is only 10 s.

In conclusion, supercritical fluids approach is very promising technique for the fabrication of high crystalline ZnO nanostructures with controlled size and morphology. This can be achieved due to the combination of the properties which inherent for traditional approaches as high temperature

gas phase and low temperature liquid phase approach. From one point, high operating temperature used in SCFs leads to high crystallinity of the material while; from the other point, still liquid phase allows inviting different surfactant systems in order to control size and shape of the nanomaterial.

As it was mentioned before, the synthetic methods developed for the fabrication of ZnO nanostructures could be divided in three approaches regarding to optical properties of this material. The evolution of optical properties of ZnO nanostructures as a function of the synthetic approach is demonstrated in next paragraph of this chapter.

IV. Evolution of optical properties of ZnO nanostructures as a function of the synthetic approach

Introduction

As it was discussed in the previous section of this chapter, ZnO nanostructures exhibit two types of PL emission in UV and visible range of the spectrum. The physico-chemical characteristics of ZnO nanostructures such as size, shape, crystallinity etc. play an important role in determining the optical properties of these nanostructures. ZnO nanostructures can be prepared with various physico-chemical characteristics depending on the applied synthetic method. For example, low temperature liquid phase approach allows preparation of ZnO nanostructures with a large dispersion of sizes and morphologies, while high temperature gas phase approach allows improving crystallinity of this material thanks to high operating temperature used in this method. However, ZnO nanostructures obtained using both these approaches demonstrate mostly two types of PL emission in UV and visible part of PL spectra. Regarding this, it is a big challenge to develop synthetic method which allows obtaining ZnO nanostructures with high and efficient UV emission

only in their PL spectra. This section provides some discussions concerning the optical properties of ZnO nanostructures obtained using different types of synthetic approaches.

IV-1. Characteristic optical properties of ZnO nanostructures obtained by high temperature gas phase approach

The size and morphology control of ZnO nanostructures in high temperature gas phase approach is poorer than in the case of low temperature liquid phase methods. High temperature gas phase approach allows obtaining ZnO nanostructures with mostly rod-like morphology. The-Long Phan et al. [144] have studied the room temperature PL properties of many ZnO rods, wires, needles, tetrapods and multilegs with size between 20 and 1000 nm obtained by CVD method at 450-640 ˚C. PL spectra of these nanostructures consist of two emissions in UV and green region. They observed that the ratio of UV and green emission intensities strongly depends on size and morphology of ZnO nanostructures. Nanorods with 20-50 nm diameter and nanostructures with sizes varying from 50 to 200 nm exhibit more intensive green emission in comparison with UV, while the other samples with a larger size have usually UV emission stronger than green. The domination of green emission on UV for small sizes of ZnO nanocrystals obtained by CVD could be explained by a larger surface-to-volume ratio in the case of small size nanostructures. These results are in good agreement with Al-Salman et al. [145] which have reported room temperature PL studies of large multi-oriented spear-like ZnO nanorods with diameters between 180-255 nm and length about 2.1-2.5 μm, synthesized using CVD at 700 ˚C (Figure I-26-A).

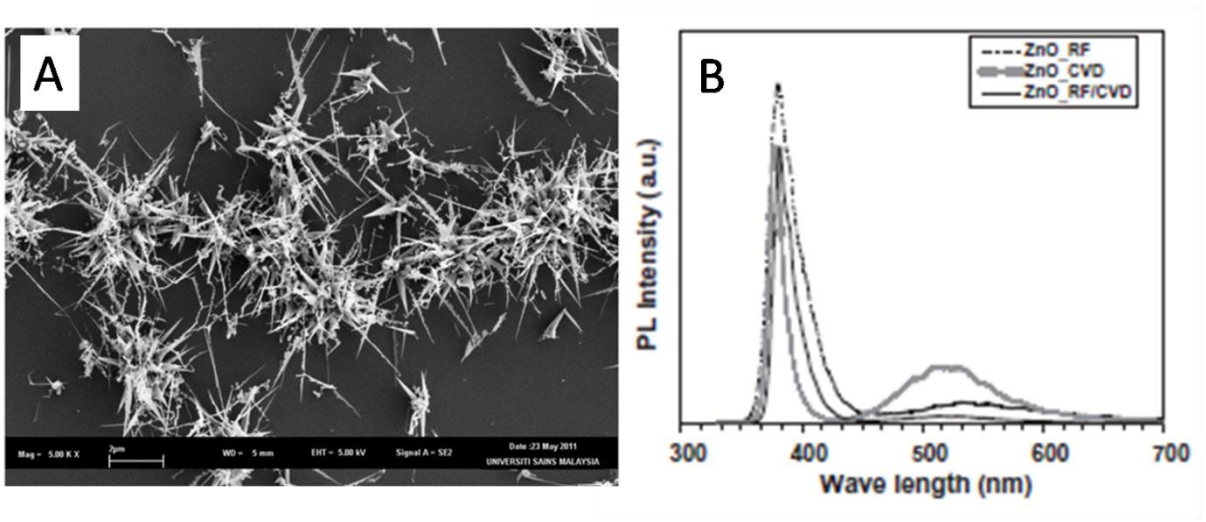

Figure I-26. Multi-oriented spear-like ZnO nanorods obtained by Al-Salman et al. [145] by CVD (A) and their PL spectra (B).

They observed a strong and dominated UV emission located at 382 nm in PL spectra (Figure I-26-B). In this report, UV-to-visible PL intensity ratio was of a factor 42. Cai et al. [146] have measured PL spectra of a quite big awl-like ZnO nanostructures with length about 1.8-2.6 μm and diameter of 0.6-1.3 μm obtained using CVD method at 1000 ˚C (Figure I-27-A). However, in this case, the intensity of visible emission at 523 nm was higher than intensity of UV line located at 380 nm (Figure I-27-B).

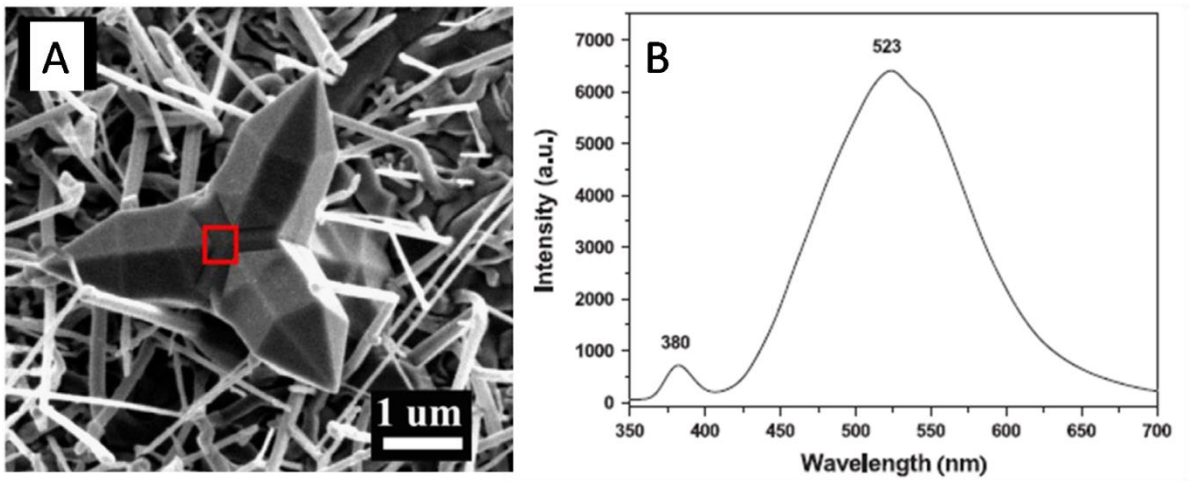

Figure I-27. ZnO nanostructures obtained by Cai et al. [146] by CVD (A) and their PL spectrum (B).

As it was discussed before, PVD method was also applied for the synthesis of ZnO nanostructures. Optical properties of different ZnO rod-like nanostructures obtained by PVD at 525 ˚C have been investigated by Yan et al. [147]. In this report ZnO nanostructures were formed in different types of rod-like morphologies such as nanocandle arrays, wine-bottle-shaped rod arrays, nanorivet arrays, nanorods etc. with length and diameter of about 2 μm and 200-500 nm, respectively (Figure I-28-A). Room temperature PL spectrum of ZnO nanorods obtained in this report is shown in Figure I-28-B. PL spectrum consists of a narrow dominated UV peak located at 388 nm and a weak broad band in the blue region. The weak blue emission band is related to some deep levels induced by defects which are originated from oxygen vacancies. In this report, a weak blue emission in comparison with strong intensive UV emission shows that ZnO nanostructures are highly crystalline with a few defects thanks to high operating temperature.

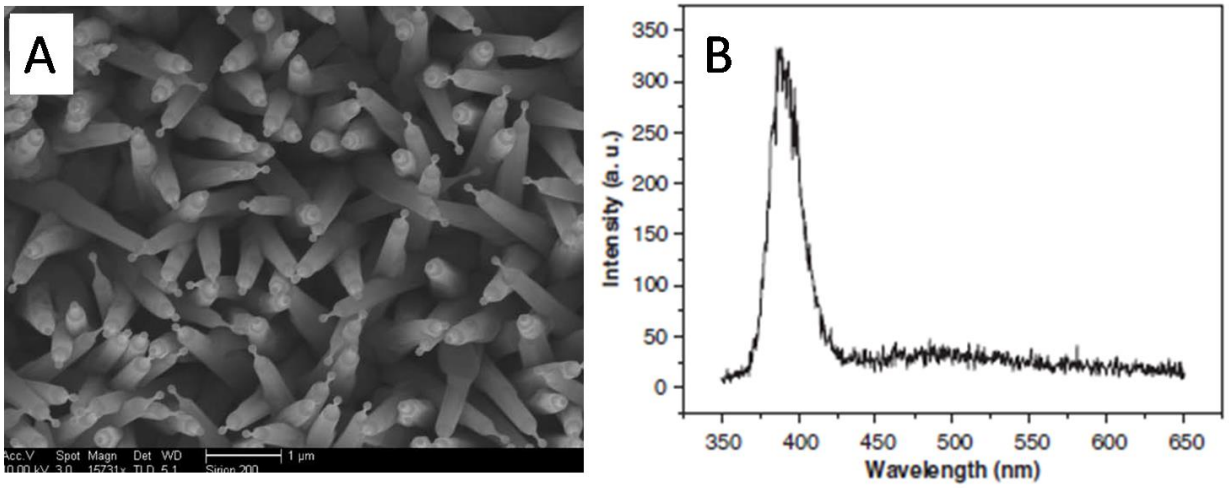

Figure I-28. ZnO nanocandle arrayobtained by Yan et al. [147] by PVD (A) and their PL spectrum (B).

Borkar et al. [148] have reported the deposition of nanocrystalline ZnO films with thicknesses of 5, 10, 20 and 50 nm onto the surface of vertically aligned carbon nanotubes. PL spectra of ZnO nanocrystalline films strongly depend on the thickness of the film. The intensity of UV line at 385 nm is increasing with increasing of the film thickness.

In conclusion, ZnO nanostructures obtained by high temperature gas phase approach demonstrate high crystallinity thanks to high operating temperature used in this method. High crystallinity allows avoiding bulk defects. This leads to the appearance of high intensive UV emission in PL spectra. ZnO nanostructures obtained by high temperature gas phase approach still have a visible emission originated from surface defects which contribute due to high surface area. However, the intensity of the visible line is decreasing with decreasing of surface-to-volume ratio.

IV-2. Characteristic optical properties of ZnO nanostructures obtained by low temperature liquid phase approach

As it was mentioned before, ZnO nanostructures obtained using low temperature liquid phase approach also demonstrate two types of PL emissions in their PL spectra. Room temperature PL spectra of spherical ZnO nanoparticles with a crystalline size of 5 nm obtained using co-precipitation method (aqueous solution growth) at 53 ˚C have been measured by Kripal et al. [149]. They observed UV emission peak at 395 nm and also more intensive visible emission lines attributed to zinc interstitials and oxygen vacancies. Shinde et al. [150] have studied room temperature PL spectra of ZnO nanopowders synthesized by co-precipitation method followed planetary ball milling of the nanopowder in order to reduce nanoparticle size. In this report, ZnO nanopowders were precipitated using zinc chloride and aqueous ammonia as starting materials at room temperature, the precipitate was annealed at 500 ˚C to remove hydroxyl groups and to form stable ZnO powder. This powder employed further planetary ball milling for 450 rpm for 0 h, 3 h and 5 h to obtain ZnO nanoparticles with crystalline size of 10.28 nm, 9.78 nm and 8.99 nm, respectively (Figure I-29-A).

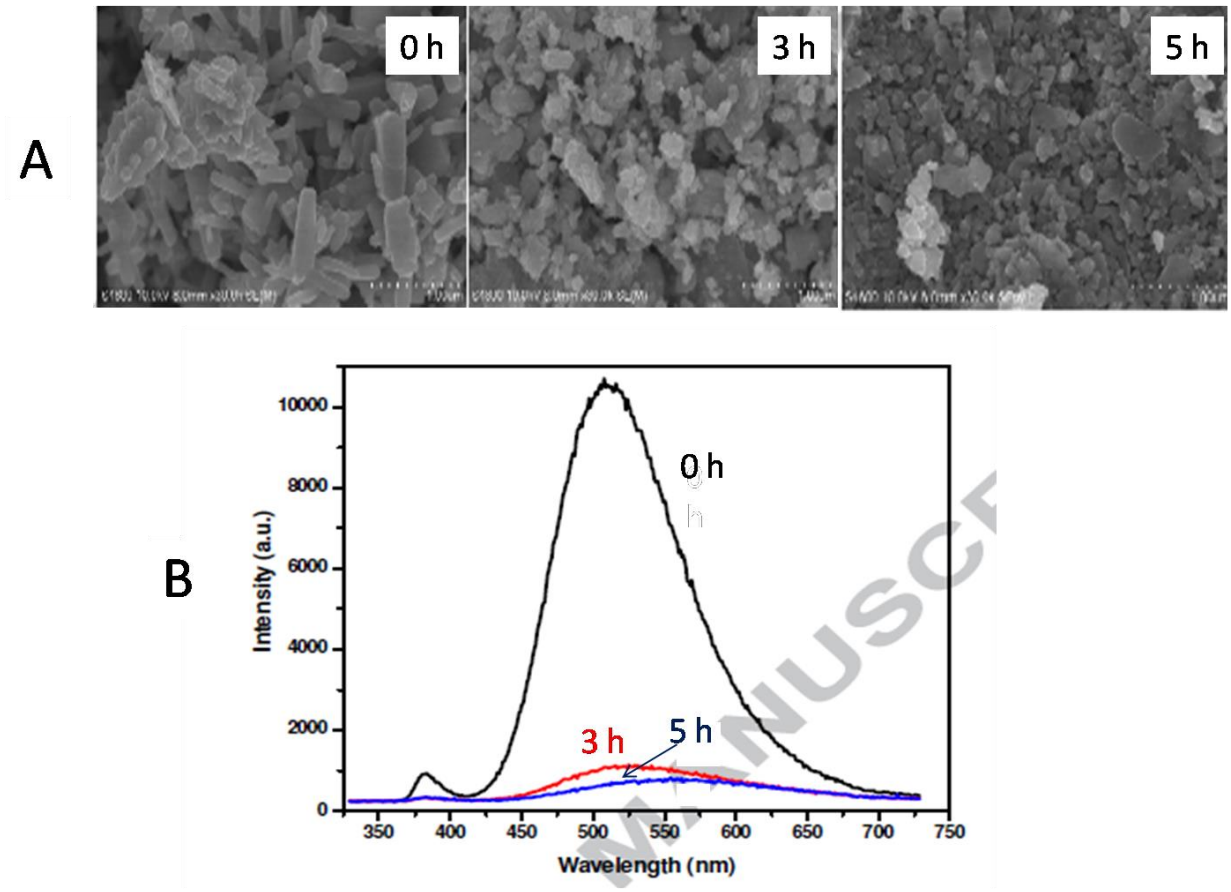

Figure I-29. ZnO nanopowders synthesized by Shinde et al. [150] using co-precipitation method with further planetary ball milling for 450 rpm for 0 h, 3 h and 5 h (A) and their room temperature PL spectra.

Room temperature PL spectra of these nanopowders are shown in Figure I-29-B. The PL spectra have two peaks in UV and green regions at 385 nm and 520 nm, respectively. The emission intensities were significantly weakened with the increase in ball milling for 0 h, 3 h and 5 h of ZnO nanopowders. Authors explain it through the suppression of the recombination of charge carriers in oxygen vacancies.

As it was discussed before, ZnO nanostructures obtained using organometallic method usually exhibit small nanoparticles size. This makes a large surface-to-volume ratio of the nanoparticles and as a consequence, visible emission originated from the surface defects dominates in their PL spectra. Optical properties of ZnO nanostructures prepared by organometallic synthetic method have also been investigated [106-107, 151]. For example, Kahn et al. [106] have reported

organometallic synthesis of spherical ZnO nanoparticles with a crystalline size of 3 nm and 6 nm and ZnO nanorods with a mean diameter of 3-4 nm and length up to 120 nm in (all details concerning the synthesis of these nanoparticles in this publication were described in previous paragraph). Their PL spectra exhibit very week UV emission at 370 nm and intensive visible emission band centered at 585 nm (Figure I-30).

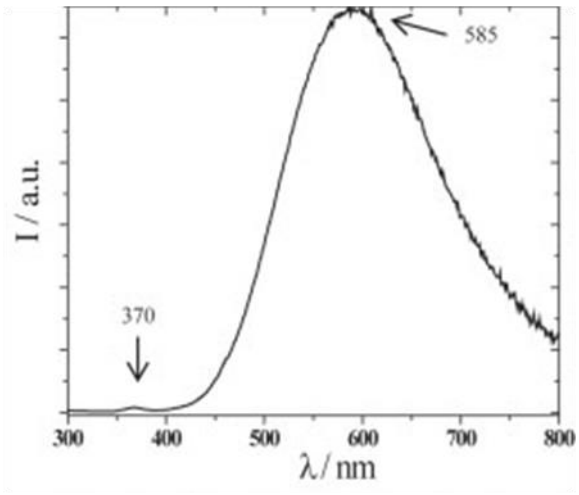

Figure I-30. Room temperature PL spectrum of ZnO nanoparticles obtained by the organometallic method by Khan et al. [106].

The same authors [151] have studied the emission properties of spherical ZnO nanoparticles and ZnO nanorods. They observed for the first time two main broad emission bands in the visible range at the same time centered at 440 nm and 580 nm, a weak UV emission is also observed at around 370 nm (Figure I-31).

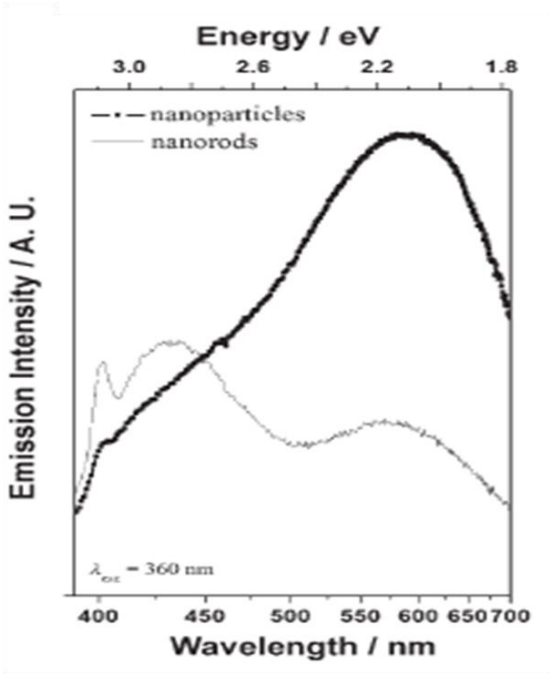

Figure I-31. Room temperature PL spectra of ZnO nanoparticles and nanorods obtained by the organometallic method by Khan et al. [151].

The same group has also reported the synthesis and optical properties of ZnO nanostructures by organometallic method using Li ions as growth controlling agent [107]. The increase of Li/Zn molar ratio induces increasing of the mean nanoparticles size from 2.5 to 4.3 nm and, as a consequence, size variation leads to a shift of the emission band from yellow to blue through white as a function of Li/Zn molar ratio.

Optical properties of ZnO nanostructures synthesized by sol-gel method have also been investigated [50, 152-153]. In 1991, Spanhel et al. [50] reported optical properties of colloidal ZnO nanocrystals with a crystalline size of 3-6 nm obtained by sol-gel method. They observed a visible emission peak at 500 nm which is shifted to 560 nm with aging of the colloid. This shift indicates the growth of larger ZnO nanocrystals. A few years later, Monticone et al. [152] have also published PL investigation of colloidal ZnO nanoparticles with size obtained by sol-gel. PL spectra of these nanoparticles consists of a weak UV emission centered at 375 nm and intensive, in comparison with UV, green and blue emission bands located at 510 and 430 nm, respectively.

As in the case of Spanhel, UV and both visible emissions also depend on shifting during colloid aging. UV emission shifts to the blue region with decrease of the particle size, while both visible emission bands undergo a red shift with an increase of the particles size. One interesting study has been performed by Guo et al. [153] corresponding to the optical properties of ZnO nanoparticles synthesized using poly-(vinylpyrollidone) (PVP) as capping agent with the sol-gel technique. They observed the evolution of room temperature PL spectra as a function of Zn/PVP molar ratio (Figure I-32).

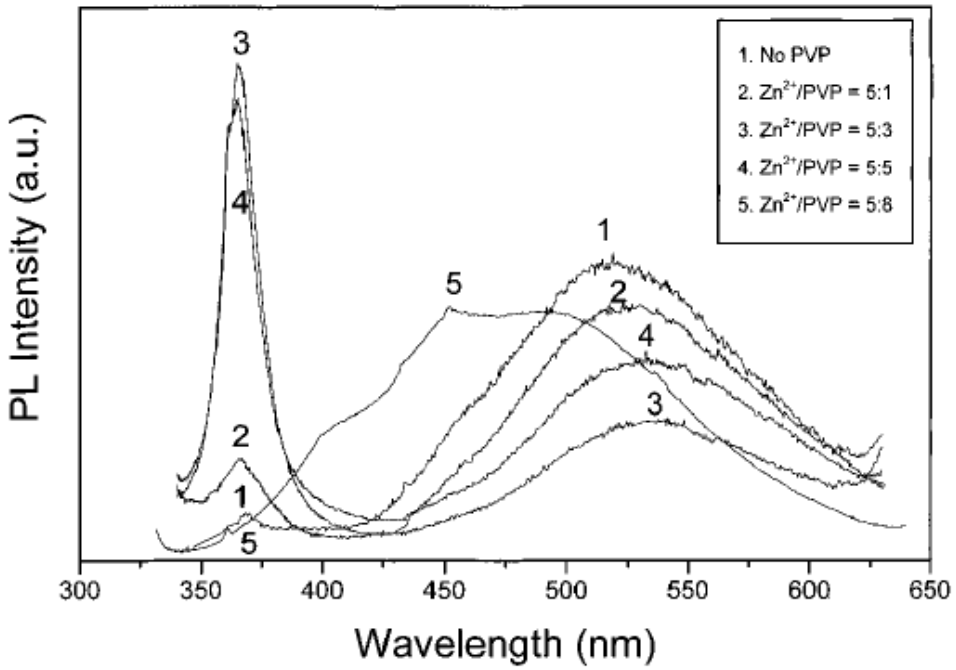

Figure I-32. The evolution of room temperature PL spectra of ZnO nanoparticles as a function of Zn/PVP molar ratio observed by Guo et al. [153].

Initially, ZnO nanoparticles obtained without adding PVP exhibit a weak UV emission at 365 nm and strong green band at 530 nm. However, the UV emission peak increases in intensity with adding PVP and started to be dominant at optimal Zn/PVP molar ratio equal to 5/3. The quenching of the green emission with the increase of PVP concentration takes place due to the interaction between PVP and ZnO nanoparticles surface avoiding surface defects in ZnO.

Optical properties of ZnO nanostructures synthesized using solvo- or hydrothermal method are also reported in literature [154-158]. Generally, PL spectra of these nanostructures demonstrate two types of PL emission in UV and visible regions. However, UV emission peak is usually less intensive than visible band due to large surface-to-volume ratio of the nanostructures obtained through this method. Aslani et al. [154] reported room temperature PL properties of spherical ZnO nanoparticles synthesized by solvothermal method at 150 ˚C. Their PL spectrum consists of UV emission at 385 nm and more intensive visible emission band centered around 550 nm. A similar PL behavior of various ZnO nanostructures fabricated using solvothermal method were observed by a number of researchers: Yang et al. [155] observed UV emission at 390 nm and two visible emission bands located at 580 nm and 630 nm; Liu et al. [156] reported a shoulder of UV emission at 390 nm and visible emissions at 435 nm and 467 nm; Ye et al. [157] have published PL spectra of ZnO nanorods with UV emission line centered between 380 and 390 nm, while visible emission band was located in the range of 470-630 nm; very recently, Pal et al. [158] reported UV emission of ZnO nanorods at 381 nm and visible emission band ranging from 450 nm to 730 nm. Interestingly, some researchers have tried to quench the visible emission band through the improving of the ZnO nanostructures quality in order to obtain a stronger UV emission in PL spectra. For example, in Yang experiments, the relative intensity of the visible emission was reduced in two times by changing the precursor concentration (Figure I-33).

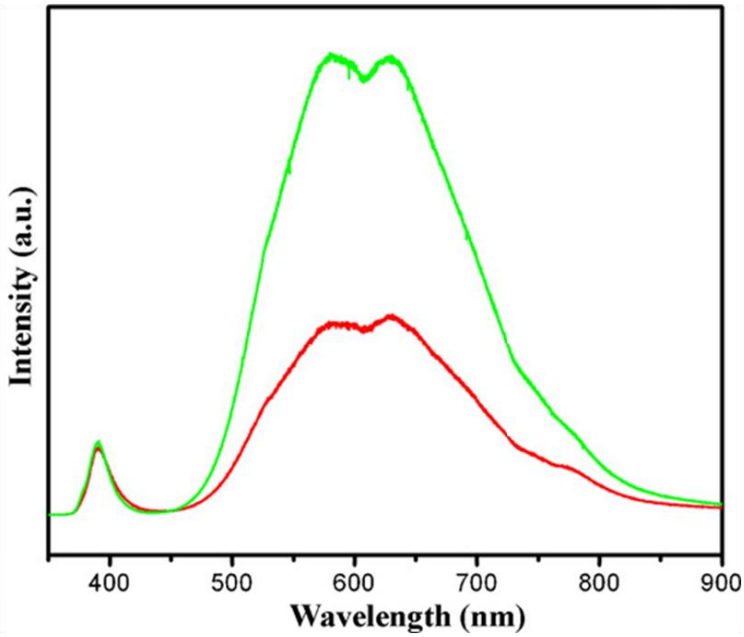

Figure I-33. Room temperature PL spectra obtained by Yang et al. [155] at 0.1 M (green line) and 0.01 M (red line) of $Zn(NO_3)_2$.

The other way to reduce the contribution of the visible emission has been demonstrated by Pal. The relative intensity of the visible emission was reduced by the incorporation of Co^{2+} ions in ZnO nanorods. In this case, doped cations could play a role of possible pathways for recombination, nonradiative process or charge transfer resulting the quenching of the visible emission (Figure I-34).

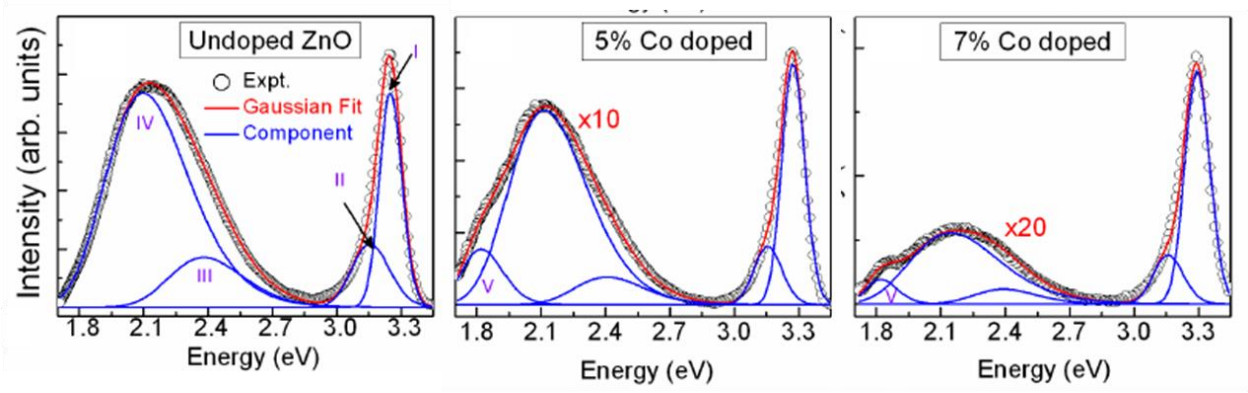

Figure I-34. PL spectra of undoped and Co-doped ZnO nanorods measured by Pal et al. [158].

In conclusion, as it was discussed in the previous paragraph, ZnO nanostructures fabricated using low temperature liquid phase approach exhibit small size and various morphologies thanks to

different surfactants systems invited in this approach. A small size of the nanostructures makes a large surface area and low operating temperature and results in a poor crystallinity of these nanostructures. This makes a large number of surface and bulk defects in ZnO nanostructures resulting in a strong visible PL emission in their PL spectra, while UV emission is less intensive or fully quenched. As it is shown in literature, there are some methods which allow improving a quality of ZnO nanocrystals leading to the reducing of the visible emission. However, according to the best of our knowledge, there is no reported fabrication of pure UV-emitting ZnO nanostructures by low temperature liquid phase approach.

IV-3. Trends in optical properties of ZnO nanostructures obtained by supercritical fluids approach

As it was discussed above, supercritical fluids approach is a recent developed method for the synthesis of ZnO nanostructures. This approach combines a relatively high operating temperature, as it is typical for high temperature gas phase approach, creating high crystallinity of the nanomaterials and this is still liquid phase method which allows involving different surfactant systems making possible size and morphology control of ZnO nanostructures. Such features are very interesting in term of Materials Science especially regarding the fabrication of future optical material based on ZnO nanostructures i. e. high crystallinity allows expecting UV-emitting PL properties; keeping good size and morphology control.

There are a few reports concerning optical properties of ZnO nanostructures obtained using supercritical fluids. For example, Ohara et al. [159] have published continuous production of highly crystalline ZnO rods with the mean diameter and length of 150 nm and 600 nm, respectively, in supercritical water at 400 ˚C and 30 MPa (Figure I-35-A). Room temperature PL

spectrum of these nanorods consist from a strong UV emission peaked at 380 nm and weak visible emission located at around 550 nm (Figure I-35-B).

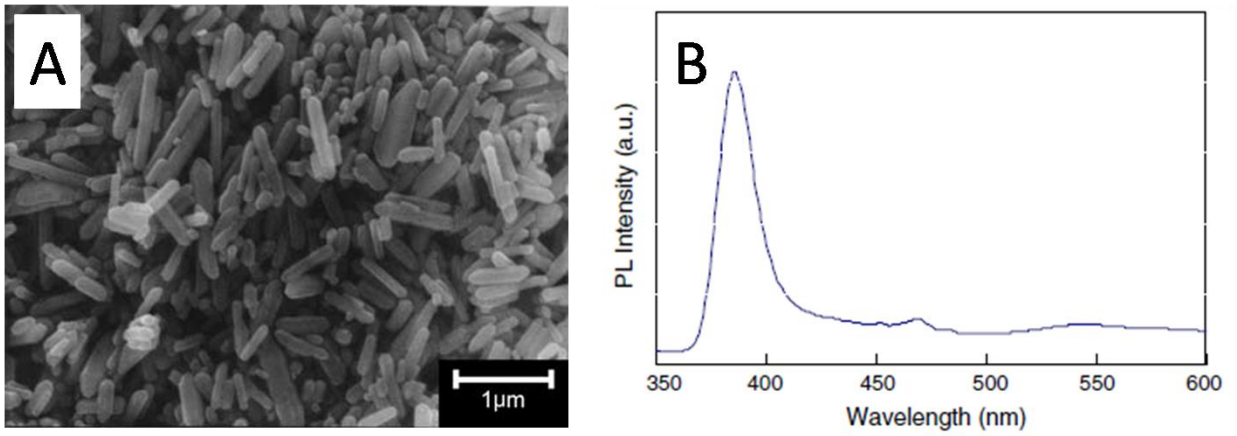

Figure I-35. ZnO rods obtained by Ohara et al. [159] by supercritical fluids approach (A) and their PL spectrum (B).

Han et al. [142] have investigated optical properties of smaller ZnO nanostructures obtained continuously in supercritical methanol and water (all details concerning this report are discussed in the previous paragraph). Their PL spectra consist of strong UV emission peak located at 382 nm and visible emission bands at 500 and 560 nm. The visible emission band was attributed to the defect states in ZnO, which could be originated from the surface states.

Supercritical fluids approach has been adopted for the synthesis of spherical ZnO nanocrystals with size of a few nm using oleylamine (OL), oleic acid (OA) and trioctylphosphine (TOP) as ligands in ICMCB by Roig et al. [143]. PL spectra of these nanocrystals exhibit only one intensive and narrow UV emission peaked at 378 nm (Figure I-36). Such PL behavior of the nanocrystals prepared by Roig et al. is very surprising. From one point, high operating temperature used in this synthesis allows production highly crystalline nanocrystals without bulk defects and as a consequence, the visible emission originated from this type of defect could be fully quenched. From the other point, small size makes a large surface area in these nanocrystals; this should lead to the appearance of a large number of surface defects as it was observed for ZnO nanostructures

fabricated by high temperature gas phase and low temperature liquid phase approaches. However, the absence of any type of the visible emission shows that surface defects are also absent.

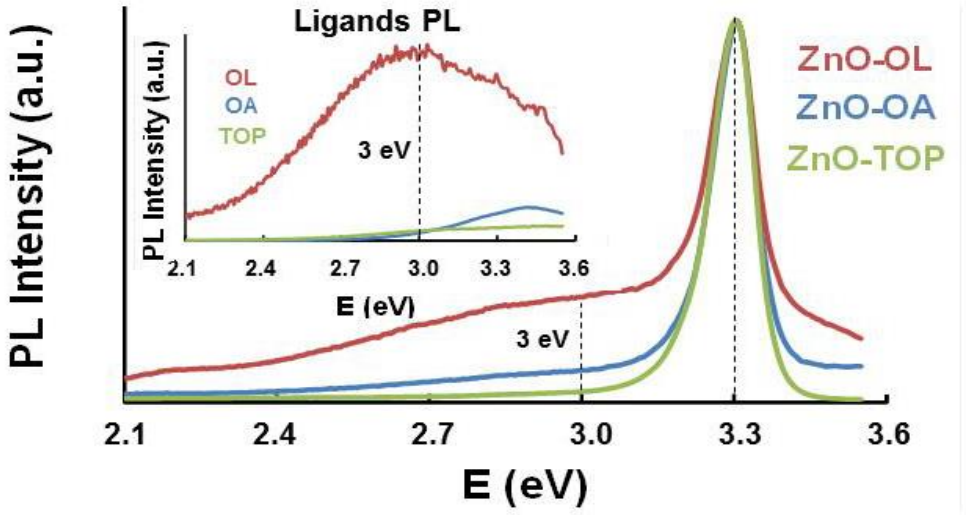

Figure I-36. Room temperature PL spectra of ZnO nanocrystals measured by Roig et al. [143].

This Ph.D. thesis is a continuation of Roig work concerning supercritical fluids based synthesis of ZnO NCs and deep investigation of the physico-chemical characteristics including their optical properties. As it was discussed above, Roig et al. have developed an original method for the synthesis of UV-emitting only ZnO NCs however, the production rate in this work was very low (only a few mg per day) which made deep characterization of ZnO NCs difficult. According to this, the first objective of this Ph.D. project is to increase the production rate of ZnO NCs through the scale up of our supercritical fluids based set up (from micro- up to millifluidic scale) which allows obtaining a larger quantity of this material. The second objective of this Ph.D. is a deep characterization of physico-chemical properties of ZnO NCs thanks to a larger quantity of the material available through the millifluidic dimension of our supercritical set up. The third objective is the evaluation of ZnO NCs formation mechanism in supercritical fluids in order to understand such unique physico-chemical characteristics of this material (e. g. UV-emitting only optical

behavior). The last objective of this Ph.D. thesis is a deep investigation of optical properties for the understanding the nature of UV emission exhibiting by ZnO NCs obtained using our supercritical fluids approach.

References:

1. H. D. Sun et al. Appl. Phys, Lett., 2001, 78, 2464.
2. L. Vayssierer, Adv. Mater. (Weinheim, Ger), 2003, 15, 464.
3. M. H. Huang et al. Adv. Mater. (Weinheim, Ger), 2001, 13, 113.
4. H. D.Yu et al. J. Am. Chem. Soc. 2005, 127, 2378.
5. Z. L. Wang, J. Phys. Condens. Mat., 2004.16, R829.
6. W. D. Yuet al. Cryst. Grow. Des., 2005, 5, 151.
7. C. H. Bates et al. Science (Washington, D.C. U.S.), 1962, 137, 993.
8. W. Bragg, Transact. Farad. Soc., 1932, 28, 522.
9. M. L. Fuller, Science (Washington, D.C. U.S.), 1929, 70, 196.
10. K. Ueda et al. Appl. Phys. Lett., 2001, 79, 988.
11. N. S. Norberg et al. J. Am. Chem. Soc., 2004, 126, 9387.
12. L. El Mir et al. Phys. Status Solidi A., 2007, 204, 3266.
13. R. Tena-Zaera, et al. J. Cryst.Growth, 2004, 270, 711.
14. V. Munoz-Sanjose et al. Phys. Status Solidi. , 2005, 2, 1106.
15. A. B. Djurišić et al. Small, 2006, 2, 944.
16. A. B. Djurišić, et al. Ad. Funct. Mater., 2004, 14, 856
17. A. Dijken et al. J. Lumin., 2000, 90, 123.
18. C. F. Klingshirn, Semiconductor Optics, Third Edition., Springer, Heidelberg, 2006.
19. C. F. Klingshirn, ChemPhysChem, 2007, 8, 782
20. R. Hauschild et al. Phys. Status Solidi C, 2006, 3, 976.
21. R. Thonke et al. Solid State Phys., 2004, 146, 73.
22. B. K. Meyer et al. Phys. Status Solidi B, 2004, 241, 231.
23. C. H. Ahn et al. Appl. Phys. Lett., 2009, 94, 261904.
24. Priller. et al. Phys. Status Solidi B, 2004, 241, 587.
25. B. Lin et al. Appl. Phys. Lett., 2001, 79, 943.
26. P. S. Xu et al. Nucl. Instrum. Methods Phys. Res. B, 2003, 199, 286.

27. A. Kobayashi et al. Phys. Rev. B, 1983, 28, 946.
28. C. X. Xu et al. Nanotechnology, 2004, 15, 856.
29. D. C. Reynolds et al. J. Appl. Phys., 2001, 89, 6189.
30. Q. X. Zhao et al. Appl. Phys. Lett., 2005, 87, 211912.
31. K. Vanheusden et al. Appl. Phys. Lett., 1996, 68, 403.
32. Y. G. Wang et al. Chem. Phys. Lett., 2003, 375, 113.
33. T. Andelman et al. J. Phys. Chem. B, 2005, 109 (30) 14314.
34. S. Sakohara et al. J. Phys. Chem. B, 1998, 102 (50) 10169.
35. G. Lin et al. Appl. Phys. Lett., 2000, 76 (20) 2901.
36. Y. Gong et al. Nanoscale Res.Lett., 2007, 2, 297.
37. N. E. Hsu et al. Appl. Phys. Lett., 2004, 96, 4671.
38. L. E. Greene et al. Angew. Chem., 2003, 115, 3030.
39. H. T. Hg et al. Appl. Phys. Lett., 2003, 82, 2023.
40. D. Li et al. Appl. Phys. Lett., 2004, 85, 1601.
41. Y. W. Heo et al. J. Appl. Phys., 2005, 98, 073502.
42. H. J. Fan et al. Appl. Phys. Lett., 2004, 85, 4142.
43. Z. Chen et al. Scr. Mater., 2005, 52. 63.
44. H. J. Fan et al. Appl. Phys. A, 2004, 79, 1895.
45. A. B. Djurišić et al. Appl. Phys. Lett., 2006, 88, 103107.
46. L. Wu et al. Opt. Mater., 2006, 28, 418.
47. W. M. Kwok et al. Appl. Phys. Lett., 2005, 87, 093108.
48. R. B. M. Cross et al. Nanotechnology, 2005, 16, 2188.
49. A. B. Djurišić et al. Nanotechnology, 2007, 18, 095702.
50. L. Spanhel et al. J. Am. Chem. Soc., 1991, 113, 2826.
51. R. Tena-Zaera, et al., J. Cryst.Growth, 2004, 270, 711.
52. V. Munoz-Sanjose et al., Phys. Status Solidi C., 2005, 2, 1106.
53. J. –J. Wu et al. J. Phys. Chem. B 2002, 106, 9546-9551.

54. Z. Zhang et al. J. Phys. Chem. C 2007, 111, 17500.
55. R. J. H. Morris et al. Surf. Interface anal. 2007, 39, 898.
56. B. D. Yao et al. Appl. Phys. Lett. 2002, 81, 757.
57. M. H. Huang et al. Adv. Mater. (Weinheim, Ger), 2001, 13, 113-116.
58. O. Tigli et al. Conference on Nanotechnology (IEEE-Nano) ISBU 978-1-4577-1514., 2011, 608.
59. G. Jimenez-Cadena et al. Mater. Chem. Phys., 2010, 124 (1), 649.
60. A. K. Gupta et al. Biomaterials, 2005,26, 3995.
61. S. Laurent et al. Chem Rev., 2008, 108, 2064.
62. A. Thünemann et al. Langmuir, 2006, 22, 2531.
63. R. Massart, IEEE TransMagn, 1981, 17, 1247.
64. J. P. Jolivet et al. Met. Clays Clay Mineral, 1992, 40(5), 531.
65. L. Babes et al. J. Colloid. Interface Sci. 1999, 212(2), 474.
66. W. Jiang et al. J. Magn. Magn. Mat. 2004, 283, 210.
67. L. Vayssières et al. J. Colloid Interface Sci. 1998, 205(2), 205.
68. Layek et al. Intern. J. Eng., Sci. and Technol., 2010, 2(8), 33.
69. T. P. Almeida et al. J. Phys. Chem. C,2009, 113,18689.
70. M. Mohapatra et al. Int. J. Eng., Sci. Technol., 2010, 2(8), 127.
71. S. D. Park et al. J. Solid State Chem., 1999, 146, 230.
72. M. Andres Verges et al. J. Chem. Soc., Farad. Trans., 1990,86, 959.
73. J.-P. Jolivet et al. J. Sol-Gel Sci. Technol., 2008, 46, 299.
74. E. Lori et al. Nano Lett., 2005, 5 (7), 1231.
75. L. Vayssieres et al. J. Phys. Chem. B, 2001, 105, 3350.
76. L. Vayssieres, Adv. Mater. (Weinheim Ger), 2003, 15, 464.
77. Y. Sun et al. J. Phys. Chem. B, 2006, 110, 15186.
78. Z. R. Tian et al. Nat. Mater., 2003, 2, 821.
79. Z. Chen et al. J. Cryst. Growth, 2006, 293, 522.

80. D. S. Boyle et al. Chem. Commun., 2002, 80.

81. Z. Wang et al. Langmuir, 2004, 20, 3441.

82. H. Zhang et al. Cryst. Grow. Des., 2005, 5, 547.

83. H. Zhang et al. Mater. Lett., 2005, 59, 1696.

84. K. Govender et al. J. Mater. Chem., 2004, 14, 2575.

85. F. Xu et al. J. Non-Cryst. Solids, 2006, 352, 2569.

86. C. Lu et al. Chem. Commun. 2006, 3551.

87. M. P. Pileni, J. Phys.Chem., 1993, 97, 6961.

88. M. Singhalet al. Mater, Res. Bull., 1997, 32, 239.

89. N. Nikolaeva et al. J. Siberian Federal University. Chemistry 2010, 2, 153.

90. Z. H. Zhang et al. Chem. Eur. J., 2007, 13, 632.

91. J. Joo et al. Adv. Mater. (Weinheim, Ger), 2005, 17, 1873.

92. T. Andelman et al. J. Phys.Chem. B, 2005, 109, 14314.

93. M. Epifani et al. Chem. Mater., 2005, 17, 6468.

94. S. H. Choi et al. J. Phys. Chem. B, 2005, 109, 14792.

95. Y. F. Chen et al. J. Am. Chem. Soc., 2005, 127, 13331.

96. M. Driess et al., Inorg. Chem., 2000, 2517.

97. V. Ischenkoet al. Adv. Funct. Mater., 2005, 15, 1945.

98. S. Polars et al. Small, 2005, 1, 540.

99. M. Driess et al. C. R. Chim. 2003, 6, 273.

100. T. J. Boyle et al. Chem. Mater. 2004, 16, 3279.

101. C. G. Kim et al. Chem. Commun., 2003, 2068.

102. C. Naural et al. Adv. Mater. (Weinheim, Ger), 1999, 11, 61.

103. K. Soulantica et al. Adv. Funct. Mater., 2003, 13, 553.

104. F. J. Rataboul, Organomet. Chem., 2002, 311, 643.

105. M. L. Kahn, J. Mater. Chem., 2009, 19, 4044.

106. M. L. Kahn et al. Adv. Funct. Mater., 2005, 15, 458.

107. A. Claria et al. New J. Chem. 2008, 32, 662.

108. M. Haase et al. J. Phys. Chem., 1988, 92, 482.

109. C. Pacholski et al. Angew.Chem. Int. Ed., 2002, 41, 1188.

110. J. B. Liang et al. J. Phys. Chem. B 2005, 109, 9463.

111. Z. R. R.Tian et al. Nat. Mater. 2003, 2, 821.

112. P. D. Garcia et al. Adv. Mater. (Weinheim, Ger), 2006, 18, 2768.

113. S. Kar et al. J. Phys. Chem. B, 2006, 110, 4605.

114. H. J. Fan et al. Small.2006, 2, 561.

115. X. D. Wang et al. J. Am. Chem. Soc, 2005, 127, 7920.

116. Q. Tang et al. Chem. Commun., 2004, 712.

117. B. Baruwati et al. Sens. Actuator A., 2006, 119, 676.

118. C. H. Lu et al. Ceram. Int. 2000, 26, 351.

119. D. Chen et al. Solid State Commun., 2000, 113, 363.

120. S. Musić et al. J. Alloys Compd., 2002, 347, 324.

121. F. Cansell et al. Curr. Op. Solid State Mater. Sc.,2003, 7, 331.

122. C. Aymonier at al. J. Supercrit. Fluids, 2006, 38, 242.

123. F. Cansell et al. J. Supercrit. Fluids, 2009, 47, 508.

124. A. Erriguible et al. J. Supercrit. Fluids, 2009, 48, 79.

125. R. Garriga et al. J. Supercrit. Fluids, 2001, 20, 55

126. V. Pessey et al. J. Mater. Chem., 2002, 12, 958.

127. S. Desmoulins-Krawies et al. J. Mater. Chem., 2004, 14, 228.

128. J. L. Bobed et al. J. Alloys Compd, 2033, 351, 217.

129. C. Slostowski et al. Langmuir, 2012, 28, 16656.

130. C. Slostowski et al. J. Supercrit. Fluids, 2013, 84, 89.

131. C. Slostowski et al. Langmuir, 2014, 30(20) 5965.

132. G. Philippot et al. J. Supercrit. Fluids, 2014, 87, 111.

133. O. Pascu et al. Nanoscale, 2013, 5, 12425.

134. F. Demoisson et al. J. Supercrit. Fluids, 2011, 58, 371.

135. S. Marre et al. J. Supercrit. Fluids, 2012, 66 251.

136. D. Testemale et al. Rev. Sci. Instrum. , 2005, 76, 1.

137. J. D. Grunwaldt et al. Catal. Lett., 2003, 90, 221.

138. V. Simonet et al. J. Chem. Phys., 2002, 117(6), 2771.

139. H. Jensen et al. Angew. Chem. Int. Ed., 2007, 46, 1113.

140. K. Sue et al. Green Chem., 2003, 5, 659.

141. B. Veriansyah et al. J. Supercrit. Fluids 2010, 52, 76.

142. N.S. Han et al. Chem. Phys. Lett. 2011, 505, 51.

143. Y. Roig et al. Angew. Chem. Int. Ed., 2011, 50, 12071.

144. The-Long Phan et al. J. Lumin., 2010, 130, 1142.

145. H. Al-Salman et al. J. Alloys Compd, 2013, 547, 132.

146. X. Cai et al. Ceram. Int., 2014, http://dx.doi.org/10.1016/j.ceramint.2014.04.074.

147. Y. Yan et al. J. Cryst. Growth, 2006, 294, 184.

148. T. Borkar et al. Mater. Res. Bull., 2012, 47, 2756.

149. R. Kripal et al. Spectrochim. Acta A, 2011, 79, 1605.

150. K. P. Shinde et al. Ceram. Int., 2014, http://dx.doi.org/10.1016/j.ceramint.2014.07.148.

151. M. L. Kahn et al. ChemPhysChem., 2006, 7, 2392.

152. S. Monticone et al. J. Phys. Chem. B, 1998, 120, 2854.

153. L. Guo et al. Chem. Mater., 2000, 12, 2268.

154. A. Aslani et al. Chem. Mater., 2010, 405, 3585.

155. Z. X. Yang, et al., J. Alloys Compd, 2011, 509, 3403.

156. Z. Liu et al. J. Phys. Chem. Sol., 2012, 73, 651.

157. N. Ye et al. Opt. Mat., 2012, 34, 753.

158. B. Pal et al. J. Alloys Compd., 2014, http://dx.doi.org/10.1016/j.jallcom.2014.06.087

159. S. Ohara et al. J. Mater. Sci., 2008, 43, 2393.

Chapter II

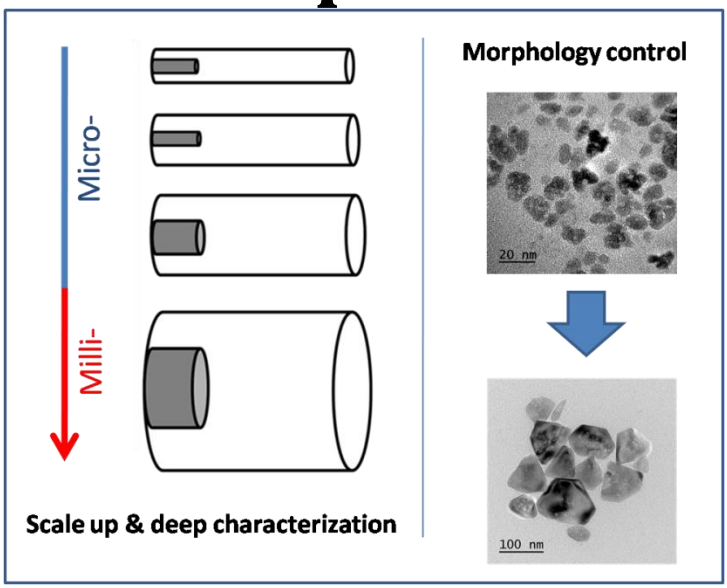
Micro-
Milli-
Scale up & deep characterization
Morphology control
20 nm
100 nm

Introduction

A supercritical fluids based (SCFs) approach has been developed at ICMCB for the synthesis of ZnO nanocrystals (NCs) with unique optical properties [1]. ZnO NCs were obtained through the oxidation of zinc acetylacetonate monohydrate ($Zn(acac)_2 \cdot H_2O$) by H_2O_2 in supercritical ethanol/water mixture at 250 ˚C and 25 MPa (molar ratio of ethanol/water=0.95/0.05; mixture critical temperature and critical pressure are equal to 245 ˚C and 7.5 MPa, respectively) using different surfactant systems such as oleylamine (OL), oleic acid (OA) and trioctylphosphine (TOP) for the NCs stabilization (Figure II-1-A). ZnO NCs obtained by this method exhibit UV emission with fully quenched visible emission in their PL spectra due to their high quality crystal properties (Figure II-1-B).

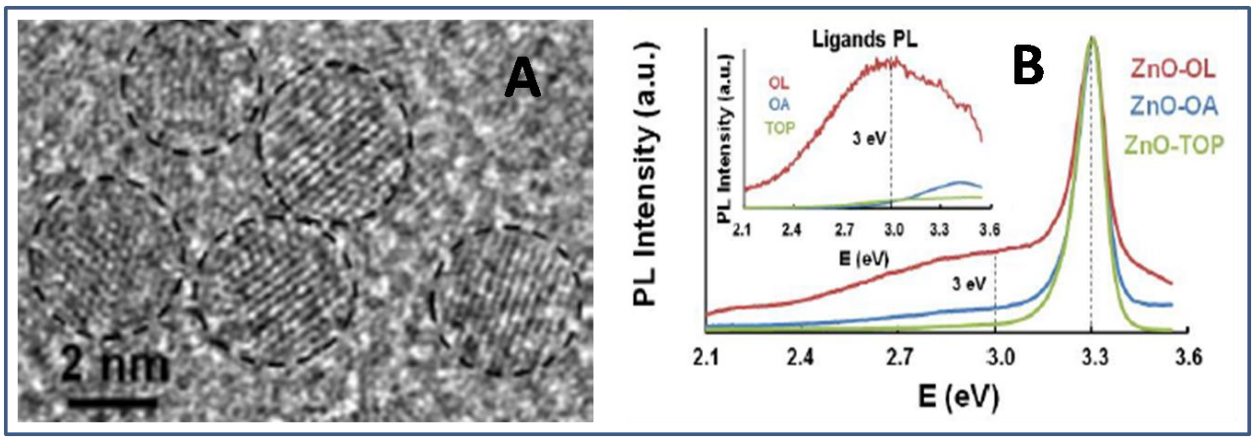

Figure II-1. HRTEM image of ZnO NCs obtained by supercritical microfluidics (A); room temperature PL spectra of ZnO NCs obtained using OL, OA and TOP (B) (adapted from [1]).

The synthesis of such ZnO NCs was developed thanks to an original experimental continuous set-up based on supercritical microfluidics [2]. Through an advanced control of the operating parameters such as temperature, pressure and residence time, this original co-flowing microfluidic process has allowed developing the chemistry and the process for the formation of these high quality ZnO NCs. However, the production rate of ZnO NCs with this microfluidic set-up remains

very low, only a few mg per hour. Moreover, such material quantity is not enough for deep physico-chemical characterizations of these interesting ZnO NCs and also for their applications. Therefore, it is a critical to produce larger quantities of high quality ZnO NCs. According to this, the scaling of the supercritical fluids process from micro- up to milliscale was necessary and was the first objective of this Ph.D. work. It is important to underline that this objective will allow proposing an efficient synthesis method coupling continuous micro- and millifluidics supercritical synthesis for development of the advanced materials.

First of all, this chapter presents the development of the experimental set-up for the increasing of the production rates of ZnO NCs (up to gram scale of ZnO NCs in ethanol/water dispersion per day) and the investigation of the influence of reactor dimensions and associated hydrodynamics on the characteristics of ZnO NCs. In a second point, a deep characterization and the morphology control of ZnO NCs are presented.

I. Experimental set-up for the synthesis of ZnO NCs through SCFs route and associated procedures

Figure II-2 shows a scheme of the experimental continuous SCFs set-up for the synthesis of ZnO NCs used in this work. The set-up includes a reactor, a furnace, two pumps and a back pressure regulator placed downstream the reactor. This latter was fabricated by inserting coaxially two tubings in one another – the external tube (total length of 1 m) placed into the furnace and an internal tube (length of 20 cm) placed inside the external tube (seen largement in Figure II-2). A typical experiment for the synthesis of ZnO NCs proceeds as follows: solution 1 (S_1) containing the precursor – zinc acetylacetonate monohydrate (10^{-2} M) and hydrogen peroxide ($2 \cdot 10^{-2}$ M, 35 wt.% H_2O_2 in water solution) in absolute ethanol is injected with the first pump into the internal capillary, corresponding to a ratio Zn/H_2O_2 = 1/2. Meanwhile, solution 2 (S_2), containing trioctylphosphine (TOP) with a concentration of $6 \cdot 10^{-2}$ M in absolute ethanol is injected with a second pump into the external capillary, with a ratio Zn/TOP = 6/1. The residence time in this continuous process has been varied in the range 10 s to 40 s.

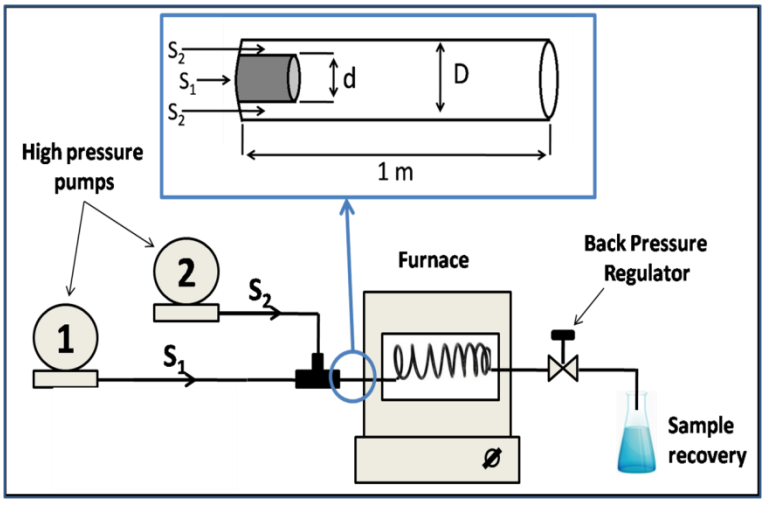

Figure II-2. Scheme of the co-flow supercritical fluids based set-up for the synthesis of ZnO NCs.

All chemicals, including zinc acetylacetonate monohydrate ($Zn(acac)_2 \cdot H_2O$, purity of 95 %), hydrogen peroxide (H_2O_2 – 35 wt.% in water), trioctylphosphine (TOP, purity of 90 %) and absolute ethanol, were purchased from Sigma-Aldrich and used as received.

In this experimental configuration, ZnO NCs formation takes place into the co-flow reactor, which is heated up to 250 ˚C by the furnace and pressurized at 25 MPa with a back pressure regulator.

The final dispersion of ZnO NCs in ethanol-water was collected downstream the back pressure regulator. ZnO NCs powders were recovered by centrifugation at 9000 rpm or by simple Büchner filtration. Recovered powders of ZnO NCs were then washed several times with absolute ethanol at room temperature and dried under air at 70 ˚C for 5 h.

II. Characterization techniques

The obtained samples were characterized by different techniques, which were used to investigate the structural, surface, thermal, optical properties and also morphology and size (Figure II-3).

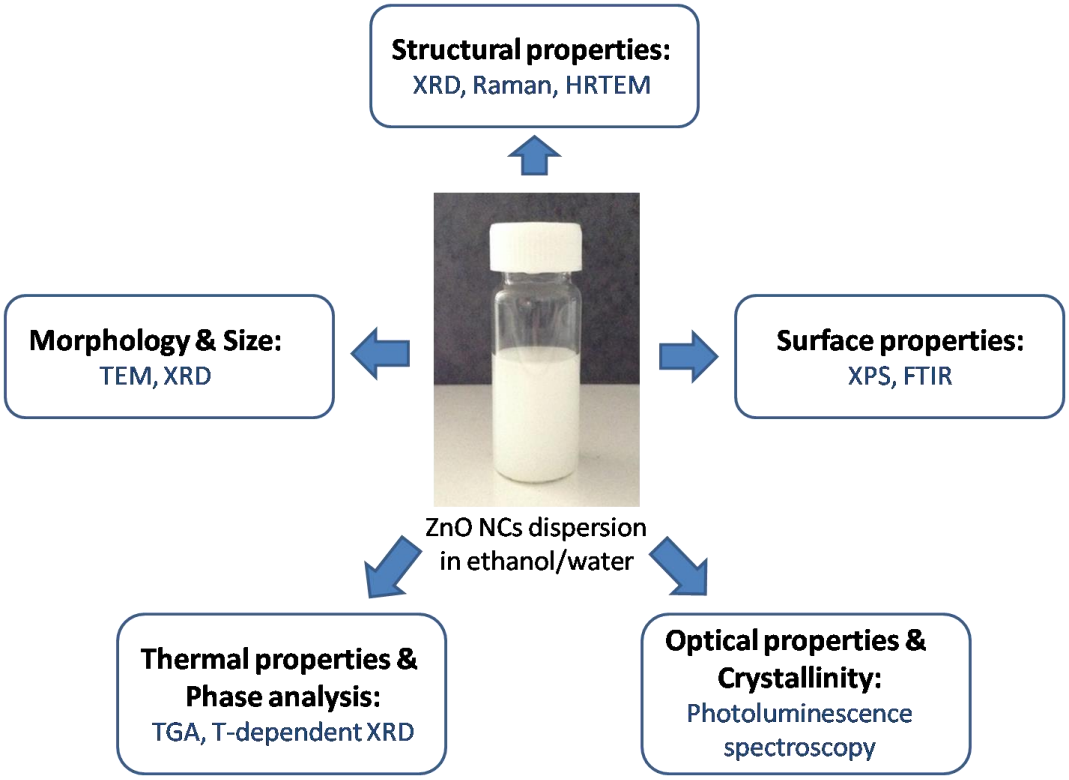

Figure II-3. Scheme representing the various techniques applied for the characterization of ZnO NCs properties.

X-ray powder diffraction and Raman spectroscopy were applied for the study of the structural properties of ZnO NCs. X-ray powder diffraction has been also applied for the NCs size estimation with the Scherrer formula. High-Resolution Transmission Electron Microscopy was used to access morphology, size, size distribution and structure of the samples. Thermogravimetry analysis was used to investigate the thermal properties and also applied for phase analysis of the samples. The detailed information concerning the surface of the samples was observed by Fourier Transform Infrared and X-ray photoelectron spectroscopies. The optical properties were investigated using

Photoluminescence spectroscopy at room and low temperature. This section will provide general information concerning characterization techniques and equipments used in this PhD work.

II-1. X-ray powder diffraction

X-ray powder diffraction measurements (XRD) were recorded with a PANaliticalX'Pert Pro powder diffractometer in the Bragg-Brentano geometry using a monochromator with $K\alpha_1$ line (λ=1.54056Å) at room temperature over the angular 2θ range 8-80 degrees with a step of 0.02 degree. The samples were prepared by depositing ZnO powder on a silicon XRD support. High-resolution X-ray diffraction measurements were collected at room temperature over the angular 2θ range 20-120 degrees with a step of 0.02 degree. Rietveld refinement was carried out using the Full Prof program for ZnO NCs to evaluate the crystal structure [3]. X-ray diffraction patterns were analyzed with the Scherrer formula for the NCs size estimation:

$$D = \frac{0.94\lambda}{\beta \cos\Theta} \qquad \text{(eq. 1)}$$

with, λ being the wavelength of the Cu k_α radiation (1.54 Å), β the full width at half maximum of the peak and Θ the Bragg's angle obtained from 2Θ value corresponding to the maximum intensity peak in XRD pattern. The calculations of the crystalline size by the Scherrer formula were not corrected by the contribution of the equipment function. The XRD characterizations as a function of temperature were performed with a powder diffractometer Philips X'Pert containing a chamber of high temperature (1800 K) and equipped with a copper anticathode K/K. The accumulation of data was performed between 8 and 80 degrees with a step of 0.02 degree and time of accumulation of 5 s. The analysis was carried out between 25 and 600 °C with an accumulation every 40 degrees. After each accumulation a pause of 30 minutes was made, allowing ensuring the temperature

stability of the chamber. The samples were prepared by depositing the powder on an aluminum XRD support. XRD measurements were performed by Eric Lebraud and Stanislav Pechev (ICMCB).

II-2. Raman spectroscopy

Raman spectra were measured using a Thermo scientific DXR micro-Raman spectrometer with a 532 nm excitation wavelength and a laser power of 10 mW at room temperature. The samples for Raman measurements were prepared by depositing a small quantity of powder on a glass plate. Raman measurements have been carried out, in particular, thanks to a collaboration with Michel Couzi (IMS, University of Bordeaux).

II-3. High-Resolution Transmission Electron Microscopy

High-Resolution Transmission Electron Microscopy (HRTEM) observations were performed using a JEOL 2200 FS equipped with a field gun emission, operating at 200 kV and with a point resolution of 0.23 nm. HRTEM was also applied for the investigation of the sample structure by the electronic diffraction. The lattice spacing of the crystallographic planes was calculated following the equation:

$$D = \frac{1}{2/d} \qquad \text{(eq. 2)}$$

with, D the measured distance and d the real lattice spacing. Samples for HRTEM measurements were prepared by dropping the NCs powder dispersion on a copper carbon grid. All high resolution measurements were done in collaboration with Sonia Buffière (PLACAMAT).

II-4.Thermogravimetry analysis

Thermogravimetry analysis (TGA) was carried out using a Pyris^{TM} 1 TGA analyzer (PerkinElmer) at a heating rate of 6 °C·min^{-1} in the temperature range of 20-600 °C under N_2 atmosphere. TGA measurements were performed by Philippe Dagault (ICMCB).

II-5. Fourier Transform Infrared Spectroscopy

Fourier Transform Infrared spectra (FTIR) were performed using a Bruker FTIR Infrared spectrometer for achieving absorption and reflection from 7500 to 4000 cm^{-1}. The sample powders (a few mg) were mixed with KBr and deposited on a steel support. FTIR measurements were realized with the help of Alexandre Fargues (ICMCB).

II-6. X-ray Photoelectron Spectroscopy

X-ray Photoelectron Spectroscopy (XPS) spectra were measured with an ESCALAB 220iXL from VG, a X-ray source TWIN Mg (1253.6 eV) and a scanning power of 150 eV. The analyzed area is a circle with a diameter of 150 μm. High resolution spectra were measured with an energy E_p of 40 eV. The samples were prepared by pressing a small amount of powder on indium foils. Spectra were exploited with the AVANTAGE software from Thermo Fisher Scientific. XPS measurements were performed in collaboration with Christine Labrugère (PLACAMAT).

II-7. Photoluminescence Spectroscopy

The emission and excitation spectra were measured with a JobinYvon SPEX fluorolog212 equipped with a double monochromator and a xenon lamp. Excitation and emission wavelengths are selected by two double monochromators of focal distance 22 cm with a Czerny-Turner configuration. A first monochromator selects the wavelength of the light coming to the sample while the emitted light from the sample is filtered by the second monochromator. The emission signal is detected and amplified by a photomultiplier Hamamatsu R928 cooled by Peltier effect. Emission spectra are systematically corrected from the spectral response of the system with the correction file taking into account the variations of the transmission of the monochromator as well as the response of the photomultiplier. Excitation spectra are corrected from the emission profile of the lamp with a system detecting the intensity of the excitation light, which is composed by Rhodamine Beta and a photomultiplier, located just after the excitation monochromator.

The low temperature PL measurements were carried out using a double chamber cryostat. The first chamber is pumped in order to reach a high vacuum (10^{-7} mPa), while a second chamber contains the sample in a stream of low temperature helium gas obtained through the vaporization of liquid helium in a capillary wrapped around a heating element, which regulates the temperature. A pumping system ensures the circulation of helium gas allowing low temperature measurements from 4.5 K to room temperature. In order to measure PL spectra from low to room temperature, the sample was put in contact with a bronze sample holder allowing temperature control between 4.5 and 300 K. A thermal probe was also linked to the sample. Samples for PL measurements were prepared by dropping the nanoparticles powder dispersion on a quartz plate. The quartz plate with a deposited powder was dried for a few hours at 50 ˚C.

III. Scaling-up continuous supercritical fluids based set up for the synthesis of UV-emitting ZnO NCs

In order to produce a larger quantity of ZnO NCs the scale up of the reactor was studied. The scale up strategy was based on the increasing of reactor channel diameter from micro- up to millifluidic dimensions in order to obtain a larger production rate of ZnO NCs keeping the same NCs characteristics. Table II-1 shows the dimension of four different reactors systems namely C_1, C_2, C_3 and C_4, which have been developed in this study allowing switching from micro- (C_1-C_3) up to millifluidic reactors (C_4). As it can be seen from Table II-1, in the case of microreactors, the production rate is very low – from 3 mg (C_1) up to 30 mg of ZnO NCs per hour (C_3), whereas the production rate in the case of C_4 millireactor can reach 100 mg/h (up to 1 g in ethanol/water dispersion per day).

Table II-1.Four dimensions of the reactor channels used for the synthesis of ZnO NCs.

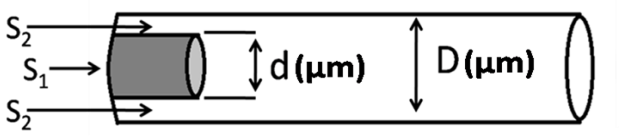

Scale	Reactor name	d (µm)	D (µm)	Average production rate (mg/h)	Residence time	Available characterization techniques
Micro-	C_1	100	250	3	10	Raman, HR TEM, PL
	C_2	100	320	5	10	Raman, HR TEM, PL
	C_3	250	750	30	10	Raman, HR TEM, PL, XRD
Milli-	C_4	750	2100	100	40	Raman, HR TEM, PL, XRD, FTIR, TGA, XPS

ZnO NCs obtained using microreactors could be characterized only by TEM, Raman and photoluminescence (PL) spectroscopy due to small quantities. However, ZnO NCs produced using

C_4 millireactor can be characterized deeply due to larger available quantity of this material. Thereby, all characterization techniques started to be available for the investigation of ZnO NCs such as X-ray powder diffraction (XRD), Fourier Transform Infrared spectroscopy (FTIR), Thermogravimetry analysis (TGA) and X-ray Photoelectron spectroscopy (Table II-1). This was very important to have the opportunity to deeply characterize these UV-emitting ZnO NCs.

As it was described before, ZnO NCs have been prepared using four reactors (C_1-C_4) in co-flowing supercritical fluids continuous set-up keeping the same operating parameters (T, P, concentrations of $Zn(acac)_2 \cdot H_2O$, TOP and H_2O_2) except residence time. The residence time for microreactors (C_1-C_3) was fixed at 10 s, while the residence time for the millireactor C_4 was increased up to 40 s to compensate the difference of heat transfer between micro- and millifluidic reactors [2]. The characterization strategy of ZnO NCs obtained with C_1-C_4 reactors was based on the structural investigation by Raman spectroscopy and further verification of the NCs nature and quality by photoluminescence spectroscopy.

It is well known that, ZnO has a hexagonal würtzite-type structure with the space group $P6_3mc$. This structure has two formula units per primitive cell where all atoms occupy C_{3v} sites. The Raman active zone-center optical phonons predicted by the group theory are $A_1+2E_2+E_1$ [4]. The phonons of A_1 and E_1 symmetry are polar phonons and also exhibit different frequencies for the transverse optical (TO) and longitudinal (LO) phonons. The nonpolar phonon modes with E_2 symmetry in würtzite-type structure of ZnO have two frequencies – $E_{2\text{-high}}$ and $E_{2\text{-low}}$ [5]. The $E_{2\text{-high}}$ mode is associated with oxygen atoms vibration and $E_{2\text{-low}}$ mode is attributed to Zn sublattice atoms vibration.

The crystal structure of materials obtained with the four co-flow C_1-C_4 reactors was investigated by Raman spectroscopy (Figure II-4). The spectra exhibit three bands in the range 411-417 cm^{-1}, 433-436 cm^{-1} and 576 cm^{-1}.

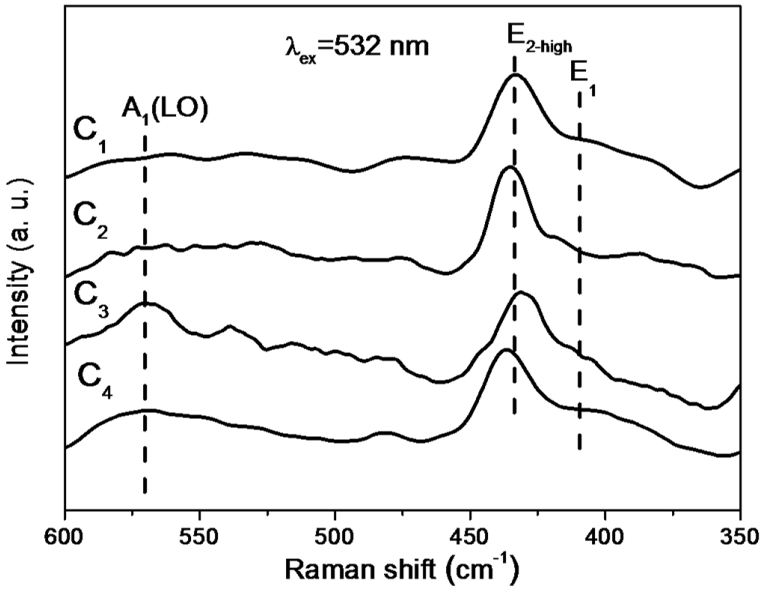

Figure II-4. Raman spectra of ZnO NCs obtained with C_1 – C_4 reactors.

Thereby, according to literature (Table II-2), the band with a maximum between 433-436 cm^{-1} can be attributed to a $E_{2\text{-high}}$ nonpolar optical mode of würtzite ZnO; this mode is active in all samples and exhibits the most intensive and narrow band.

Table II-2. Raman modes (cm^{-1}) observed in ZnO NCs obtained from C_1-C_4 reactors compared with modes observed for bulk ZnO [6-7].

Reactor	E_1	E_2(high)	A_1(LO)
Ref. [6-7]	410	437	574
C_1	411	433	-
C_2	417	435	-
C_3	414	432	576
C_4	414	436	576

The band with a maximum between 411-417 cm^{-1} can be attributed to E_1 polar mode of ZnO würtzite structure, while the band at 576 cm^{-1}, which can be attributed to A_1(LO) polar longitudinal phonon mode, is visible only in the case of the samples obtained with C_3 and C_4 type of reactors. Thereby, all observed Raman bands can be attributed to würtzite type structure of ZnO confirming that the samples obtained with C_1-C_4 co-flow reactors exhibit hexagonal würtzite structure of ZnO.

Further characterization of ZnO NCs obtained with the four C_1-C_4 co-flow reactor configurations was photoluminescence spectroscopy (Figure II-5). It is important to remind that our first objective is to strain at a gram scale of UV-emitting ZnO NCs. That is why the second characterization technique was photoluminescence spectroscopy. All spectra have a similar shape in comparison with the reference sample obtained with C_1 reactor; the spectra exhibit only one narrow emission peak centered at 377 nm in the UV region, while the defect emission in the visible region is fully absent. This UV emission is attributed to the free excitonic recombination in ZnO due to the known ZnO band gap value of 3.37 eV.

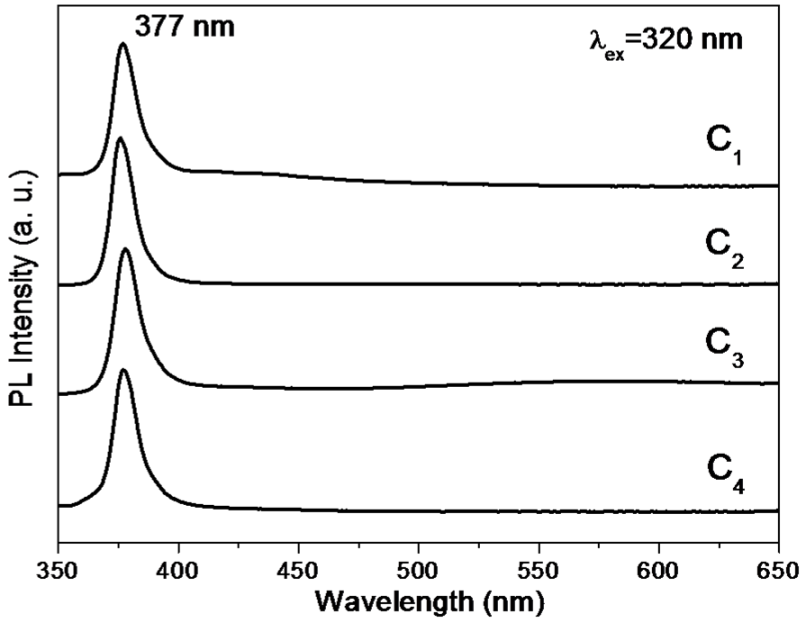

Figure II-5. Photoluminescence spectra of ZnO NCs obtained with C1-C4 reactors.

The intensive UV emission and at the same time the quenched visible emission in photoluminescence spectra show that ZnO NCs obtained with the continuous supercritical fluids based process demonstrate high crystallinity and stoichiometry.

Raman and photoluminescence spectroscopies show that ZnO NCs obtained with all C_1-C_4 co-flow reactor configurations demonstrate similar structural and optical properties independently on

reactor channel dimension i.e. ZnO NCs are crystallized in ZnO würtzite structure with UV-emitting only photoluminescence properties confirming the high quality of these NCs. Thereby, the scale up of the continuous supercritical fluids based set-up, as a first objective of this Ph.D., is successfully reached for the production of larger quantity of high quality ZnO NCs (from 3 mg/h for C_1 and up to 100 mg/h for C_4 reactor) keeping the same UV-emitting only optical properties which are very promising for optochemical applications based on UV sensing. The next step was a deep characterization of this UV-emitting ZnO NCs.

IV. Deep characterization of UV-emitting ZnO NCs

As it was shown in the previous section, the scale up of continuous supercritical fluids based set-up allows higher production of high quality ZnO NCs keeping the same optical properties. A deep characterization of structural, morphological and surface properties of ZnO NCs obtained by SCFs is now needed. In this section, the discussion concerning a deep characterization of ZnO NCs obtained with C_4 millifluidic reactor is provided.

The structural characteristics of ZnO NCs obtained with C_4reactor were obtained by high resolution XRD (Figure II-6). As it can be seen from the figure, all X-ray diffraction peaks can be attributed and indexed with ZnO würtzite structure (JCPDS card No. 01-075-0576) [8]. Rietveld refinement of this XRD pattern with satisfying indexes of agreement with the würtzite-type structure of ZnO was obtained (Bragg R-factor – 5.3, RF-factor – 3.2). The refined lattice parameters values are a=b=3.2512(1) Å, c=5.2090(2) Å and cell volume V=47.687(3) $Å^3$. ZnO NCs size was obtained by Scherrer equation from XRD pattern and equal to 8.2 nm.

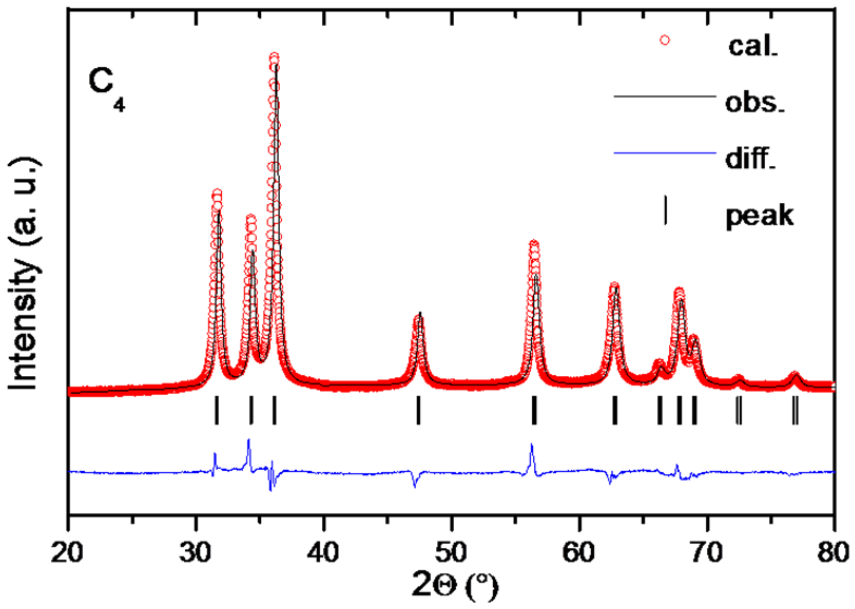

Figure II-6. Rietveld refinement of XRD pattern of ZnO NCs obtained with C_4 reactor.

The crystal structure of ZnO NCs obtained with C_4 millireactor has also been investigated by HRTEM (Figure II-7-A). The lattice spacing of the spherical ZnO nanocrystal with size around 9 nm was measured to be of 0.19 nm. Different crystallographic planes of ZnO würtzite structure such as (110), (103) and (100) were also observed using the other HRTEM micrographs. HRTEM could also confirm a high crystallinity of ZnO NCs obtained by SCFs.

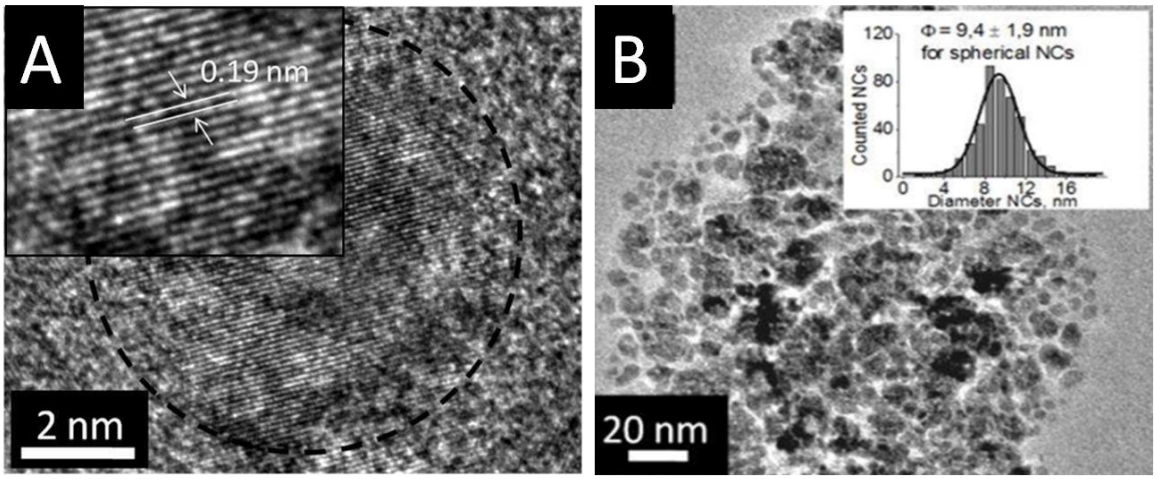

Figure II-7. HRTEM micrograph of ZnO NCs obtained with C_4 reactor: high-magnification micrograph of a ZnO nanocrystal, a zoom is in inset (A) and a survey TEM micrograph of ZnO NCs, the Gaussian size distribution is shown as inset.

TEM measurements were also carried out for the characterization of the size, size distribution and shape of ZnO NCs obtained with C_4 reactor (Figure II-7-B). ZnO NCs demonstrate somewhat spherical shape with an average NCs size equal to 9.4±1.9 nm.

As it was described before, ZnO NCs are synthesized in the presence of trioctylphosphine which was used as a stabilization agent. FTIR spectrum was measured for ZnO NCs obtained with C_4 reactor in order to investigate the surface properties of these NCs (Figure II-8).

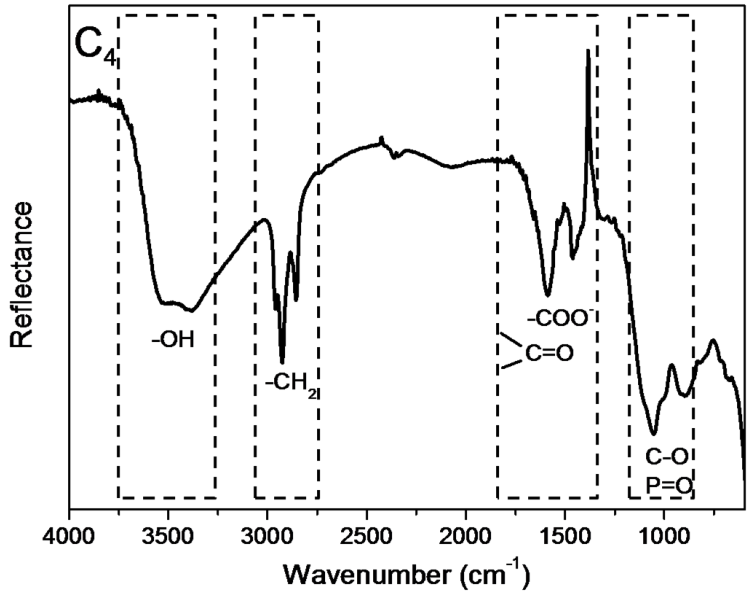

Figure II-8. FTIR spectra of ZnO NCs obtained with the C_4 reactor.

The strong absorption peak centered at 3500 cm^{-1} is attributed to the stretching vibrations of –OH groups. The absorption peaks at 2929 cm^{-1}, 2856 cm^{-1} are stretching vibrations of methylen groups ($-CH_2$) which are originated from TOP. The peaks located at 1587 cm^{-1} and 1390 cm^{-1} could be attributed to carboxylate ions (COO^-) and function which can form COO-Zn bound and acetylacetonate on the surface of ZnO NCs. The absorption peaks at 1049 cm^{-1} could be attributed to C-O and/or P=O stretching vibrations. Therefore, FTIR analysis shows that OH, acetylacetonate functions and also TOP molecules can be found at the surface of ZnO NCs.

For further surface characterization XPS measurements were performed on the sample obtained with the C_4 reactor (Figure II-9). XPS analysis is in good agreement with FTIR data confirming the presence of phosphorous functions at the surface of ZnO NCs from TOP and also trioctylphosphine oxide (TOPO), which could be formed through the oxidation of TOP by hydrogen peroxide or water during the ZnO NCs synthesis.

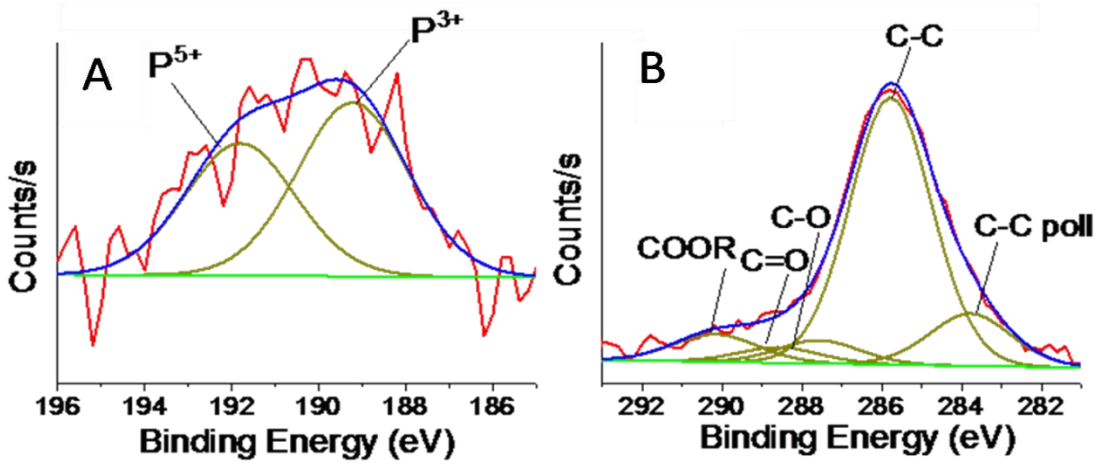

Figure II-9. P_{2s} (A) and C_{1s} (B) high resolution XPS spectra for ZnO NCs obtained with C_4 reactor.

Phosphorous atoms present in two P_{2s} states for P^{3+} and P^{5+} at the energies of 189.23 eV and 191.81 eV, respectively (Figure II-9-A). It suggests the possible bounding between TOP and/or TOPO with ZnO NCs surface. XPS spectrum also shows the presence of several contributions among COO^-, C=O and C-O bounds corresponding to acetylacetonate (Figure II-9-B). All the above mentioned XPS peaks disappeared upon Ar^+ ion etching confirming the surface location of the organic functions [1].

The quantification of these organic functions observed by FTIR and XPS on the ZnO NCs surface was determined using TGA for the sample obtained with the C_4 reactor (Figure II-10). TGA curve shows two weight loss steps of 0.8 and 5.8 %. The derivative function of this curve has two peaks with the global minima at 52 and 465 ˚C. The first peak at 52 ˚C could be attributed to the physisorbed traces of atmospheric water. The second peak at 465 ˚C of the derivative function could be attributed to the presence of chemisorbed molecules on the surface of ZnO NCs such as acetylacetonate coming from $Zn(acac)_2$ and TOP. The calculated average quantity of organic functions on the surface of ZnO NCs is about 6 wt. %.

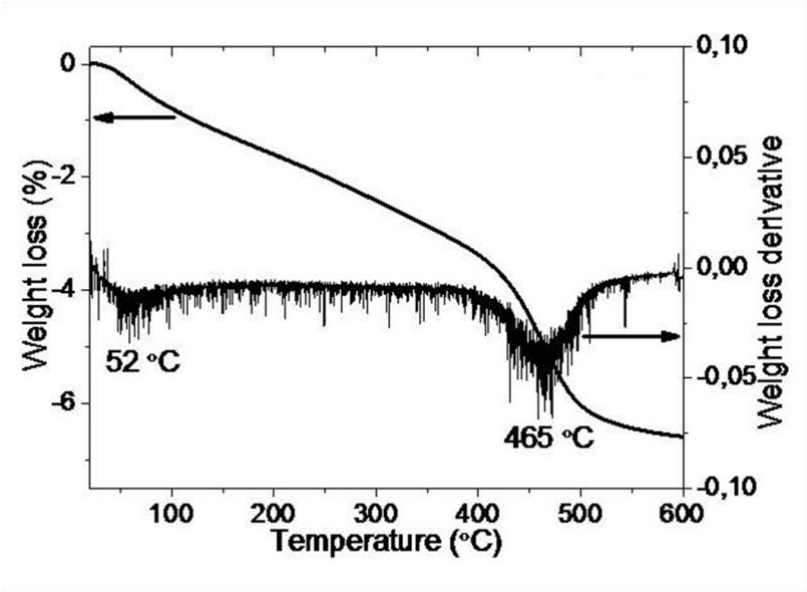

Figure II-10. TGA of ZnO NCs obtained with C_4 millireactor.

To conclude at this step, the structural, morphological and surface properties of ZnO NCs obtained with the C_4 reactor were characterized using XRD, HRTEM, FTIR, XPS and TGA techniques. It was shown that ZnO NCs are crystallized in würtzite structure with high crystallinity and stoichiometry. ZnO NCs obtained with the C_4 reactor exhibit spherical shapes with an average size equal to 9.4±1.9 nm and surrounded with about 6 wt.% of organics originated from $Zn(acac)_2 \cdot H_2O$ and TOP.

In addition, high crystalline ZnO NCs, which exhibit UV emission only in their PL spectra can be prepared by our SCFs method. Moreover, as it was demonstrated above, the scaling from micro- up to millifluidic set up allows obtaining a larger amount of ZnO NCs keeping the same physico-chemical characteristics of this material. However, one of the key parameter of the continuous supercritical fluids system is the hydrodynamics of the reactors. It is known that hydrodynamics strongly depends on parameters such as the reactor size and the ratio between the internal and external reactor diameters. The hydrodynamic regime is different in these reactors due to difference of their dimensions. On the other hand, the hydrodynamic regime could have an influence on the size and morphology of ZnO NCs. The other important parameter which could

have a strong influence on ZnO NCs size and morphology is the H_2O_2 concentration. This influence appears through the modification of NCs nucleation and growth processes depending on the H_2O_2 concentration. A discussion concerning the influence of hydrodynamics and H_2O_2 concentration on ZnO NCs size and morphology is provided in the next paragraph.

V. Morphology and size control of ZnO NCs

V-1. Hydrodynamic influence on ZnO NCs morphology

As it was shown before, ZnO NCs obtained with C_1-C_4 supercritical micro- and millifluidic continuous reactors demonstrate the same physico-chemical characteristics i.e. crystal, surface and optical properties. However, TEM measurements performed for ZnO NCs obtained with the different reactors show various morphologies (Figure II-11).

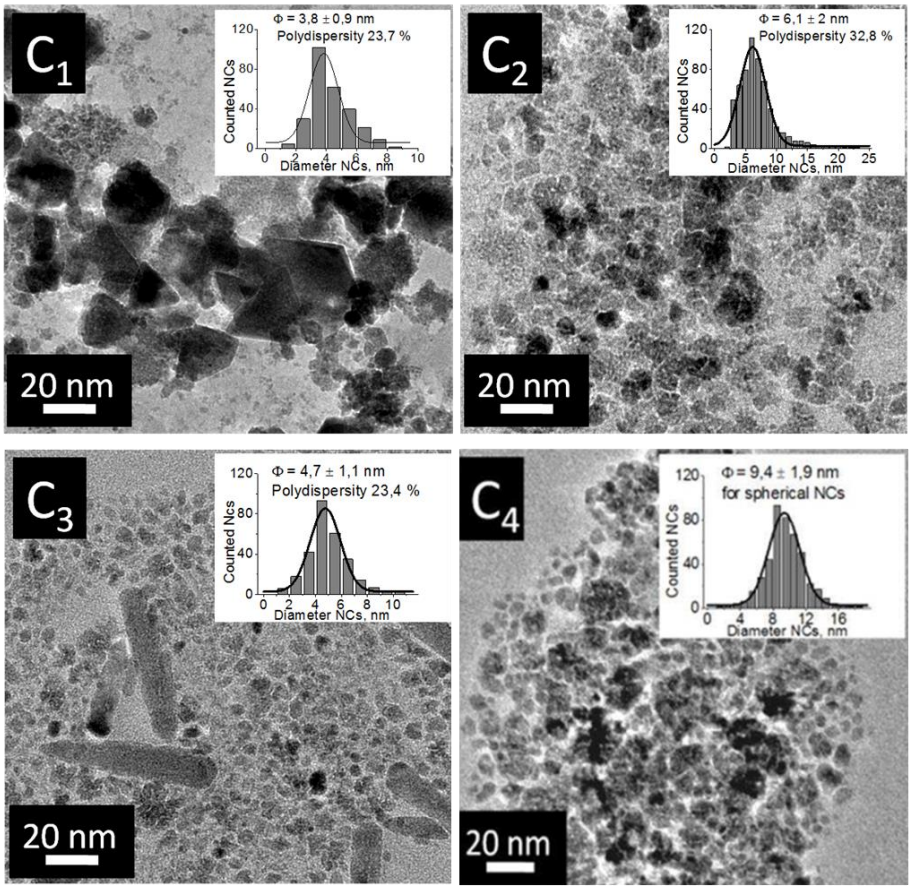

Figure II-11.TEM images of ZnO NCs obtained with the C_1-C_4 co-flow reactor configurations.

According to this figure, ZnO NCs obtained with the C_1 type of reactor exhibit two populations of ZnO NCs – spherical NCs with an average size of 3.8±0.9 nm and also ZnO triangular nanostructures. Two different morphologies of ZnO NCs were also observed with the synthesis in C_3 microreactors. In this case, spherical ZnO NCs with an average size of 4.7±1.1 nm and nanorods

are also formed. Instead of this, ZnO NCs which were prepared using C_2 microreactor and C_4 millireactor have only a unique almost spherical morphology with the average sizes of 6.1±2 nm and 9.4±1.9 nm, respectively (Figure II-11).

As it was mentioned before, ZnO NCs were obtained with C_1-C_4 reactors with the same operating parameters such as temperature, pressure, flow rates ratio and concentrations of $Zn(acac)_2 \cdot H_2O$, H_2O_2 and TOP. Thereby, the difference in ZnO NCs morphology could be explained through the influence of hydrodynamics depending on reactor channel dimension [1, 9].

The hydrodynamic regime of our supercritical continuous reactor can be characterized by two main parameters such as the fluid velocity ratio – R_H and the Reynolds number – R_e. R_H determines the shape of the internal flow (since the same fluid is injected internally and externally) and can be calculated by the following equation:

$$R_H = \frac{Q_{ext}}{Q_{\text{int}}} \frac{S_{\text{int}}}{S_{ext} - S_{\text{int}}} \qquad \text{(eq. 3)}$$

with Q_{ext}, Q_{int} *(ml/min)*are the external and internal flow rates, respectively; S_{int}, S_{ext} *(μm)* are the internal and external cross-sectional area of reactors, respectively. Two main regimes can appear depending on the R_H value: the flow focusing regime (R_H> 1) and the flow spreading regime (R_H <1) [9]. Figure II-12 illustrates the typical flow shapes which can be obtained into co-flowing reactors depending on the R_H value.

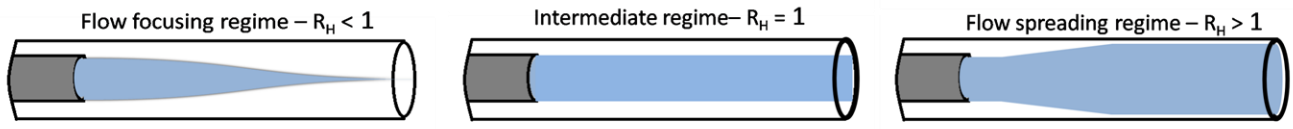

Figure II-12. Different geometries of the internal flow (blue color) in co-flow reactor system depending on R_H parameter value.

On the other hand, the hydrodynamic regime of the flows can also be characterized with the R_e number. The internal and external flows can be laminar or turbulent depending on the R_e value: if

R_e < 500 – laminar, R_e>1700 – turbulent regime, in between are transition regimes). R_e parameter could be calculated by the following equation:

$$R_e = \frac{\rho v d}{\eta} \qquad \text{(eq. 4)}$$

with *ρ (mg/ml)* – liquid density, *v (ml/min)*– flow velocity, *d (μm)* – hydrodynamic diameter, *η (Pa·s)* – viscosity.

As it was mentioned before, ZnO NCs obtained using C_1-C_4 reactors have different type of morphologies (Figures II-11). Thereby, different hydrodynamics regimes can appear due to the different reactor channel dimensions for C_1 to C_4. Table II-3 shows the hydrodynamics characteristics of flows in C_1, C_2, C_3 and C_4 such as the flow rate ratio, R_H and R_e and ZnO NCs morphologies. We can assume that the different hydrodynamics regimes and as a consequence various geometries of the flows could change the concentrations of TOP in the vicinity of the growing NCs resulting in different morphologies of ZnO NCs. In the case of C_1 and C_3 reactors where R_H (C_1) and R_e (C_3) are different in comparison with C_2 and C_4, two kinds of ZnO NCs morphologies are observed (Figure II-11). Non spherical morphology could be explained by the presence of an important TOP concentration in the vicinity of the growing NCs.

Table II-3.Hydrodynamics parameters of the C_1 – C_4 experimental reactors.

Scale	Reactor	Flow rate ratio	R_H	R_e	ZnO NCs morphology
Micro	C_1	2.75	1.22	45	Spherical, triangles
	C_2	2.74	0.44	57	Spherical
	C_3	2.78	0.40	132	Spherical, nanorods
Milli	C_4	2.78	0.85	32	Spherical

The higher TOP concentration on the co-flow contact point in interaction with the ZnO NCs growth process in the case of C_1 and C_3 conducts to the formation of triangles and nanorods,

respectively, while for C_2 and C_4 reactors a smaller TOP concentration seems to allow the separation of the nucleation and growth from the functionalization step to obtain only spherical ZnO NCs.

To confirm the hypothesis that ZnO rods and triangles are formed due to the interaction of TOP with ZnO NCs during their growth a new experiment has been carried out. This experiment was performed using the same operating parameters for ZnO NCs synthesis as it was shown previously (for C_4 reactor), but in this case TOP was injected internally (Figure II-13-A) in order to increase TOP concentration in the internal flow containing the precursor.

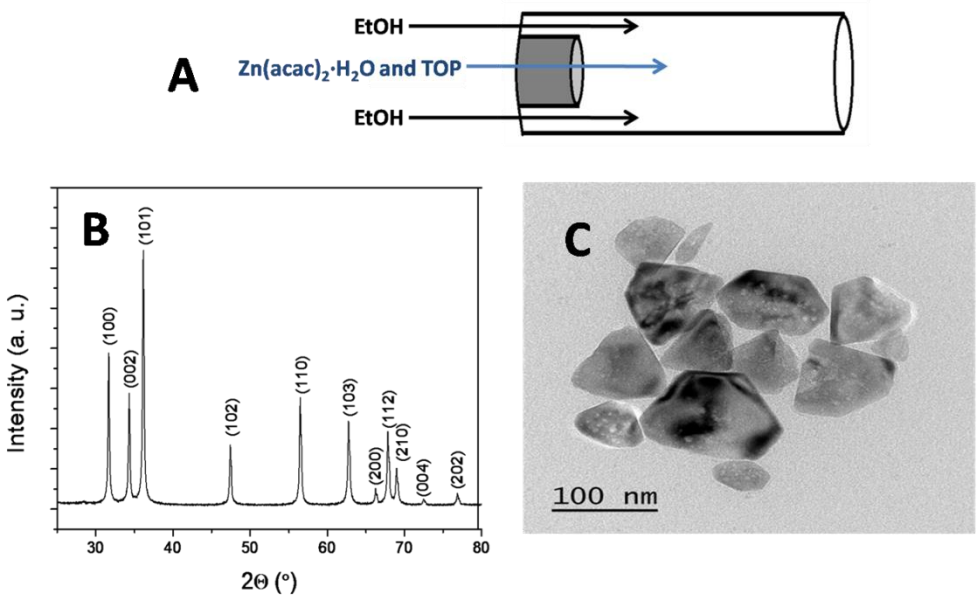

Figure II-13. Scheme of ZnO NCs synthesis with internal injection of TOP (A), XRD (B) and TEM (C) of ZnO NCs obtained with an internal injection of TOP.

Figure II-13-B shows XRD pattern of ZnO NCs obtained in this experiment. All peaks on this pattern can be attributed and indexed to the hexagonal phase of ZnO with würtzite structure. No peaks from other phase of ZnO or impurities are observed. The calculated ZnO NCs size is equal to 38.5 nm (from the Scherrer equation). Figure II-13-C illustrates TEM micrograph of ZnO NCs obtained in this experiment. In this case, ZnO NCs exhibit triangular and hexagonal shapes with

big size up to 100 nm instead of small spherical (9.4 nm) ZnO NCs obtained with the external injection of TOP (Figure II-11-C_4).

Many reports have shown that the morphology of ZnO nanostructures can be controlled by the addition of a surfactant during the synthesis [11-14]; this is in agreement with our observation in this study with the formation of different shapes of ZnO NCs such as triangles, hexagons and rods. It should be noted that, these shapes are characteristic of hexagonal structure of ZnO phase. This experiment shows that ZnO NCs morphology can be controlled by changing TOP ligands concentrations through the process hydrodynamics. Another key parameter of our process is the concentration of H_2O_2, H_2O_2 being the "initiator" of the precursor transformation.

V-2. Hydrogen peroxide concentration effect on ZnO NCs size and morphology

The evolution of size and morphology of ZnO NCs has been investigated as a function of H_2O_2 concentration. For that, ZnO NCs samples namely H_1, H_2, H_3 and H_4 were prepared with $[Zn^{2+}]/[H_2O_2]$ ratios equal to 1/0.5, 1/1, 1/2 and 1/3, respectively, without using TOP. All the other operating parameters such as residence time (40 s), temperature (250 ˚C), and pressure (25 MPa) were kept constant using the C_4 reactor.

Figure II-14 shows the evolution of TEM micrographs of ZnO NCs nanocrystals obtained as a function of H_2O_2 concentration. At the lowest H_2O_2 concentration corresponding to $[Zn^{2+}]/[H_2O_2]$ ratio of 1/0.5 and 1/1 (Figure II-14-A, B and C, D), ZnO NCs exhibit not well uniformed morphology consisting of triangles, hexagons and also spherical shaped NCs. However, ZnO NCs morphology is quite different at the highest H_2O_2 concentration, than in all previous cases, these NCs are formed in a spherical shape (Figure II-14-E, F and G, K).At the $[Zn^{2+}]/[H_2O_2]$ ratio of 1/3 which corresponds to the highest H_2O_2 concentration, ZnO NCs demonstrate a spherical morphology with a very low NCs size, while at the $[Zn^{2+}]/[H_2O_2]$ ratio of 1/2 NCs are still more or less spherical but exhibit a bigger size.

The crystal structure and an average size of ZnO NCs obtained as a function of H_2O_2 concentration were investigated by XRD (Figure II-15). XRD pattern of ZnO NCs synthesized at higher H_2O_2 concentration ($[Zn^{2+}]/[H_2O_2]$=1/3) is unavailable because it is impossible to obtained ZnO NCs powder by Büchner filtration of the dispersed NCs in ethanol/water due to their very small size. ZnO NCs samples obtained depending on H_2O_2 concentrations demonstrate hexagonal würtzite type structure. The differences in size have also been confirmed by Scherrer equation. The calculated NCs sizes are 35.5 nm, 37.6 nm and 12.9 nm for H_1, H_2 and H_3 samples, respectively. The sizes of H_1 and H_2 ZnO NCs samples are similar, while H_3 ZnO NCs sample demonstrates

decreasing in NCs size and, as it can be seen from TEM (Figure II-14-G, K), NCs size decreasing further with increasing H_2O_2 concentration.

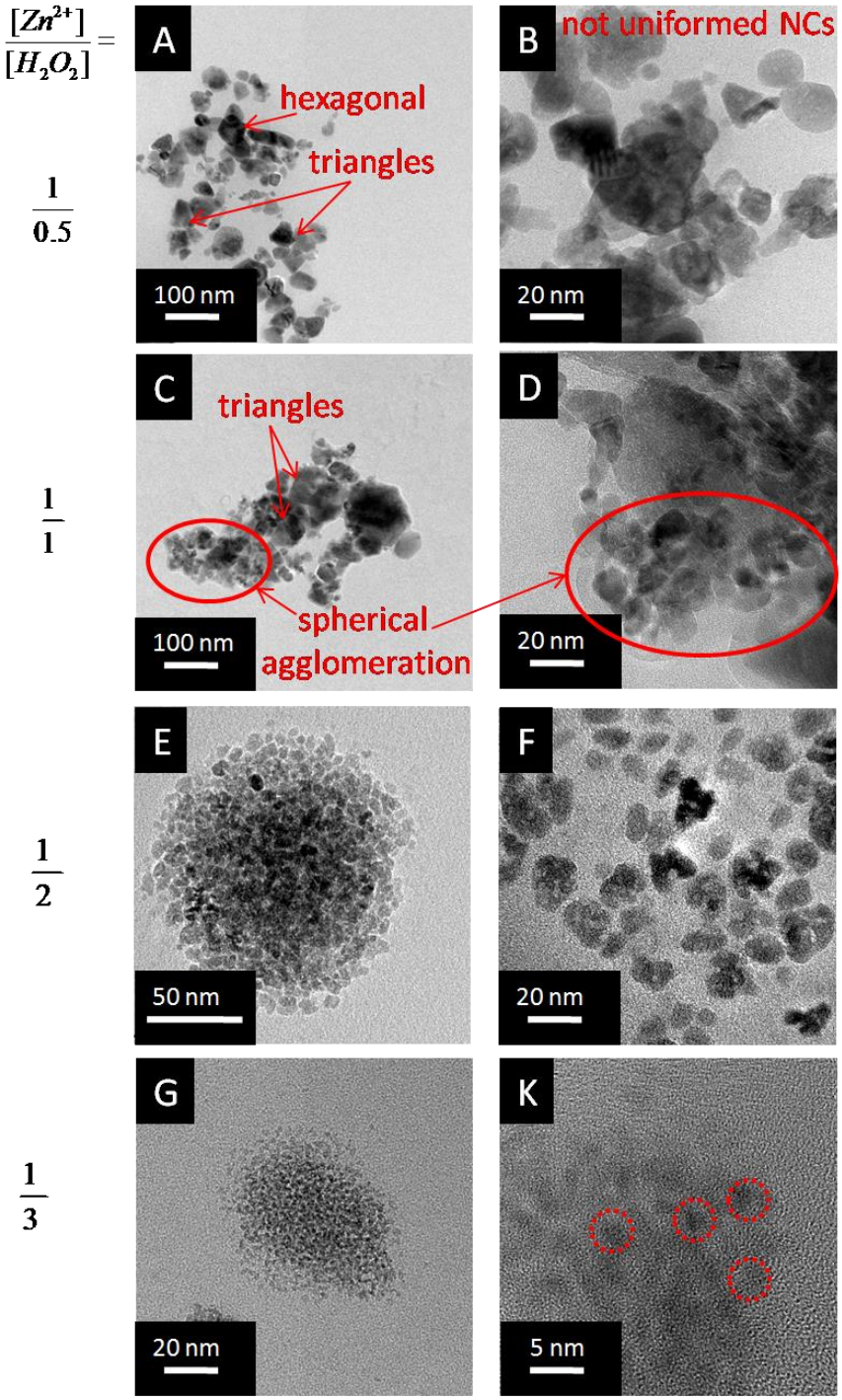

Figure II-14. TEM images with different magnifications of ZnO NCs obtained various $[Zn^{2+}]$ /$[H_2O_2]$ ratios – 1/0.5 (A, B), 1/1 (C, D), 1/2 (E/F) and 1/3 (G, K).

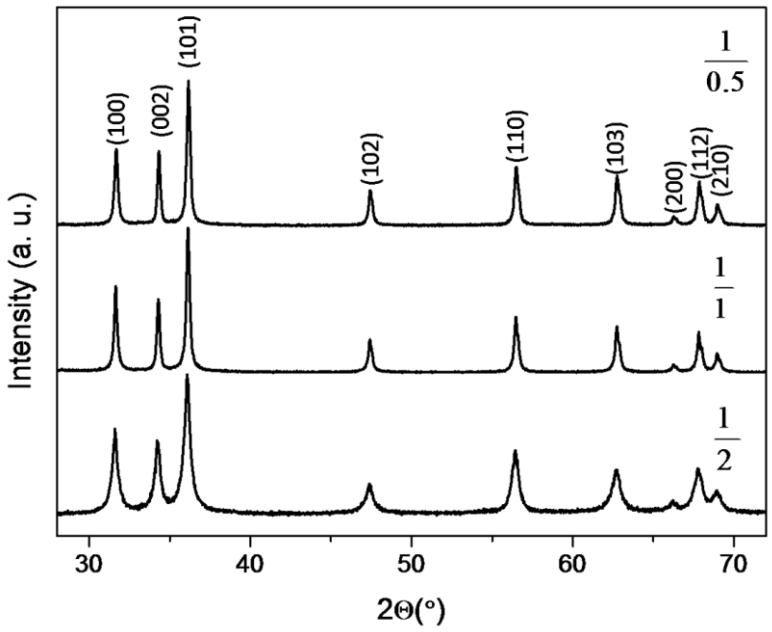

Figure II-15. XRD patterns of ZnO NCs obtained using different H_2O_2 concentrations (A) and ZnO NCs size dependence on H_2O_2 concentration (B).

Further investigation is needed to put in evidence the influence of particle morphologies on the XRD pattern (relative intensities between XRD peaks could be modified depending on morphology). As it can be seen from TEM and XRD investigations, H_2O_2 concentration has a significant influence on ZnO NCs size and morphology. At the highest H_2O_2 concentration ZnO NCs exhibit spherical morphology and very small size of few nanometers for H_4, while with decreasing H_2O_2 concentration the average size of ZnO NCs is increasing up to 35.5 and 37.6 nm for H_1 and H_2 samples, respectively.

These results can be explained with the theory proposed by LaMer and Dignae [15-16]. Figure II-16 presents a LaMer diagram which could be divided into three parts: the first part corresponds to the increase of in the monomer concentration (C) until the nucleation period (prenucleation stage), a second pert presents the increase of the monomer concentration up to the maximum supersaturation (C_{max}^{nu}) and the subsequent decrease to the growth stage (C_{min}^{nu}), and the third part indicates the concentration decrease of the monomers up to the solubility level (C_s) corresponding to the growth process. In our experiments the nucleation and growth of ZnO NCs occur by the

decomposition of $Zn(acac)_2 \cdot H_2O$ in the presence of H_2O_2. Obviously, ZnO NCs nucleation and growth processes are controlled by H_2O_2.

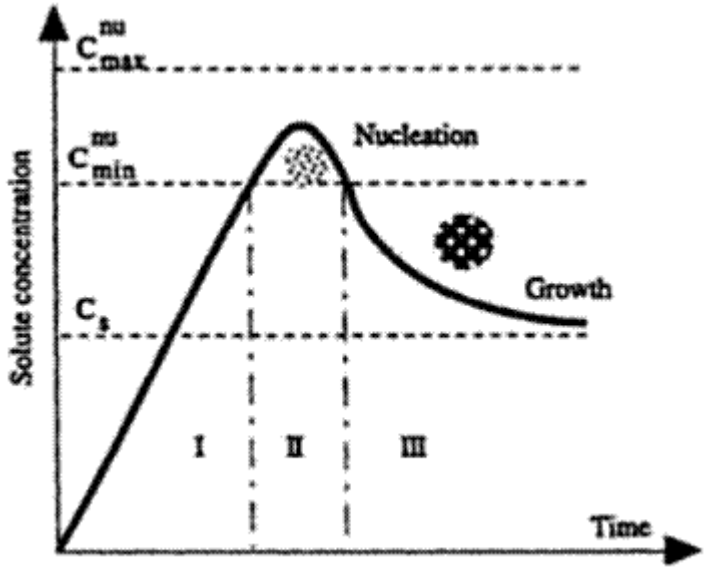

Figure II-16. LaMer diagram for the nucleation and growth processes.

According to LaMer diagram, the nucleation stage is limited to a short period of time, and the growth process is induced by a second stage where the surface of larger particles plays as a precipitant. The nucleation of NCs starts when the supersaturation of solute overcomes the energy barrier required for the formation of NCs. According to this, in the case of H_4 experiment at highest H_2O_2 concentration the nucleation of ZnO NCs occurs very fast. This process consumes all precursor stopping the reaction at this stage resulting the formation of very small spherical NCs. At H_3 experiment, the nucleation of ZnO NCs goes also fast but due to lower H_2O_2 concentration there are still some remaining precursor which participates to the growth forming more or less spherical NCs with size of 12.9 nm. In the case of H_1 and H_2 experiments the growth stage exceeds the nucleation due to low H_2O_2 concentration. In these cases, the excess of the precursor is invited to the growth of NCs nuclei which act as growth sites.

ZnO NCs size and morphology could be controlled by a two ways: (i) the hydrodynamic regimes which change TOP concentration in the vicinity of the growing ZnO NCs allowing to obtain spherical, rods and triangular morphology of NCs and (ii) H_2O_2 concentration which allows to control ZnO NCs morphology and size due to the difference in nucleation and growth processes from small spherical to big triangular and hexagonal NCs.

Conclusion:

The scaling from micro- up to millireactor dimensions of our continuous supercritical fluids based set up for the synthesis of ZnO NCs has been successfully provided. ZnO NCs obtained with all reactors exhibit UV emission only in their room temperature PL spectra. A deep characterization of ZnO NCs properties has been focused on NCs obtained with millireactor (C_4) due to a larger quantity of powder available thanks to the bigger reactor dimension. XRD, HRTEM measurements and Rietveld refinement demonstrate that ZnO NCs are crystallized in würtzite structure. The surface properties of ZnO NCs have been investigated using FTIR and XPS spectroscopy. ZnO NCs are surrounded by the organics such as –OH, -CH_2, COO-, C-O, C=O and P=O which are originated from TOP and the traces of acetylacetonate from the precursor. The quantification of these organics has been provided by TGA. It was found that the average quantity of organics on the surface of ZnO NCs is about 6 wt.%.

ZnO NCs exhibit different morphologies depending on reactor channel dimensions keeping the same optical properties. The spherical ZnO NCs were observed in the case of C_2 and C_4 reactors, while two populations of spherical and sticks (C_1) and spherical and triangular ZnO NCs (C_2) are observed. Such behavior was explained by the influence of TOP interaction with ZnO NCs in growth. The effect of H_2O_2 concentration on ZnO NCs morphology was also studied. It was observed that very small and highly uniform spherical ZnO NCs are formed with high H_2O_2 concentration, while ZnO NCs morphology starts to be not so uniform and contains some populations of triangular and hexagonal ZnO NCs with decreasing of H_2O_2 concentration. This morphology behavior could be explained LaMer diagram. ZnO NCs size and morphology in our supercritical fluids method can be controlled by two ways: the hydrodynamic regime and the H_2O_2 concentration.

Finally, this chapter demonstrates the scale up of the reactors in our supercritical fluids based method for the production of larger quantity of UV emitting only ZnO NCs, a deep characterization of these NCs, and the morphology control. However, as it is known from the literature, ZnO nanostructures usually demonstrates two types of PL emission in UV and visible range of the spectra due to the large surface area. The absence of the visible emission in ZnO NCs obtained with our supercritical fluids method is quite surprising. However, this phenomenon could be explained through the understanding of ZnO NCs formation mechanism in supercritical fluids. The discussions concerning the formation mechanism is provided in the next chapter of this Ph.D.

References:

1. Y. Roig et al. Angew. Chem., Int. Ed., 2011, 50, 12071.
2. Y. Roig, Ph.D. Thesis, University of Bordeaux 1, 2012.
3. J. Rodriguez-Carvajal, Phys. B (Amsterdam), 1993, 192, 55.
4. C. A. Anguello, D. L. Rousseau, S. P.S. Porto, Phys. Rev., 1969, 181, 1351.
5. M. Rajalakshmi et al. J. Appl. Phys., 2000, 87, 2445.
6. K. Alim et al. J. Appl. Phys., 2005, 97, 124313.
7. N. Ashkenov et al. J. Appl. Phys., 2003, 93, 126.
8. Joint Committee on Powder Diffraction Standards (JCPDS). Powder Diffraction File, Card No. 01-075-0576, Swarthmore, PA.
9. S. Marre et al. J. Supercrit. Fluids, 2012, 66, 251.
10. B. D. Cullity, Elements of X-Ray Diffraction, Addision-Wesley, Reading, Mass, USA, 3rd edition, 1967.
11. O. Pascu et al. Nanoscale, 2013, 5, 12425.
12. S. G. Kwon et al. Account Chem. Res., 2008, 41, 1696.
13. R. Sui et al. Chem. Rev., 2012, 122, 3057.
14. J. Y. Kim et al. Langmuir, 2008, 24, 4316.
15. D. Duft et al. Atmos. Chem. Phys., 2004, 4, 1997.
16. G. Gao, Nanostructures & Nanomaterials synthesis, properties & applications, Imperical College Press, London, UK, 2004.

Chapter III

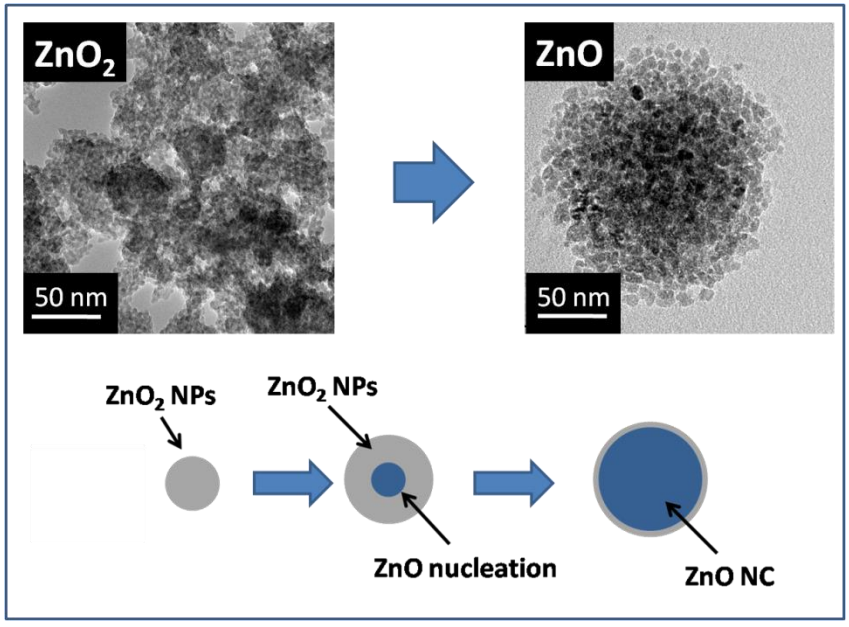

Introduction

As previously mentioned in Chapter II, highly crystalline ZnO NCs can be obtained via our continuous supercritical fluids (SCFs) approach. This material demonstrates unique optical properties i.e. a strong UV emission peak while the emission in the visible region of the spectra is totally absent. Such PL properties are usually observed for high quality ZnO single crystals characterized by high crystallinity and low crystal defects. The absence of visible emission in the ZnO NCs obtained with our SCFs approach is quite surprising regarding the literature available on PL properties of ZnO NCs generally characterized with mainly a visible emission associated to surface defects. The understanding of this behavior could be obtained through the investigation of ZnO NCs formation mechanism.

In this context, the main objective of this chapter is to investigate ZnO NCs formation mechanism in our continuous supercritical fluids based process. For this, a key process parameter, the residence time, was studied keeping constant the other parameters. The samples obtained with different residence times were deeply characterized using XRD, Raman, TEM, TGA and XPS techniques.

I. Influence of residence time on the ZnO NCs characteristics

In order to understand the unusual optical properties of the obtained NCs and investigate the ZnO NCs formation mechanism, the experiments were focused on the influence of residence time. ZnO NCs have been obtained by the same procedure as the one described in Chapter II. Four samples have been synthesized for four different residence times – 6 s, 10 s, 30 s and 40 s. The other operating parameters for the synthesis of ZnO NCs such as temperature (250 ˚C), pressure (25 MPa), concentrations of Zn precursor ($[Zn(acac)_2 \cdot H_2O] = 10^{-2}$ M) and oxidant ($[H_2O_2] = 2 \cdot 10^{-2}$ M), flow rates configuration were kept constant. All samples have been prepared with the millifluidic continuous reactor (C_4) in order to produce enough quantity of ZnO NCs powder for a deep characterization. The samples produced with different residence time were characterized by a number of methods - XRD, Raman, HRTEM, TGA, *In situ* high temperature XRD, FTIR and XPS.

The evolution of X-ray diffraction patterns with residence time (6 s, 10 s, 30 s and 40 s) is shown in Figure III-1.The phase obtained at low residence times (6 s and 10 s) is different of the one formed for the longest residence times (30 s and 40 s). X-ray diffraction patterns measured for the samples obtained at longer residence times (30 s and 40 s) exhibit pure ZnO phase with the hexagonal würtzite-type structure. For lower residence times (6 s and 10 s) all diffraction peaks can be indexed with the cubic zinc peroxide phase - ZnO_2 (JCPDS card No. 13-0311) [1-5]. Figure III-2 presents the ZnO_2 unit cell; cubic ZnO_2 phase (space group Pa-3, a=4.871 Å) can be described as a body face centered occupied by the O_2^{2-} anions, Zn^{2+} cations occupying the octahedral sites of the array [1].

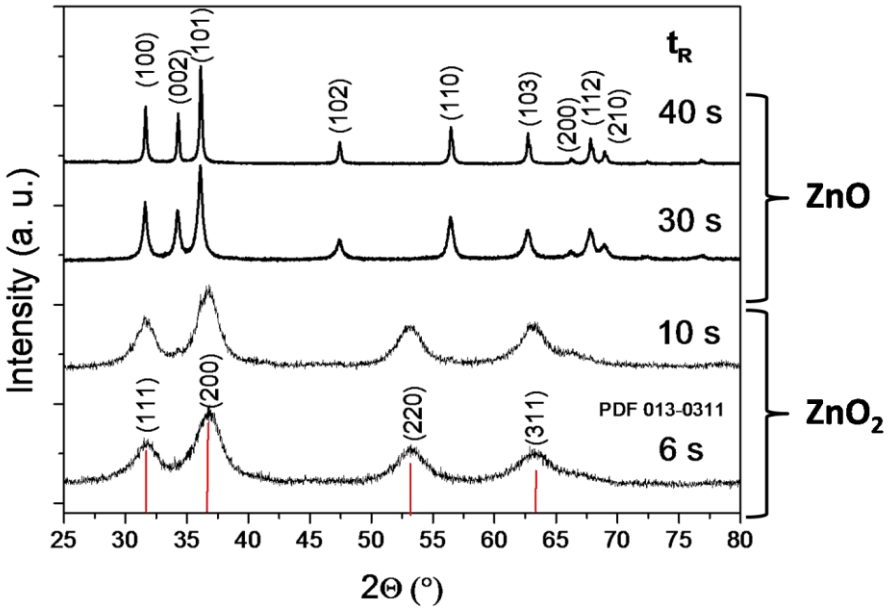

Figure III-1. Evolution of XRD diffraction patterns of Zn based materials as a function of residence time.

It is very important to mention that in ZnO_2 cubic lattices, the distance between two oxygen atoms in the O_2^{2-} pair is equal to 1.47 Å and shorter that one of 2.11 Å between oxygen and zinc ions in ZnO [2].

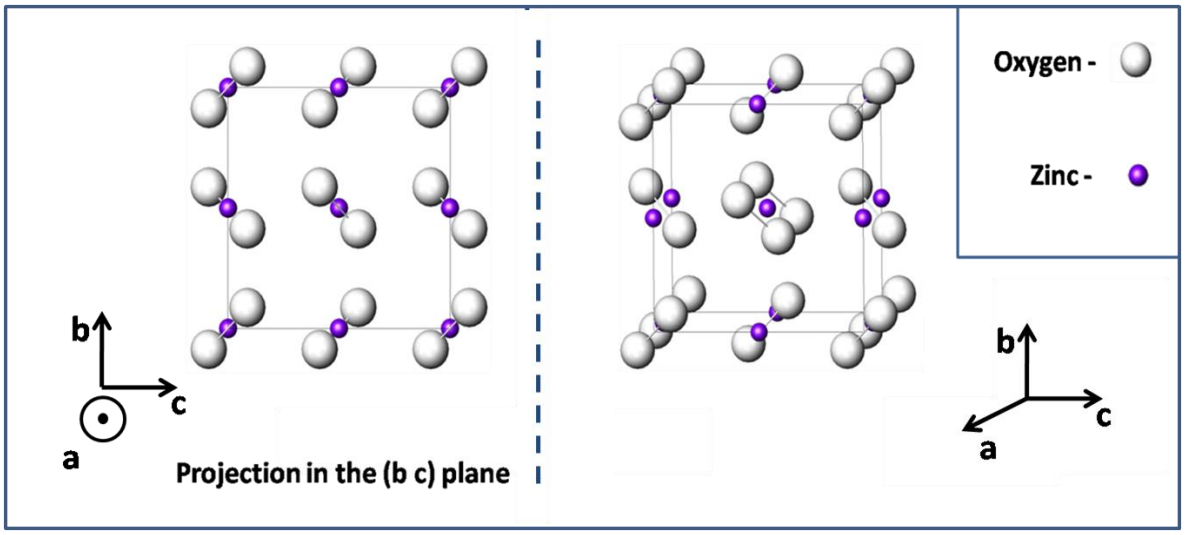

Figure III-2. Illustration of ZnO_2 cubic structure.

XRD data demonstrates that the residence time has a strong influence on ZnO NCs formation process. XRD measurements show that the samples obtained at higher residence time (30 s and 40

s) are ZnO NCs with a würtzite type structure, while the samples obtained at lower residence time (6 s and 10 s) exhibit a ZnO_2 cubic phase structure.

For further investigation of the structural properties of the samples synthesized at different residence times Raman spectra were measured (Figure III-3).

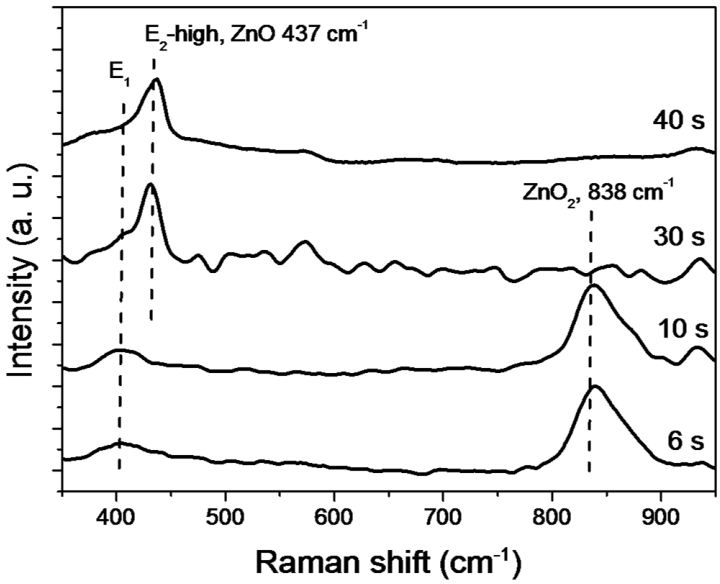

Figure III-3. Raman spectra of the samples obtained at different residence times.

Raman spectra for the samples synthesized at 30 s and 40 s residence time display two obvious Raman bands at 415 cm^{-1} and 437 cm^{-1} corresponding to E_1 polar and E_2-high nonpolar optical Raman mode of ZnO würtzite structure [6]. However, the spectra of the samples obtained at lower residence times are different. Both of these spectra exhibit intensive and broad band located at 838 cm^{-1}. This Raman shift has been observed earlier in ZnO_2 nanoparticles [7-12]. Uekawa et al. [10] have attributed Raman shift at 838 cm^{-1} to the stretching vibrations of O-O bond of the peroxo ion (O_2^{2-}). However, Raman spectra of the samples obtained at 6 s and 10 s residence times present also a broad and small intensive band between 395 and 419 cm^{-1}, which could be attributed to the E_1 polar mode of ZnO würtzite structure. The Raman analysis is in good agreement with XRD data. However, in the case of the samples synthesized at 6 s and 10 s residence time, no ZnO

characteristic XRD peaks were observed due to a lower sensitivity of XRD in comparison with Raman spectroscopy. This result could show that ZnO_2 samples obtained at 6 s and 10 s residence time contains also ZnO phase, at a concentration which could be less than 5 wt.% corresponding to XRD sensitivity.

According to XRD and Raman measurements, ZnO würtzite phase is mainly obtained in experiments with higher (30 s and 40 s) residence times, while a ZnO_2 cubic phase is observed for the lower (6 s and 10 s) residence times. These experimental results allow assuming that ZnO NCs could be formed through the intermediate ZnO_2 phase formed by $Zn(acac)_2 \cdot H_2O$ transformation in the presence of H_2O_2 in supercritical ethanol/water mixture. Moreover, it is known that ZnO_2 is a compound with a quite low decomposition temperature equal to 200 ˚C [13]. Thereby, ZnO_2 intermediate NCs could be thermally decomposed to ZnO in the supercritical reactor used in this work (250 ˚C, 25 MPa).

In order to verify the hypothesis that ZnO_2could be an intermediate phase in ZnO NCs synthesis with our supercritical approach XRD measurements as a function of temperature have been performed for the material prepared with a residence time of 6 s (Figure III-4).

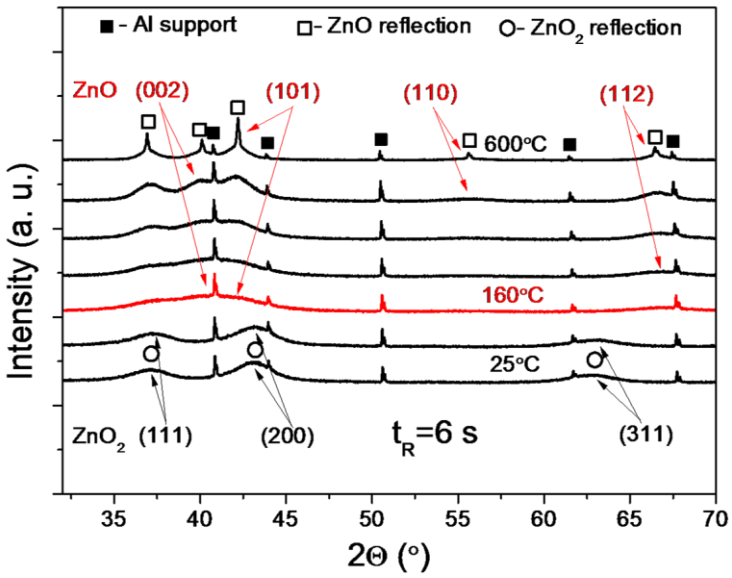

Figure III-4. XRD measurements as a function of temperature of the powder obtained with a residence time of 6 s.

As it can be seen from Figure III-4, XRD patterns of cubic ZnO_2 nanoparticles are stable below 160 ˚C; no phase transition occurs in the temperature range between 50 and 160 ˚C. However, above 160 ˚C - (002), (001) and (112) reflections from ZnO würtzite structure are appearing, while (111), (200) and (311) reflections of ZnO_2 cubic phase are disappearing. ZnO würtzite phase is stable up to 600 ˚C, and remains after cooling back to room temperature. Thus, XRD measurements as a function of temperature confirm the formation of ZnO_2 phase as an intermediate phase for the synthesis of high crystalline ZnO NCs in our supercritical fluids based method.

A number of studies from the literature show that the decomposition temperature of ZnO_2 depends on the ZnO_2 nanoparticles size. That is why the investigation of the evolution of size and morphology of the nanoparticles as a function of residence time was performed by TEM measurements before TGA. Figure III-5 shows typical TEM micrographs of ZnO_2 and ZnO samples obtained with 6, 10, 30 and 40 s residence times. All samples are constituted of nanoparticles with a more or less spherical morphology; there is a significant evolution of nanoparticles size as a function of residence time.

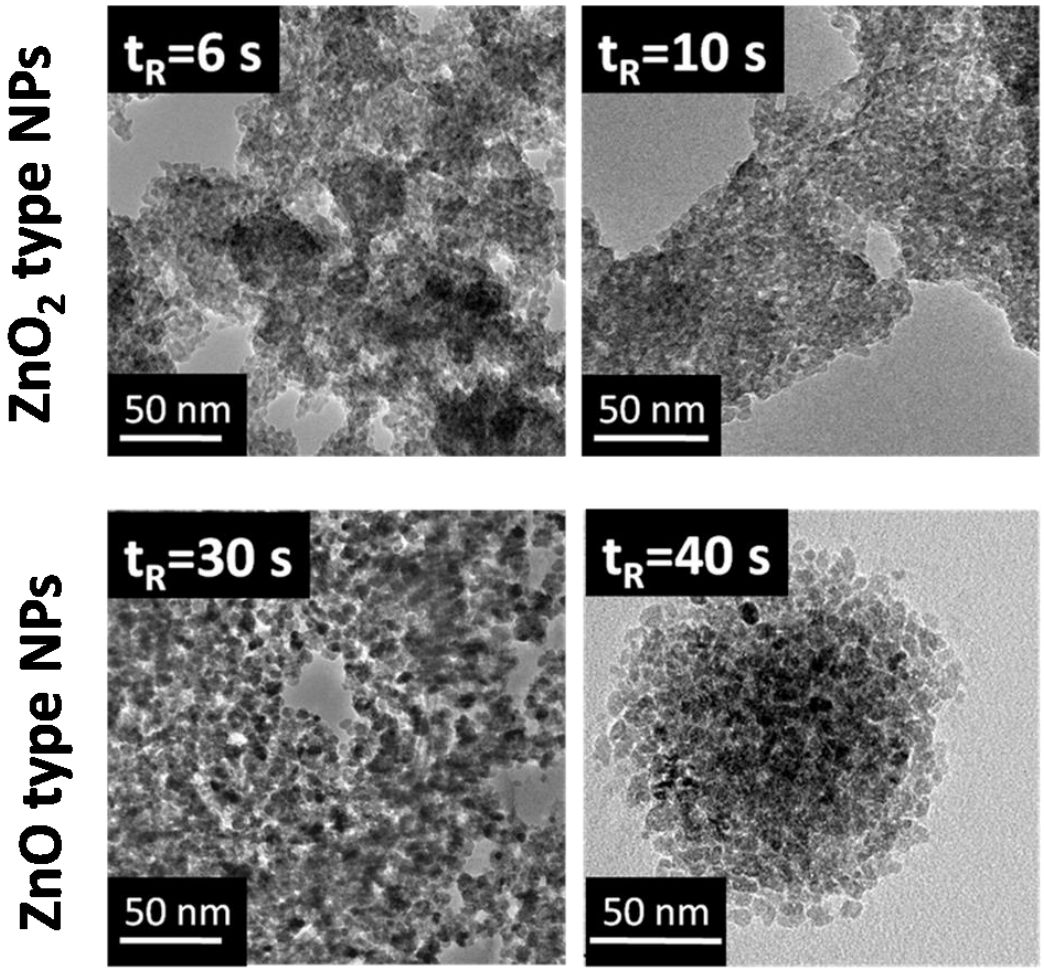

Figure III-5. TEM micrographs of the samples obtained at different residence time (6 – 40 s).

HRTEM measurements were performed to determine size and size distribution of Zn based materials as a function of residence time. Figure III-6 shows HRTEM micrographs and size distribution diagrams for about 100 nanoparticles with a Gaussian fit of ZnO_2 type nanoparticles obtained with 6 s and 10 s residence time. The size of ZnO_2 nanoparticles formed at 6 s residence time is 3.4±0.6 nm, while the size of ZnO_2 nanoparticles obtained with 10 s residence time is bigger and equal to 4.6±0.8 nm. There is an increase of ZnO_2 NPs size as a function of residence time. ZnO NCs have also a more or less spherical morphology. The size of ZnO NCs in the case of 30 s residence time is 12.8±3.5 nm and in the case of 40 s residence time is 12.9±3 nm (Figure III-7).

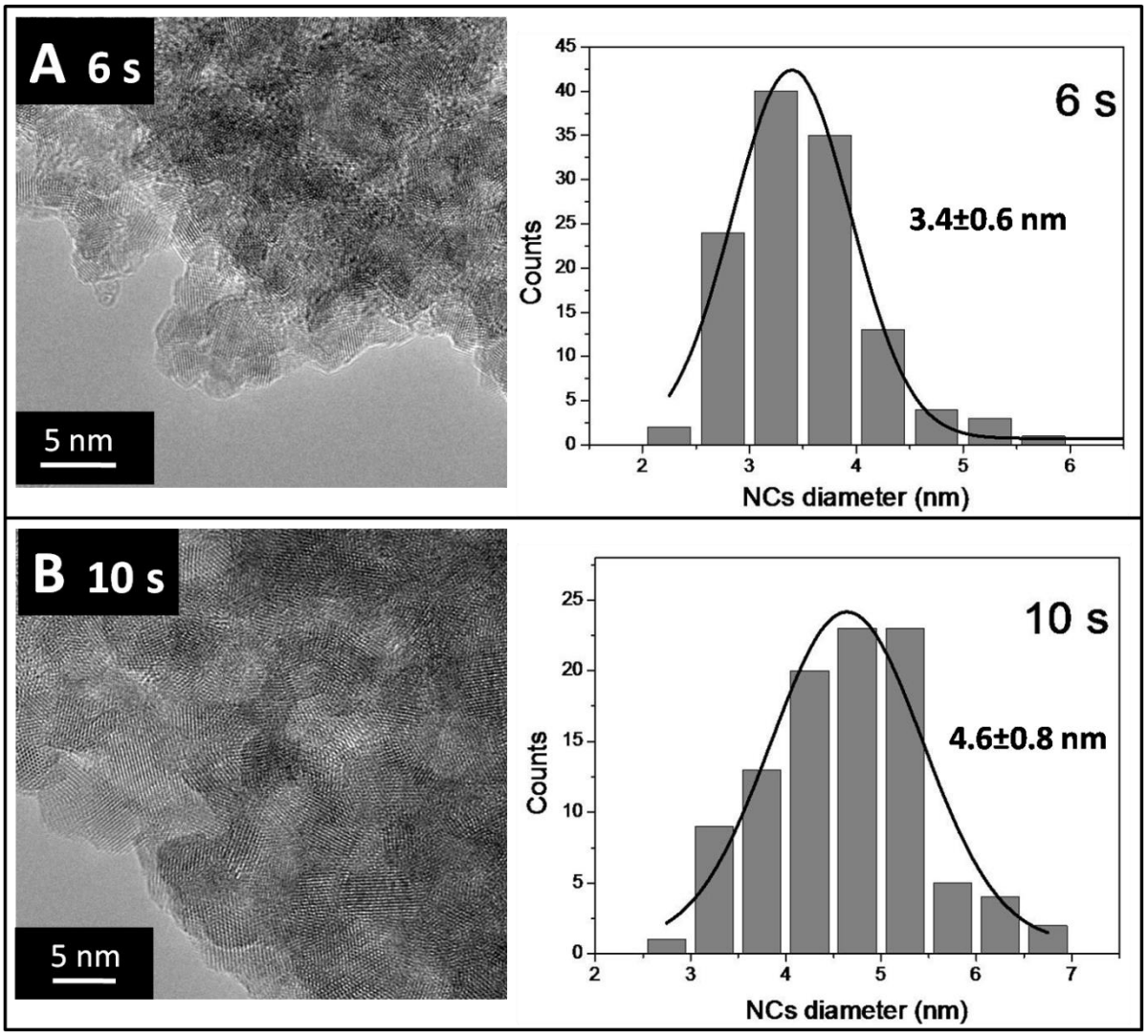

Figure III-6. HR TEM micrographs of ZnO_2 nanoparticles and corresponding histograms for the sample obtained with a residence time of 6 s (A) and a sample obtained with a residence time of 10 s.

Figure III-6 shows agglomerated particles. The inhomogeneous color can be related to residual porosity between the superimposed particles.

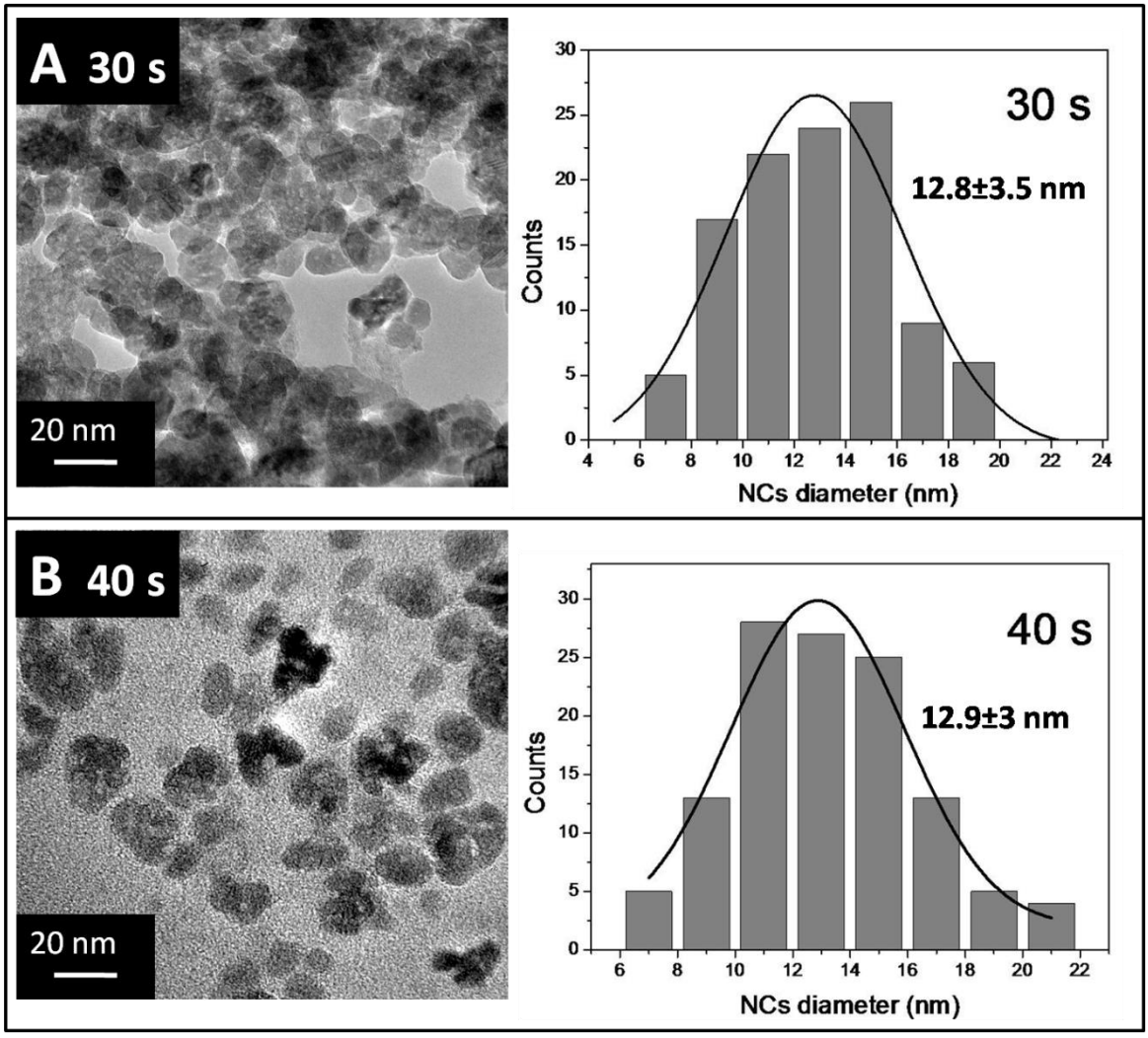

Figure III-7. HR TEM micrographs of ZnO_2 nanoparticles and corresponding histograms for the sample obtained with a residence time of 30 s (A) and a sample obtained with a residence time of 40 s.

TEM measurements show that ZnO_2 and ZnO nanoparticles have a more or less spherical morphology. The size of nanoparticles is increasing with residence time from 3.4±0.6 nm to 4.6±0.8 nm for ZnO_2 nanoparticles obtained at 6 s and 10 s residence times, respectively. The size is still increasing to 12.8 – 12.9 nm after the transformation of ZnO_2 to ZnO. However, there is no nanoparticles size difference between the nanoparticles obtained at 30 s and 40 s residence times. This shows that the Zn precursor is completely decomposed after 30 s residence time in the reactor. The TEM micrographs obtained at high magnification demonstrate a good crystallinity of these nanoparticles which is a characteristic of nanoparticles formed in supercritical fluids.

As it was mentioned before, ZnO_2 is a compound with a quite low decomposition temperature. A number of studies of decomposition temperature on ZnO_2 at nanoscale are reported in literature [7, 10-11, 14-15]. Thanks to TGA, Kim et al. [7] have reported thermal decomposition of ZnO_2 to ZnO at 189 ˚C. Uekawa et al. [10] have observed thermal decomposition at 227 ˚C for ZnO_2 nanoparticles of about 20 nm, while Sun et al. [11] have observed the decomposition of ZnO_2 at about 240 ˚C for nanoparticles of about 100 nm. Prikhodchenko et al. [14] have measured the decomposition of 4-5 nm ZnO_2 nanoparticles at 180 ˚C, while Wolanov et al. [15] have observed decomposition of 5 nm sized ZnO_2 nanoparticles at about 160 ˚C. This literature data are summarized in Table III-1. Thereby, as it was reported in the literature, the decomposition temperature of ZnO_2 nanoparticles depends on nanoparticles size and also the decomposition temperature could increase if ZnO_2 nanoparticles are agglomerated [14-15].

Table III-1. Summary of literature data of ZnO_2 nanoparticles decomposition temperatures.

Synthetic method	Agglomeration	Size (nm)	Decomposition temperature (˚C)	Ref.
Organometallic	Agglomerated	-	189	7
Precipitation of $Zn(OH)_2$ by H_2O_2	Agglomerated	30-55	212	10
Sol-gel	Agglomerated	100	230	11
Precipitation of $Zn(OH)_2$ by H_2O_2	High agglomerated	4-5	180	14
Precipitation of $Zn(OH)_2$ by H_2O_2	Agglomerated	5	160	15

In order to investigate the decomposition temperature of our ZnO_2 nanoparticles TG analysis has been performed. Figure III-8-A shows the TGA curves for the samples obtained with 6 s, 10 s and

40 s residence times. In the case of 40 s sample when pure ZnO NCs are formed TGA curve has two main weight loss steps – 0.6 wt.% and 5.6 wt.%.

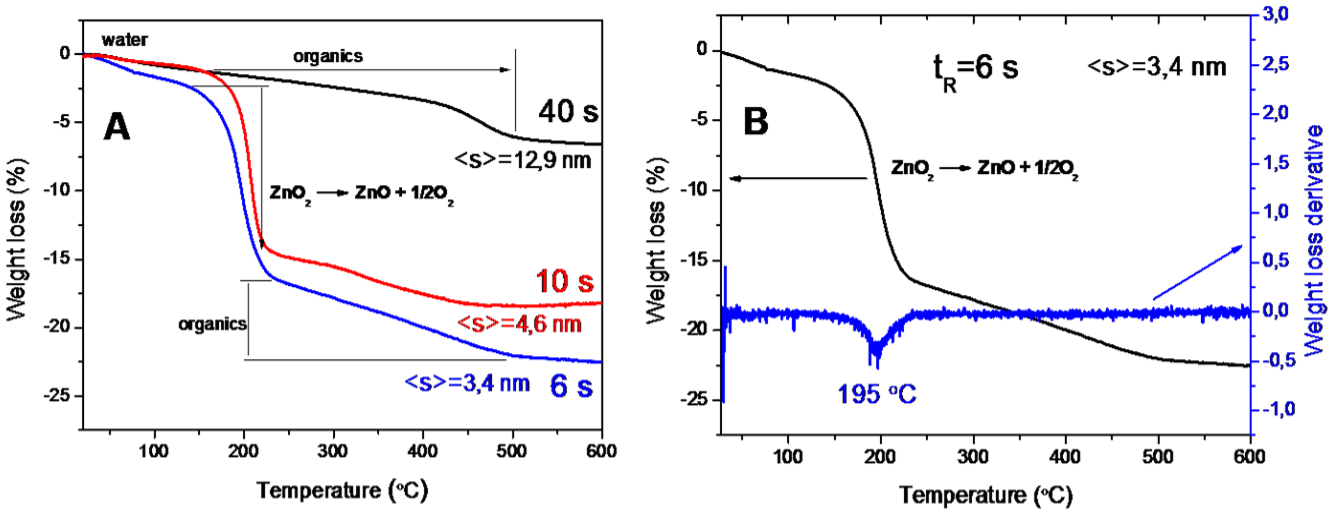

Figure III-8. TGA curves of the samples obtained with 6, 10 and 40 residence times (A) and TGA with derivative function of 6 s residence time sample.

The first weight loss step could be attributed to water from the atmosphere. The second weight loss step is attributed to physi- and chemisorbed organic molecules which could appear on ZnO NCs surface as acetylacetonate (Chapter II, Figure II-10 TGA). The TGA curves of the samples obtained with 6 s and 10 s residence times are different from the 40 s residence time. There are three weight loss steps – 1.3 wt.%, 14.1 wt.%, 5.7 wt.% and 0.53, 13.6, 4.2 wt.% for 6 s and 10 s residence time samples, respectively. As in the case of 40 s residence time sample, first and third weight loss steps could be attributed to water and acetylacetonate from the precursor. There is a good agreement between these values for the three samples. The second step which is centered at 195 ˚C (Figure III-8-B) can be attributed to the thermal decomposition of ZnO_2 in ZnO, for 6 s and 10 s residence time samples, in good agreement with the evolution of XRD patterns as a function of temperature (Figure III-4). According to these data, the sample prepared with 6 s residence time consists of 88 wt.% of ZnO_2, 1.4 wt.% of water, 5.7 wt.% of organics and still 4.8 wt.% is not decomposed. The sample obtained with 10 s residence time has 85 wt.% of ZnO_2, 0.5

wt.% of water, 4.2 wt.% of organics and there is still 10.3 wt.% of undecomposed part. The quantity of this undecomposed part is increasing with residence time. Thereby, the undecomposed part could be attributed to ZnO phase. Therefore, TGA also show the presence of ZnO phase in ZnO_2 samples which are obtained with lower residence time which is with a good agreement with data observed using Raman spectroscopy.

The thermal behavior of the sample obtained with 40 s residence time is expected to be ZnO due to its high thermal stability [16]. TGA curves for the samples obtained with lower residence time have weight loss step at 195 ˚C which is attributed to the thermal decomposition of ZnO_2 to ZnO and molecular oxygen. It was also proved by high temperature XRD measurements for sample obtained at 6 s residence time. TGA also shows that ZnO_2 and ZnO NCs could be surrounded by organics which are from the precursor – acetylacetonate (Chapter II, Figure II-8 FTIR).

All the aforementioned results confirm that ZnO NCs are formed through ZnO_2 nanoparticles which play a role of intermediate phase. A last point still needs to be confirmed before the ZnO NCs formation mechanism discussion; is there really the presence of ZnO in ZnO_2 NPs as it was observed by Raman spectroscopy and TGA. In order to confirm the presence of ZnO into ZnO_2 NPs, XPS measurements have been performed for the samples obtained at 6 s and 40 s residence times. Figure III-9 shows XPS survey spectra of the sample obtained with 6 s residence time at low and high energy regions. The survey spectra of ZnO_2 sample have several lines which can be attributed to $Zn_{3s, 3p}$, O_{1s}, C_{1s} atoms. Additionally, these spectra exhibit Auger lines of Zn atoms such as ZnML1 and ZnML2 peaks. The spectra of ZnO NCs sample obtained with a residence time of 40 s (not shown here) have similar shape as for ZnO_2 sample.

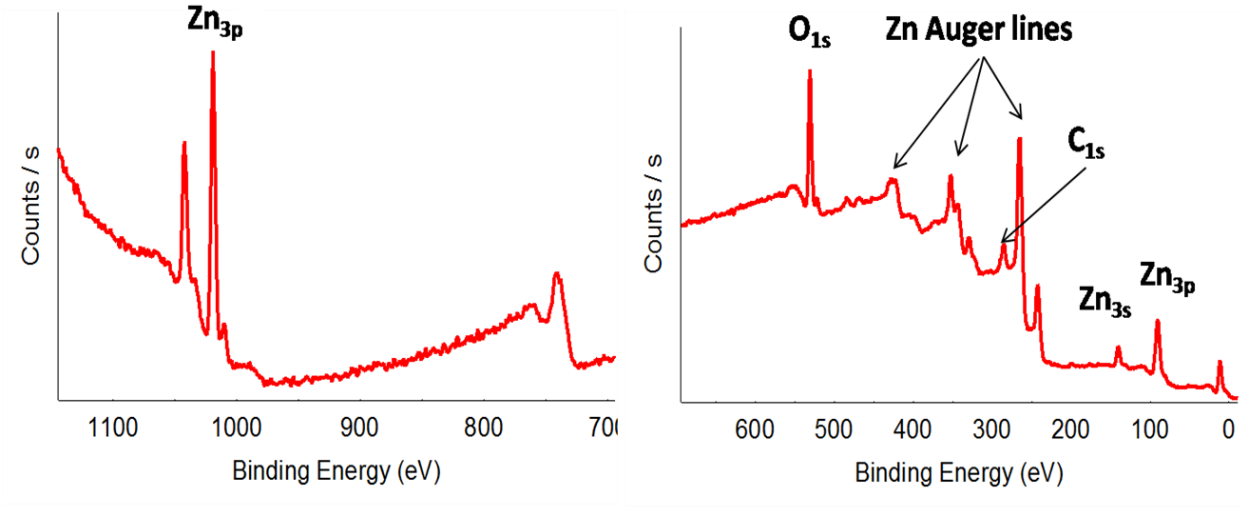

Figure III-9. XPS survey spectra at low (right) and high (left) energy regions of ZnO_2 sample obtained with 6 s residence time.

Figure III-10 shows high resolution XPS spectra on Zn_{3p} atom measured for both samples. The spectra for 6 s and 40 s residence time samples can be fitted with only one function with an energy maximum of 1020.6 eV and 1021.8 eV, respectively.

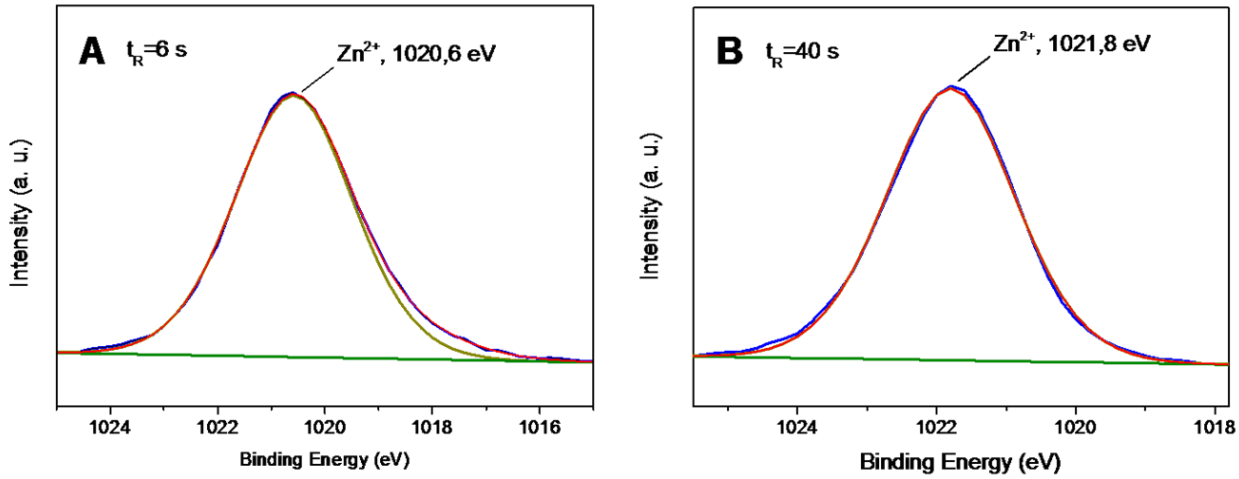

Figure III-10. High resolution XPS spectra on Zn_{3p} atom of the sample obtained with 6 s (A) and 40 s (B) residence times.

These fits show that all Zn atoms have Zn^{2+} oxidation state for both samples. High resolution XPS spectra were measured also on O_{1s} atoms in order to get the information concerning the presence of ZnO phase in ZnO_2 nanoparticles for the samples obtained with 6 s and 40 s residence times.

Figure III-11-A shows XPS spectrum of the sample obtained with 6 s residence time. This spectrum can be fitted with three functions corresponding to binding energies – at 530.6 eV, 532.2 eV and 533.2 eV.

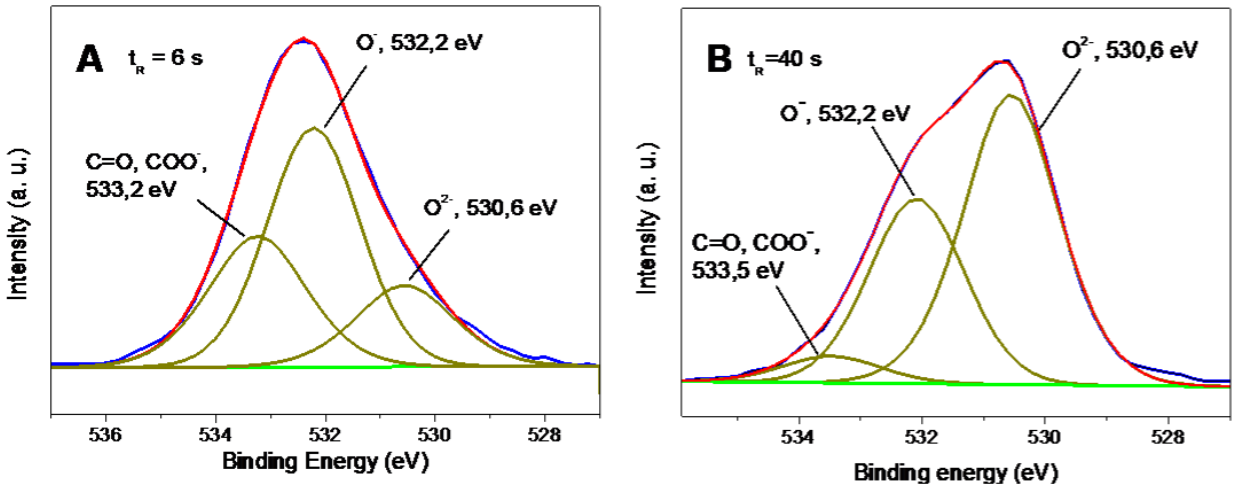

Figure III-11. High resolution XPS spectra measured on O_{1s} atom for the samples obtained with 6 s and 40 s residence times.

According to Dupin at al. [17] the binding energy of O_{1s} atom in the range of 527 – 530 eV is characteristic of O^{2-} ions in metal oxides. The binding energy in the range of 530.6 – 531.1 eV is characteristic of oxygen specie integrated in the material O_2^{2-}. The binding energy in the range of 531.1 – 532 eV is due to low coordinated oxygen species which could be described as "O^-" ions. Khallaf et al [18]. have also reported O_{1s} XPS spectra for ZnO_2, the observed binding energy for ZnO_2 is equal to 532 eV, while annealed ZnO_2 sample exhibits XPS line at 530 eV corresponding to ZnO. Thereby, the binding energies of O_{1s} atom in the sample obtained with a residence time of 6 s at 530.6 eV, 532.2 eV and 533.2 eV could be attributed to O^{2-}, $O^-$from O_2^{2-} ions and oxygen originated from the organic functions as C=O, COO^-, respectively.

High resolution O_{1s} XPS spectrum of the sample obtained with 40 s residence time is presented in Figure III-11-B. As in the previous case, this spectrum can be fitted with three functions with corresponding binding energies of 530.6 eV, 532.2 eV and 533.5 eV, these binding energies being

also attributed to O^{2-}, O^{-} and C=O, COO^{-}, respectively. Table III-2 shows the quantification of the oxygen species calculated form XPS spectra for the samples obtained with 6 and 40 s residence time. As it can be seen, O^{2-} and O_2^{2-} ions are present in both samples. However, the quantitative ratio of these ions is different for each sample.

Table III-2. Quantification of O^{2-} and O^{-} oxygen species in the samples obtained with a residence times of 6 s and 40 s.

Type of oxygen specie	ZnO_2, 6 s Quantity (at.%)	ZnO, 40 s Quantity (at.%)
O^{2-}	9.02	22.67
O^{-}	24.53	14.09

It should be noted that XPS is a "surface" technique and the obtained information relates to the near surface region of investigated material. However, as it was demonstrated by TEM, the nanoparticles size of the sample obtained with a residence time of 6 s is about 3.4 nm. In this case, the observed XPS data could relate not only to the surface but also to part of the "bulk" properties; this shows that ZnO phase could be placed at the center of spherical ZnO_2 nanoparticles. On the other hand, the observed XPS data for the nanoparticles of the sample prepared at 40 s residence time is related only to the surface properties due to their bigger average size equal to 12.9 nm; this fact allows concluding that ZnO_2 phase is still presents at the surface of ZnO NCs obtained at higher residence time.

In conclusion, four samples have been obtained at different residence times and investigated by XRD, Raman, TGA, HRTEM and XPS measurements. XRD patterns and Raman spectra are demonstrating that ZnO NCs with würtzite structure are formed at higher residence times (30 s and 40 s), while at lower residence times (6 s and 10 s) a ZnO_2 cubic phase is formed as an intermediate phase. The nanoparticle size, size distribution and morphology of the samples obtained with all residence times were evaluated by TEM. These measurements show that all samples exhibit a more or less spherical morphology. TEM measurements demonstrate a strong

nanoparticles size dependence on residence time; the average nanoparticle sizes are equal to 3.4 nm, 4.6 nm, 12.8 nm and 12.9 nm for 6 s, 10 s, 30 s and 40 s residence times, respectively. The nanoparticle size is increasing with a residence time increasing from 6 s up to 30 s, while the nanoparticles size of the sample obtained at 40 s is equal to that of 30 s residence time sample (12.8-12.9 nm) showing complete decomposition of Zn precursor in our conditions at residence times higher than 30 s. XRD as a function of temperature and TGA measurements are showing the decomposition temperature of ZnO_2 in ZnO at 195 ˚C which is in a good agreement with literature data.XPS data observed for Zn_{3p} demonstrate that Zn is presenting only in 2+ oxidation state in both samples observed at lower (6 s) and higher (40 s) residence times. XPS of O_{1s} peak shows the presence of ZnO phase in ZnO_2 nanoparticles obtained at 6 s residence; moreover, ZnO phase could be located not only on the surface of ZnO_2 nanoparticles but also on their core due to their small size. On the other hand, ZnO_2 phase is observed in the case of ZnO NCs prepared with a residence time of 40 s; however, in this case ZnO_2 phase is observed on the surface of ZnO NCs due to their size bigger than a XPS resolution.

II. ZnO NCs formation mechanism

In this paragraph, the discussion concerning ZnO NCs formation mechanism in continuous supercritical fluids route is proposed. Obviously, the formation mechanism of ZnO NCs can influence the physico-chemical characteristics of this material. Therefore, a better understanding of the mechanism should play an important role for further investigation of physico-chemical properties of ZnO NCs, especially the understanding of such unique optical properties of ZnO NCs obtained with our SCFs route.

The data observed from XRD, Raman spectroscopy, TGA and XPS shows that ZnO_2 nanoparticles are formed at low residence times, while ZnO NCs are observed at higher residence times. This suggests that ZnO_2 plays the role of intermediate phase in the synthesis of ZnO NCs through the transformation of $Zn(acac)_2{\cdot}H_2O$ in the presence of H_2O_2. Some reports confirm that ZnO_2 nanoparticles can be synthesized through the transformation of different precursors in the presence of H_2O_2 [2, 4, 7-9, 11, 19-21]. For example, Escobedo-Morales et al. [2] have obtained ZnO_2 nanoparticles through the hydrothermal transformation of $Zn(CH_3COO)_2{\cdot}2H_2O$ with H_2O_2 at 100 ˚C during 10 h. Pál et al. [19] and Sebők et al. [20] have reported the transformation of $Zn(CH_3COO)_2{\cdot}2H_2O$ with H_2O_2 under *hv* irradiation forming ZnO_2 nanoparticles in 4 h and 6 h. ZnO_2 nanoparticles have also been synthesized through the direct transformation of $Zn_5(CO_3)_2(OH)_6$ in the presence of H_2O_2 at 100-170 ˚C for 6 h [21], 80-120 ˚C for 6-18 h [9] and at room temperature for 24-72 h [8]. ZnO_2 nanoparticles formation has also been observed using H_2O_2 and other precursors such as zinc (II) 2-ethylhexanoate (instantaneously) [4] and zinc (II) isobutylcarbamate 0.5 h [7]. Moreover, ZnO_2 nanoparticles can also be prepared through the treatment of ZnO nanostructures in H_2O_2 aqueous solution at 120 ˚C for 6 h [22]. Therefore, different zinc precursors and even ZnO nanostructures can be transformed to ZnO_2 nanoparticles.

We can claim that, entering the supercritical fluid reactor, $Zn(acac)_2 \cdot H_2O$ reacts with H_2O_2 to induce the nucleation and growth of ZnO_2 following:

$$Zn(acac)_2 \cdot H_2O + H_2O_2 \rightarrow ZnO_2 + 2Hacac + H_2O \qquad \text{(eq. 1)}$$

As it was discussed before, ZnO_2 nanoparticles formed through the transformation of $Zn(acac)_2 \cdot H_2O$ in the presence of H_2O_2 at low residence time is thermally decomposed forming ZnO NCs with increasing residence time following:

$$ZnO_2 \rightarrow ZnO + \tfrac{1}{2}O_2 \qquad \text{(eq. 2)}$$

It should be noted that initially the solutions contain precursor and H_2O_2 in ethanol (Solution 1) and pure ethanol (Solution 2) at room temperature. These solutions are injected into the supercritical fluid reactor. Therefore, it is important to obtain a detailed temperature profile along the reactor depending on the tubing diameter.

Heat transfer in a pipe, for which walls are at a uniform temperature is known as the Graetz-Nusselt problem (Figure III-12). The system coordinates and boundary conditions are summarized in Figure III-12. The center of the tube is set to r = 0 and we study a fluid flowing in a tube of radius r. The fluid enters at a temperature T_e until it reaches the area where the walls of the tube are brought uniformly and consistently to a temperature T_w. The aim is to solve the problem for $z > 0$, while remaining close to the center of the tube.

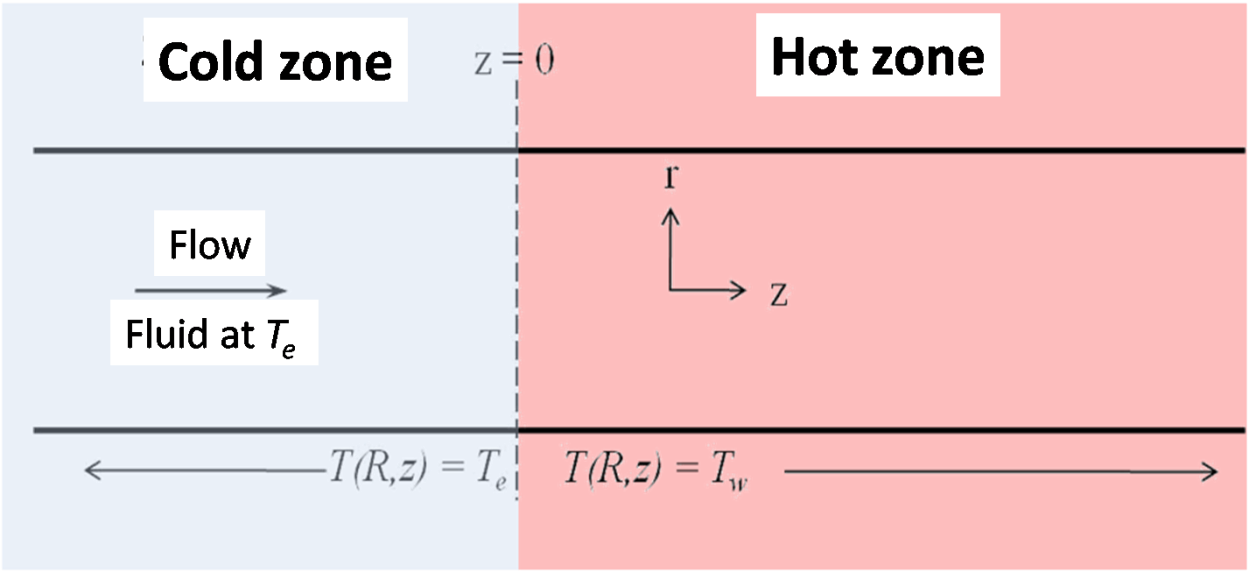

Figure III-12: System coordinates and boundary conditions of the Graetz-Nusselt problem (from [23]).

Our experimental set-up can be simplified to the Graetz-Nusselt problem by assuming a negligible longitudinal heating (compared to radial heating). The temperature profile in the steady state is obtained by solving the equation of energy equivalence:

$$\rho c_v \frac{\partial T}{\partial t} + [\rho v c_v \nabla T] = \nabla(\lambda \nabla T) - T\left(\frac{\partial p}{\partial T}\right)_p (\nabla . v) + \phi_\mu \qquad \text{(eq. 3)}$$

Where, for a given fluid, ρ is the density ($kg.m^{-3}$), c_v is the heat capacity at constant volume ($J \cdot kg^{-1} \cdot K^{-1}$), v the fluid velocity ($m.s^{-1}$), T the temperature (K), t the time (s), λ the thermal conductivity ($W \cdot m^{-1} \cdot K^{-1}$) and ϕ_μ the viscous dissipation ($W.m^{-3}$).This equation can be solved analytically is if some simplifications are applied to the problem. In particular, assuming negligible dissipation due to the viscosity, constant fluid density and specific heat capacity, while the fluid is considered incompressible ($\nabla \cdot v = 0$). In our experimental procedure, the fluids are initially injected in liquid form at high pressure before being heated to reach the supercritical domain. The Graetz-Nusselt problem in this case becomes much more complex, since it has to take into account all the contributions and variables of the equation of energy equivalence (no simplifications can be made).

It is no longer possible to solve this problem analytically since we are dealing with a transcritical flow. However, this problem can be solved numerically. This was achieved through a collaboration with Jalil Ouazzani (ARCOFLUID company), who has developed an algorithm using the formulation of the energy equation including the heat capacity at constant volume (C_v). This algorithm is applied to supercritical fluid flows (using a non-linear Van der Waals equation of state) and to gas flows (ideal gases equation of state). It is introduced into a code using the SIMPLE and SIMPLER method sand works within the PHOENIX software to simulate this type of fluid behavior.

Figure III-13 shows the simulation curve of temperature profile along the C_4 reactor for the experiment at 6 s residence time (the heated length of the reactor is 30 cm).

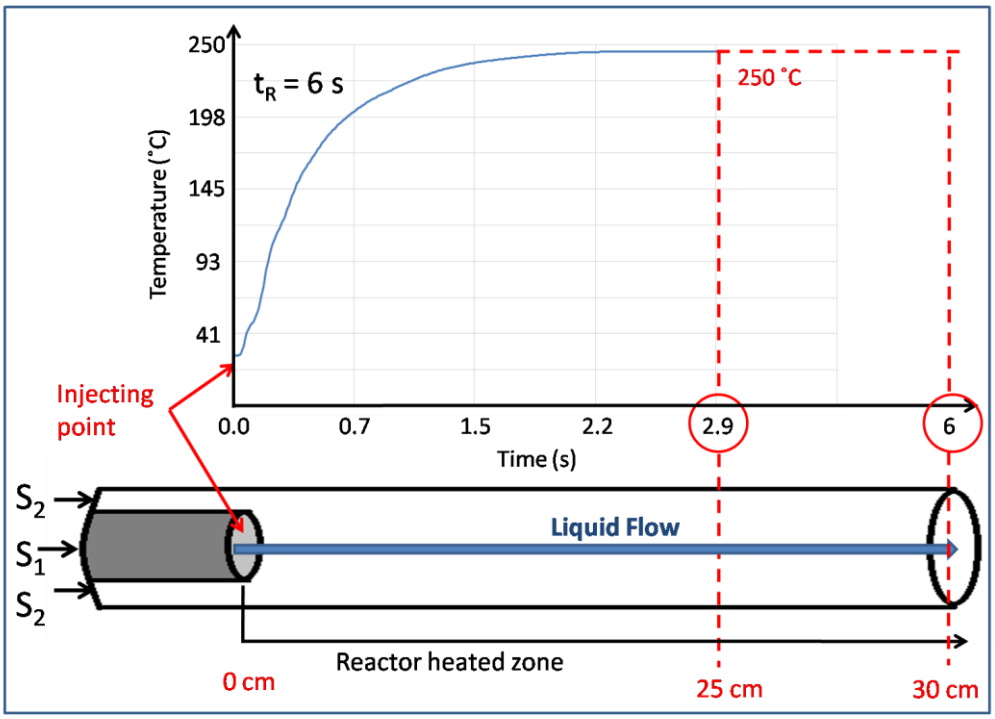

Figure III-13. Temperature profile inside the reactor for a 6 s residence time experiment.

As it can be seen from the graph, the reaction medium is reaching 250 ˚C after 2.9 s of residence time corresponding to fluid flow at 25 cm point in the reactor. Therefore, ZnO_2 nanoparticles could be formed before their decomposition temperature in this process and if residence time is short

enough not all ZnO_2 phase will decompose to ZnO. As it was noted previously, some percentage of ZnO phase has been observed by Raman spectroscopy and XPS. These observed data are in good agreement with the calculated temperature profile for the experiment performed at 6 s residence time, because according to the profile curve the fluid is reaching high temperature after a few seconds inducing the thermal decomposition of ZnO_2 nanoparticles forming ZnO phase. Therefore, ZnO_2 intermediate nanoparticles could be stabilized and recovered in the experiments at 6 s and 10 s residence times. A similar calculation of the temperature profile for the same C_4 reactor was performed for the experiment with a residence time of 40 s (Figure III-14).

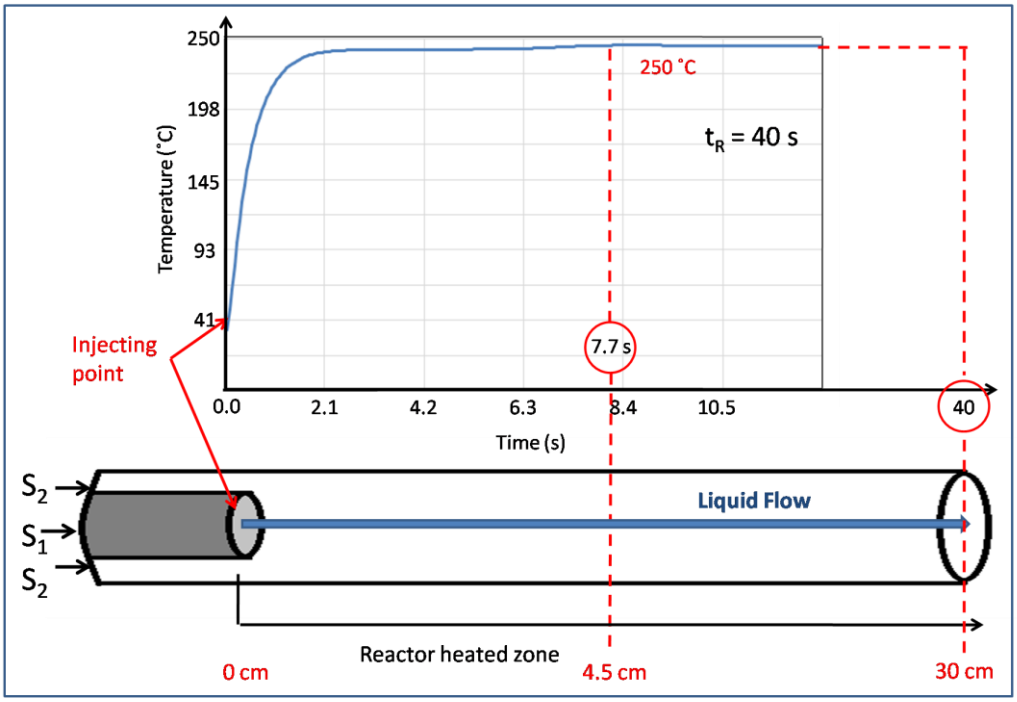

Figure III-14. Temperature profile into the reactor for a 40 s residence time experiment.

In this case, the reaction media is heated up to 250 ˚C at 7.7 s of residence time. At this time, fluid flow reaches 250 ˚C at 4.5 cm of reactor length i. e. close to the beginning of the reactor. Therefore, ZnO_2 nanoparticles which initially appear through the transformation of $Zn(acac)_2{\cdot}H_2O$ in the presence of H_2O_2 can be fully transformed to ZnO NCs when residence time of the experiment is long enough (30 s and 40 s).

Temperature profile calculations for the experiments performed with 6 s and 40 s residence times are in good agreement with XRD, Raman, HRTEM, TGA and XPS data where ZnO_2 nanoparticles have been observed at low residence time, while ZnO NCs appear with increasing residence time value. Thereby, ZnO NCs in our continuous SCFs method are formed in two steps: (i) the formation of ZnO_2 nanoparticles through the transformation of $Zn(acac)_2 \cdot H_2O$ in the presence of H_2O_2 (see eq. 1); (ii) and the thermal induced decomposition of ZnO_2 nanoparticles forming ZnO NCs (see eq. 2).

As it was discussed before, TEM measurements for the samples obtained at different residence times show that the nanoparticles size is increasing with increasing residence time from 6 s up to 30 s, while ZnO NCs obtained at 40 s demonstrate the same size as NCs prepared at 30 s residence time. Such behavior could occur due to complete transformation of $Zn(acac)_2 \cdot H_2O$ in the presence of H_2O_2 to ZnO_2; moreover, 30 s residence time is enough for full thermal decomposition of ZnO_2 to ZnO. This could also confirm the growth of ZnO NCs through the thermal decomposition of ZnO_2 phase. On the other side, XPS data observed on 6 s residence time sample show 9.02 at.% of ZnO phase in these nanoparticles. This phase could present the ZnO nuclei inside of these nanoparticles (XPS data could be attributed to all volume for these nanoparticles due to their small size of 3.4 nm). On the other hand, ZnO_2 phase was observed on XPS spectrum measured for the sample obtained at 40 s residence time. This data can illustrate only near surface region of these ZnO NCs due to their bigger size (12.9 nm) than in the case of 6 s. Thereby, ZnO_2 phase in ZnO NCs obtained at higher residence time is located on the surface of these NCs.

Such observed data suggest the hypothesis of ZnO NCs growth. The growth of ZnO NCs could result from three processes (Figure III-15): (i) the nucleation of ZnO_2 nanoparticles trough the transformation of $Zn(acac)_2 \cdot H_2O$ in the presence of H_2O_2; (ii) the growth of ZnO_2 nanoparticles until complete consumption of $Zn(acac)_2 \cdot H_2O$ with the nucleation of ZnO phase at the center of

these nanoparticles and (iii) ZnO growth from center to surface of ZnO_2 nanoparticles through the thermal decomposition of ZnO_2. Thereby, ZnO NCs are formed from the growth of ZnO_2 nanoparticles and their fast decomposition into ZnO NCs.

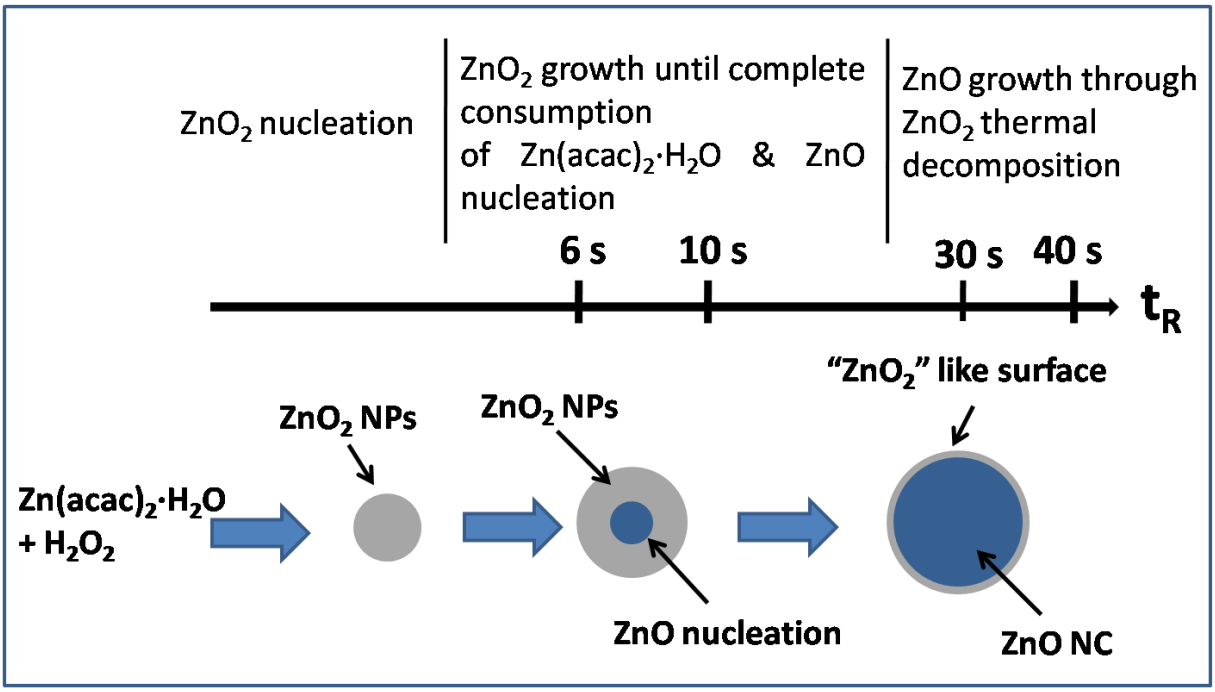

Figure III-15. Scheme of ZnO NCs growth through ZnO_2 thermal induced decomposition in SCFs reactor.

It should be noted that the presence of H_2O_2 in the reaction media even at supercritical conditions [24-25] makes ZnO_2 nanoparticles growth possible even at 250 ˚C. This hypothesis for the growth of ZnO NCs through ZnO_2 thermal decomposition is in good agreement with XPS data for the sample obtained with a residence time of 40 s and explains the observation of ZnO_2 phase on the surface of ZnO NCs. Thereby, the surface of ZnO NCs obtained by SCFs route is covered by "ZnO_2" like surface state.

As it was noted before, the formation mechanism is critical to understand the physicochemical properties of ZnO NCs. The nanomaterials synthesized through the supercritical fluids route usually demonstrate high crystallinity [26-29]. Thereby, high crystallinity of ZnO NCs obtained with SCFs route could exclude the crystal defects and as a consequence the visible emission from

these defects is quenched. However, such small size of ZnO NCs obtained in our work should give a large contribution of the surface in comparison with bulk making surface defects appearance resulting with a visible emission. However, as it was demonstrated before (Chapter II) ZnO NCs obtained with our synthetic method show only UV emission in their room temperature PL spectra, while the visible emission is totally absent (Figure III-16-A).

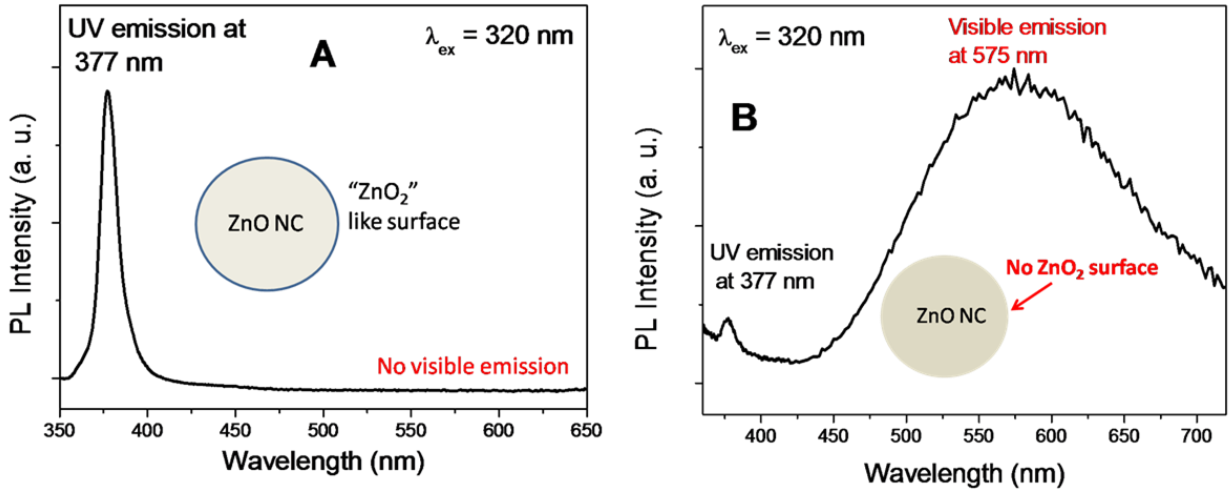

Figure III-16. Room temperature PL spectra of ZnO NCs obtained at 40 s residence time in the presence of H_2O_2 (A) and without using H_2O_2 (B).

The absence of the visible emission related to the crystal defects could be explained by the high crystallinity of these NCs. However, the absence of the surface defects and as a result the quenched visible emission is quite surprising. To explain this experimental fact one hypothesis could be proposed: the surface defects in ZnO NCs obtained by our SCFs route are "blocked" by the specific surface state namely – "ZnO_2" like surface of ZnO NCs. This hypothesis could be proposed according to XPS data where binding energy related to "O^-" species from O_2^{2-}peroxide ion has been observed on the surface of ZnO NCs obtained with a residence time of 40 s. In order to prove this hypothesis one experiment was performed: ZnO NCs were prepared using routine way (residence time is 40 s) but H_2O_2 was not added into reaction media $(Zn(acac)_2 \cdot H_2O$ is transformed in the presence of water in ethanol/water mixture). Obviously, the formation of "ZnO_2" like surface

on ZnO NCs is impossible in this case. Room temperature PL spectrum of this sample is shown on Figure III-16-B and seems to be different to that measured for reference sample. This spectrum exhibits two types of PL emission: less intensive UV emission peak at 377 nm and more intensive red band in the visible region (575 nm) of the spectrum. This band in the visible domain of PL spectrum could be attributed to the surface defects of ZnO.

To prove the existence of "ZnO_2" like surface on ZnO NCs prepared with 40 s residence time with H_2O_2, we have provided a heat treatment of this sample at 350 ˚C (increase rate 150°C/hour, step 1 hour at 350°C and free decrease). In this experiment we could expect the thermal decomposition of "ZnO_2" like surface which covers ZnO NCs and, as a result, we could observe visible emission in PL spectra. Figure III-17 shows room temperature PL spectra of ZnO NCs before and after heat treatment.

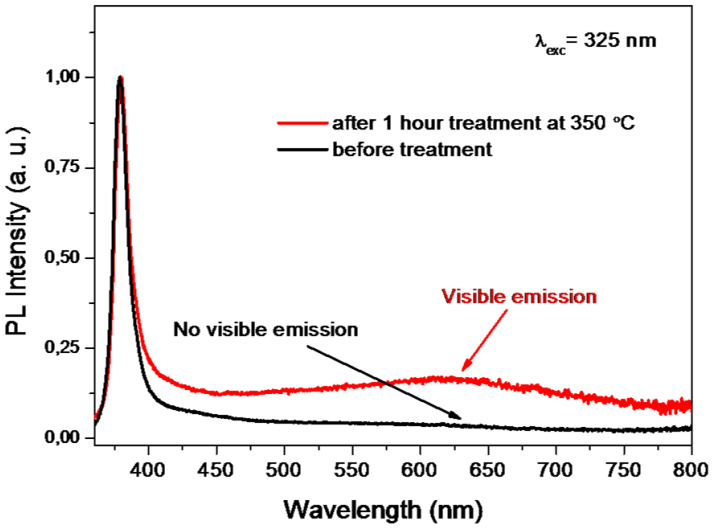

Figure III-17. Normalized room temperature PL spectra of ZnO NCs obtained with H_2O_2 at 40 s residence time before and after heat treatment.

As it was expected, the visible emission at 600 nm is observed on the sample after a heat treatment during 1 hour. However, the effect of heat treatment is low in comparison with that observed on the sample prepared without using H_2O_2. So, this means that the emission of defects is also linked to the existence of core defect. It exists probably due to the migration of defects from the surface

to the core which can explain the instability of visible emission in sol gel route. Thereby, in our case, heat treated sample could show the additional contribution of bulk defect.

Thereby, the formation mechanism of ZnO NCs plays definitely a role on the optical properties of these NCs. Moreover, a deep understanding of the features of the formation mechanism allows controlling these properties. Thereby, pure UV emission in PL spectra of ZnO NCs could be explained by two features of our SCFs synthetic method: (i) high crystallinity of ZnO NCs which can be achieved in this method and (ii) "ZnO_2" like surface of ZnO NCs which is blocking surface defects; this is given by an originality of ZnO NCs nucleation and growth process through ZnO_2 intermediate nanoparticles in supercritical fluids.

Conclusion:

The formation of ZnO NCs as a function of residence time in our continuous supercritical fluids process has been investigated for the first time. The structural, morphological and surface properties of the samples have been characterized using XRD, Raman, HR TEM, TGA, FTIR and XPS techniques. ZnO NCs which are formed at high residence times (30-40 s) exhibit hexagonal würtzite type structure of ZnO, while the samples obtained with low residence time (6-10 s) have body-centered cubic structure, which is attributed to zinc peroxide (ZnO_2). In all cases, the samples obtained with different residence times have spherical morphology. The size of spherical nanoparticles is increasing with residence time. The ZnO_2type samples obtained with low residence times (6-10 s) can decompose at around 195 ˚C. This was also confirmed by high temperature XRD measurements. Thereby, we demonstrate that ZnO NCs formation in our continuous supercritical fluids method goes through ZnO_2 intermediate phase. The following growth of ZnO NCs could be realized through the thermal decomposition of ZnO_2 intermediate nanoparticles. ZnO NCs obtained at high residence time have "ZnO_2" like surface which blocks surface defects quenching visible emission in their PL spectra. Room temperature PL spectrum of ZnO NCs obtained without using H_2O_2 exhibits strong and intensive defect emission. Moreover, appearance of defect emission in ZnO NCs sample obtained at 40 s with H_2O_2 after heat treatment could also confirm our hypothesis that "ZnO_2" like surface blocks the surface defects. High crystallinity and "ZnO_2" like surface state in ZnO NCs obtained with SCFs route determine pure UV-emitting optical properties of these NCs. To understand better the nature of this UV emission in ZnO NCs, Room and low temperature PL measurements have been performed for the samples obtained at 6 s and 40 s residence time. All results and discussions concerning the nature of PL emission of ZnO NCs obtained with our SCFs method are demonstrated in next Chapter.

References

1. N. G. Vannerberg, Ark. Kemi, 1959, 14, 119.
2. A. Escobedo-Morales et al. J. Cryst. Growth, 2011, 316, 37.
3. S. Cheng et al. J. Phys. Chem. C, 2009, 113, 13630.
4. K. Pemartin et al. Chem. Lett., 2012, 41, 1032.
5. L. Rosenthal-Toib et al. Chem. Eng. J., 2008, 136, 425.
6. T. C. Damen et al. B. Tell, Phys. Rev., 1966, 142, 570.
7. K.-A. Kim et al. Bull. Korean Chem. Soc., 2014, 35, 431.
8. L. Y. Yang et al. Mater. Lett., 2010, 64, 1647.
9. G. Feng et al. Particuology, 2012, 10, 388.
10. N. Uekawa et al. Phys. Chem. Chem. Phys., 2003, 5, 929.
11. M. Sun et al. Chem. Phys. Lett., 2007, 443, 342.
12. X. Bai et al. Mater. Lett., 2010, 64, 341.
13. I. I. Vol'nov, "Peroxides, superoxides and ozonides of alkali and alkaline earth metals", Plenum Press, New York, 1966.
14. P. V. Prikhodchenko et al. J. Gun, Matter. Lett., 2014, 116, 282.
15. Y. Wolanov et al. Environ. Sci. Technol., 2013, 47, 8769.
16. L. O. Shunk et al. AIChE J, 2009, 55, 1497.
17. J-C. Dupin et al. Phys. Chem. Chem. Phys., 2000, 2, 1319.
18. H. Khallaf et al. J. Phys. B: Appl. Phys., 2009, 42, 135304.
19. E. Pál et al. J. Colloid Interface Sci., 2009, 332, 173.
20. D. Sebők et al. Appl. Surf. Sci., 2010, 256, 5349.
21. T. H. Guo. et al. Mater. Lett., 2011, 65, 639.
22. S. Z. Liu et al. Matter. Lett., 2012, 71, 154.

23. Y. Roig. Ph.D. thesis, University of Bordeaux 1, 2012.

24. A. Hiroki et al. J. Phys. Chem. B, 2005, 109, 3364.

25. E. Croiset et al. AIChE J., 1997, 43, 2343.

26. K. Byrappa et al. Prog. Cryst. Growth Charact. Mater., 2007, 53, 117.

27. F. Cansell et al. Curr. Opin. Solid State Mater. Sci., 2003, 7, 331.

28. H. Reverón et al. Nanotechnology, 2005, 16, 1137.

29. F. Cansell et al. J. Supercrit. Fluids, 2009, 47, 508.

Chapter IV

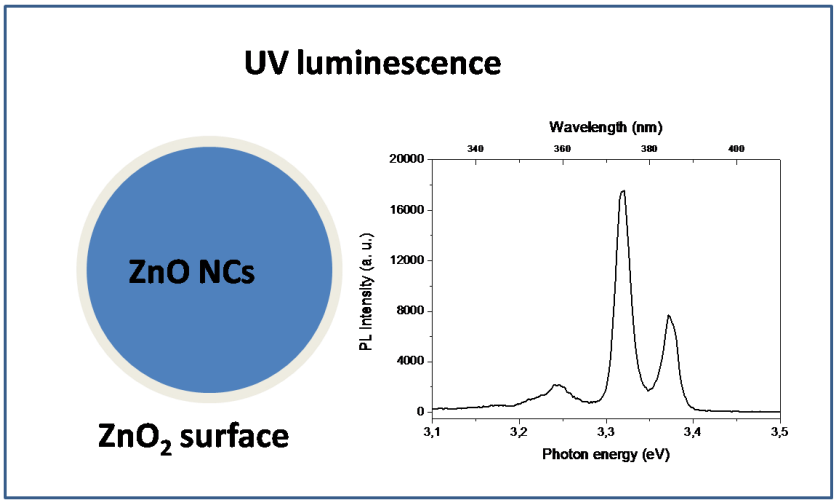
UV luminescence
ZnO NCs
ZnO_2 surface
Wavelength (nm)
340
360
380
400
20000
16000
12000
8000
4000
0
PL Intensity (a. u.)
3,1
3,2
3,3
3,4
3,5
Photon energy (eV)

Introduction

ZnO is a II-IV wide direct band gap semiconductor material with large band gap energy of 3.37 eV at room temperature. Due to its high free exciton binding energy of 60 meV, ZnO has stable efficient UV emission even at room temperature. Such properties of this material make ZnO a promising photonic material for optoelectronic applications in the near UV region.

As it was discussed in Chapter I, typical PL spectra of ZnO material at room temperature could exhibit two types of PL emission, at room temperature: (i) an emission band situated in UV region (from 360 nm to 380 nm, i.e. 3.18 eV to 3.43 eV) is related to electron-hole pair recombination (excitonic emission) and (ii) a broad band centered in the visible region (from 500 nm to 600 nm i.e. 2.07-2.48 eV) corresponds the emission from bulk and surface defects of ZnO.

As developed in Chapter I, optical properties of ZnO nanostructures strongly depend on the way of their synthesis. Over the last few decades, mostly three synthetic approaches have been developed for the production of ZnO nanostructures: (i) low temperature liquid phase approach allows the production a large dispersion of well morphology and size controlled ZnO nanostructures due to inviting different surfactant systems. However, low operating temperature of this approach results in the appearing of surface and bulk defects and, as a consequence, PL spectra of these ZnO nanostructures mostly have visible emission originated from these defects; (ii) high temperature gas phase approach allows obtaining ZnO nanostructures with high crystallinity thanks to high operating temperature allowing the exhibition of UV emission in their PL spectra, however the size and shape control of ZnO nanostructures in this approach is poor due to inability to use the surfactants; (iii) the most resent approach for the synthesis of ZnO NCs is supercritical fluids [1]; we have demonstrated in Chapters II and III that this approach allows the

production of ZnO NCs with well controlled morphology and size and, at the same time, the operating temperature is still high enough for obtaining high crystallinity of ZnO NCs. First PL measurements revealed UV emission and no signal of the defect emission in the visible range.

This chapter deeply describes room and low temperature optical properties of NCs synthesized via continuous supercritical fluids route. Room temperature PL measurements are shown for the samples obtained with different residence time and for the samples prepared with and without using TOP as surfactant. Low temperature PL and decay time measurements are also demonstrated for ZnO and ZnO_2 NCs. Discussions concerning the nature of UV emission in ZnO NCs are provided.

I. Room temperature photoluminescence properties of ZnO NCs

Room temperature PL spectra of ZnO NCs prepared by supercritical fluids route have been measured for the samples obtained with different operating conditions such as various residence times, with and without using TOP as surfactant.

As it was shown in Chapter III, ZnO NCs obtained via supercritical fluids route demonstrate high crystallinity. Moreover, the formation of ZnO NCs through ZnO_2 as an intermediate phase leads to the specific ZnO_2-like surface state which seems to neutralize the surface defects. Such crystal and surface properties of ZnO NCs obtained by SCFs route show a pure excitonic emission in their PL spectra with fully quenched visible emission (Chapter III, Figure III-16-A). On the other hand, TOP demonstrates an efficient interaction with ZnO NCs surface leading, for example, to different morphologies of ZnO NCs. In order to investigate the influence of TOP on ZnO_2 specific surface state of ZnO NCs room temperature PL spectra have been measured for two samples obtained at 40 s residence time with and without using TOP as surfactant. Figure IV-1 shows the superposition of PL spectra of these samples at near the band gap excitation wavelength (λ_{ex} = 320 nm).

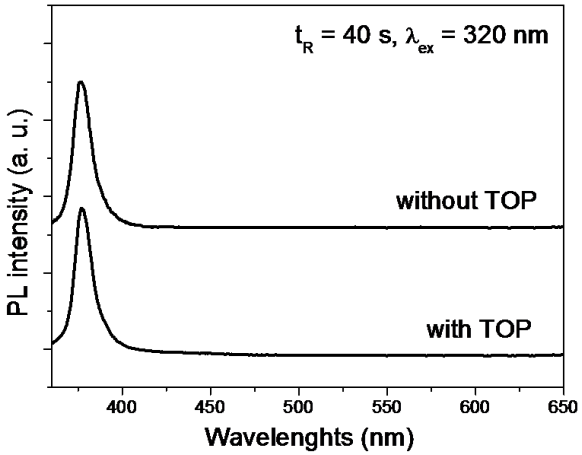

Figure IV-1. Room temperature emission spectra of ZnO NCs obtained at 40 s residence time with and without TOP. Spectra were normalized at their maximum of intensity to facilitate the comparison of spectral distribution

In both cases, ZnO NCs exhibit one intensive and narrow emission peak at 377 nm in the UV domain of the spectra. Such a result confirms that this is not a coupling of TOP ligands with NCs that neutralizes surface specific surface defects which usually give a rise to visible photoluminescence in ZnO nanomaterials. This is a direct consequence of the ZnO_2-like specific surface states on the as-prepared NCs. Thereby, the room temperature PL behavior of ZnO NCs is in a good agreement with the NCs formation mechanism which has been proposed in Chapter III due to the neutralizing of surface defects in ZnO NCs thanks to ZnO_2-like surface and as a consequence, the absence of the visible emission.

Room temperature PL spectrum of the sample obtained with 6 s residence time when ZnO_2 nanoparticles are formed is shown in Figure IV-2. As in the case of the samples obtained with 40 s residence time, 6 s residence time sample is demonstrating an excitonic emission peak in UV range for a 320 nm excitation wavelength and no visible emission was observed. Moreover, UV emission of this spectrum which is situated at 377 nm is attributed to the excitonic recombination of ZnO and at the same time, no emission peak which could appear from ZnO_2 was observed.

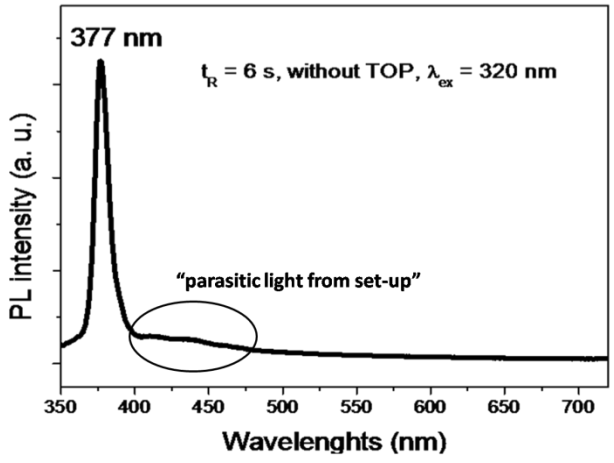

Figure IV-2. Room temperature PL spectrum of ZnO_2-type sample obtained at 6 s residence time, without using TOP as surfactant.

Such optical behavior of ZnO_2-type sample is in good agreement with the proposed ZnO NCs formation mechanism in Chapter III. The excitonic emission which is originated from ZnO in

ZnO_2-type sample obtained at 6 s residence time could be exhibited from ZnO nuclei (Figure IV-3). The XPS measurements (Chapter III, Figure III-11 XPS) show the presence of ZnO phase which is nucleating and growing from the center of ZnO_2 nanoparticle through the thermal induced decomposition of ZnO_2 phase.

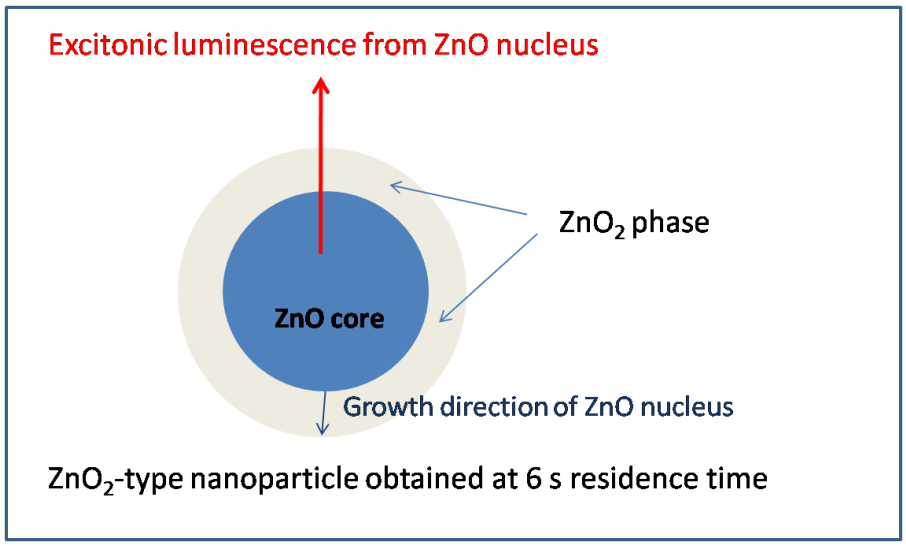

Figure IV-3. Scheme of ZnO_2-type nanoparticle: ZnO_2nanoparticle and ZnO core.

ZnO_2 is an indirect semiconductor with band gap energy E_g = 2.8-4.5 eV [2]. The band gap energy for ZnO_2 nanomaterials was measured by a number of groups and was found to be equal to 4.6 eV [3], 4.12 eV [4], 4.5 eV [5] and 4.1 eV [6]. H. Bai et al. [7] have reported room temperature PL emission spectra of ZnO_2 spherical nanoparticles. The emission spectra of ZnO_2 nanoparticles exhibit one strong band edge emission at 400 nm. This emission band was attributed to the oxygen vacancies in ZnO_2 nanoparticles. G. Feng et al. [8] have observed a wide and strong room temperature PL band in the visible region of 525-570 nm in the spectra of ZnO_2 nanocrystals. This emission band was also attributed to surface and bulk defects of ZnO_2. Kim et al. [9] have published an absorption spectrum of ZnO_2 nanoparticles which shows an absorption maximum at around 234 nm. We can conclude that if exiting, UV emission of ZnO_2 should be reabsorbed by

ZnO nuclei in our NCs prepared at 6 s residence time, absorption edge of ZnO lattice being located at 380 nm [10-11]. No visible emission of ZnO_2 was observed.

To sum up, room temperature PL measurements show that the samples obtained with various residence times and with or without TOP presence exhibit strong emission band located in the UV region of PL spectra (377 nm), while emission in the visible spectral region is fully absent. Moreover, room temperature PL measurements are in good agreement with the hypothesis of ZnO NCs formation mechanism proposed in Chapter III, i.e. (i) ZnO_2 specific surface states neutralize surface defects of ZnO NCs and (ii) ZnO nuclei starts to grow at 6 s residence time confirming the thermal induced decomposition of ZnO_2 intermediate nanoparticles to ZnO NCs. At this stage we can discard the existence of luminescent surface defects. But to check the bulk quality of ZnO NCs, it is necessary to record and analyze the emission spectra at low temperature.

II. Low temperature photoluminescence properties of ZnO NCs

Low temperature PL measurements for ZnO NCs have been carried out to better understand the nature of UV emission which was observed at room temperature. All the acquisitions were calibrated in wavelengths with a mercury lamp signal. Excitation was performed at 320 nm wavelength for all the following PL characterizations, additional measurements were recorded under 350 nm, 370 nm, 380 nm and 400 nm. As no difference in the emission graphs was observed, these spectra are not presented here.

Figure IV-4 shows typical PL spectra of ZnO NCs obtained at 40 s residence time without using TOP as surfactant and measured at 10 K and 60 K. Several narrow peaks in the region of band edge emission were observed between 3.2 eV and 3.4 eV.

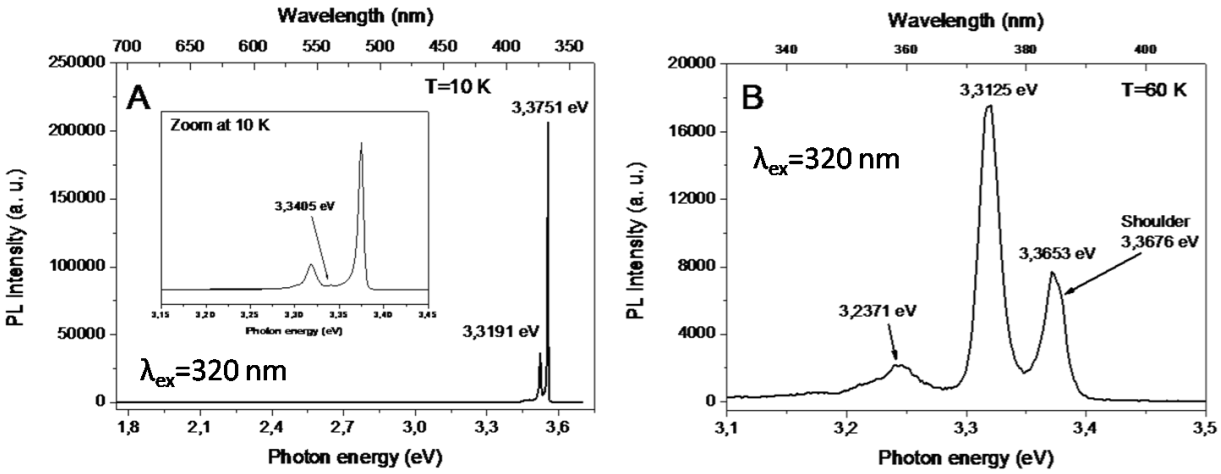

Figure IV-4. PL spectra of ZnO NCs obtained at 40 s residence time measured at 10 K (A) and 60 K (B).

The intensive and narrow lines of the near band edge emission region are observed at 3.3751 eV and 3.3191 eV for first and second lines at 10 K (Figure IV-4 A), respectively. The energy difference is equal to 56 meV which correspond to 451.7 cm^{-1}. A small peak is also visible at 3.3405 eV in UV region of the spectrum (inset of Figure 4 A). Figure IV-4 B shows UV region of PL spectrum measured at 60 K. A strong modification of the relative intensities between two first

peaks can be noted as: *I(3.3751 eV)/I(3.3191 eV)=5.67* and *I(3.3653 eV)/I(3.3125 eV)=0.44* for 10 K and 60 K, respectively

As the thermal quenching of the first line is drastic between 4 K and 10 K, the Figure IV-5-A demonstrates the thermal quenching of lines' intensities centered at 3.3751 eV and 3.3191 eV under a 325 nm excitation beam, on PL intensity when the equipment was regulated at 10 K, as a function of temperature deviation. Figure IV-5-B shows an intensity percentage loss for these maxima. As we can see, this evolution is quite linear. The slope of the straight line used to adjust these variations is equal to: -1.25 for the 3.3751 eV line (*tgα)* and -1.05 for the 3.3191 eV line (*tgβ*). Intensity of these two lines is strongly affected by temperature as about 5 % of the signal is lost with an increase of 3 K. Evolution of the intensities is similar which may indicate a link between these two lines.

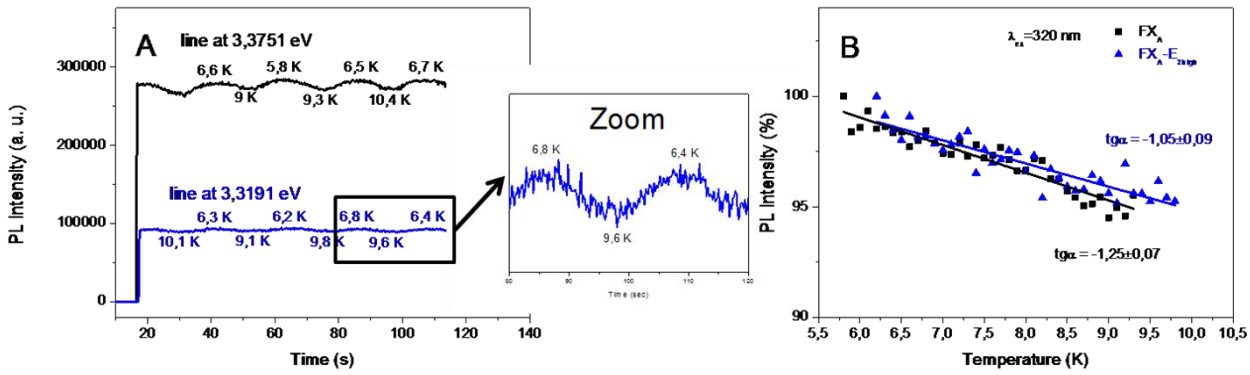

Figure IV-5. Low temperature PL kinetics of the lines at 10 K at 3.3751 eV and 3.3191 eV (A) and an intensity percentage loss for these lines (B).

In addition, when temperature increases the appearance of a shoulder at higher energy (3.3676 eV) is detected in the spectrum measured at 60 K. The intensity of the small and not well resolved band at 3.2371 eV is higher than at 10 K where this band is quenched, whereas the peak at 3.3125 eV becomes maximal in intensity. As PL measurements performed at room temperature, no PL emission in the visible domain of the spectra measured at low temperature was observed

confirming the lack of surface defects generally observed on such small size of ZnO nanostructures.

The emission peak of ZnO low temperature PL spectra located at 3.375-3.38 eV has already been reported in literature. This peak is traditionally attributed to the direct radiative electron-hole recombination called free excitonic recombination and labeled "FX". One can distinguish several types of free excitonic recombination (called as FX_A, FX_B, FX_C) depending on the energy of these free excitons (see Figure IV-6). The energy difference between FX_A and FX_B is generally equal to 7-10 meV, FX_A being the line at lower energy [12-15]. Liang and Yoffe [15] have observed a shoulder of FX_C centered at 3.4264 eV at 4.2 K on ZnO single crystals (0.1 μm size) grown by the vapor transport method.

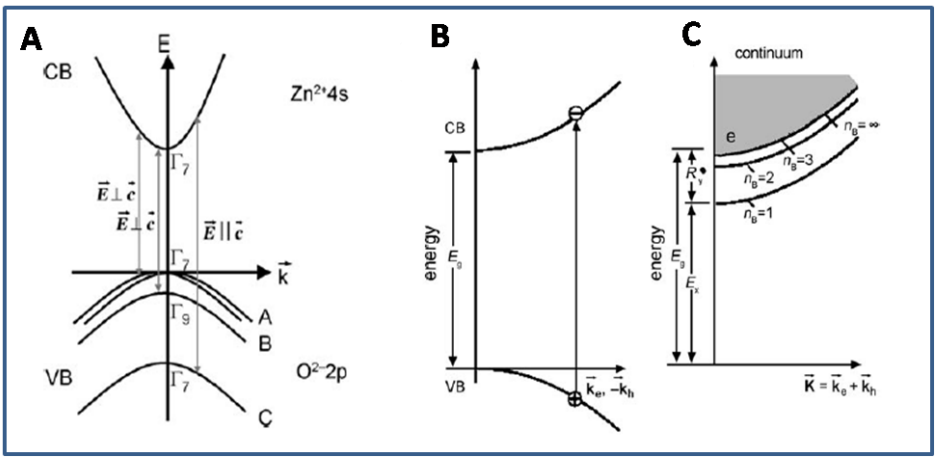

Figure IV-6. The electronic structure of ZnO (A), the schematic drown band-to-band transition (B) and the exciton states (C) [16].

Free excitonic emission FX_A was reported in literature for high quality ZnO monocrystals at 3.378 eV at 4.2 K [15]. FX_A is observed at 3.376 eV at 10 K for ZnO nanorods grown by metallorganic vapor phase epitaxy with diameter and aspect ratio in the range of 7-100 nm and 10-50 nm, respectively [17]. For ZnO nanorods and nanopencils obtained by thermal evaporation method, the length and diameter are equal to 10.23 μm and in the range of 230~340 nm,

respectively for nanorods, length and diameter were 1.9 μm and in the range of 35-55 nm, respectively for nanopencils, FX_A was observed at 3.380 eV for both morphologies [14]. FX_A emission was observed at 3.376 eV at 15 K [18] and at 3.376 eV at 10 K [13] for ZnO films grown by metallorganic vapor phase epitaxy. For ZnO film grown by laser-molecular-beam epitaxy FX_A emission was observed at 3.377 eV at the temperature of 5 K [12]. Thereby, literature survey shows that the smallest ZnO nanostructures which are exhibiting FX emission at low temperature are nanorods-like structures with size up to 100 nm. However, many reports [26-28] on ZnO nanowires, films and nanorods show that FX associated emission appears at temperature higher than 10 K after the depopulation of the traps which give lines peaking between 3.35-3.37 eV [16]. This type of near band edge emission usually gives very narrow peaks on low temperature PL spectra of ZnO. This emission is originated from the bounded excitons with ionized or neutral donors (D^+, D^0) or neutral acceptors (A^0) which form D^+X, D^0X and A^0X center. Their emissions were reported as intense PL peak at low temperature on ZnO single crystals at 3.3636 eV and 3.3614 eV [19], 3.367 eV [20], 3.3628 eV [21], 3.358-3.368 eV [22]; for ZnO films at 3.360 eV [23], 3.364 eV [24], for ZnO nanowires at 3.362 eV [25]. The origin of this donor/acceptor state is not clear in literature and whatever the synthetic route or the nature of the reactants, their associated emission is located in the same range of energy.

Thereby, in all the survey done, bound exciton emission in ZnO is situated at lower energy region than the two first lines observed in Figure IV-4. It is quite surprising to observe in our material, PL lines at energy values which correspond to free excitons but two explanations can be formulated: The first observed line at 10 K which is centered at 3.3751 eV can be attributed to FX_A excitonic recombination. A temperature increase at 60 K makes possible the observation of FX_B free excitons at 3.3676 eV, while FXA line is shifted to lower energy at 3.3653 eV due to temperature increase. One can imagine that the high crystallinity of ZnO NCs and their small dimension could avoid the local intrinsic punctual defects which can trap the electron-hole pair

required for the observation of bounded excitons at the expected 3.35-3.37 eV energy region. On the other hand, one can imagine that because of the small size of ZnO NCs, quantum effect occurs and results a shift of the bounded excitons to higher energy but generally quantum confinement strongly affect the optical properties and considerably shift the emission. We have discarded this last hypothesis. A deeper investigation behavior of these emission lines is needed to better understand the nature of the emissions.

As it was mentioned before, the energy difference between the peaks at 3.3751 eV and 3.3191 eV is equal to 56 meV (451 cm^{-1}) in the emission spectrum measured at 10 K. As it was shown in previous chapters, the Raman spectra of ZnO NCs exhibit the most intensive E_2 high nonpolar phonon mode at 436 cm^{-1} which is very close to obtained energy shift of 451 cm^{-1} (Figure IV-4). Thereby, the second line at 3.191 eV could be attributed to the vibronic transition resulting from the coupling of the radiative deexcitation line with E_2 high nonpolar phonons of ZnO NCs. It should be noted that, the interaction of free and bounded excitons with optical phonons of ZnO could have different character depending on the nature of the phonon.

The investigations of the optical phonons comparing with photoluminescence properties in ZnO have been provided by a number of groups [29-35]. ZnO with würtzite symmetry has 4 atoms per unit cell leading to 12 phonon modes among which 9 modes are optical ones. The zone-centered optical phonons can be classified according to the following representation: $\Gamma_{opt}=A_1+E_1+2E_2+2B_1$. The A_1 and E_1 optical modes are polar and both Raman and IR active. The two E_2 modes are nonpolar and Raman active only. The B_1 optical mode is inactive. Polarized right-angle Raman scattering of bulk ZnO was measured by Damen et al [29]. The frequencies for optical E_2, E_1(LO) and A_1(LO) modes were measured as 437 cm^{-1}, 583 cm^{-1} and 574 cm^{-1}, respectively. Arguello et al [30] obtained quite similar result in a variety of geometries in ZnO crystal. Calleja and Cardona [31] have studied the resonance of the high frequency optical modes – E_2-high, A_1(TO), E_1(TO)

and E_1(LO). Temperature dependence of Raman scattering study for E_2-high, A_1(LO) and E_1(LO) modes has been reported by Cuscó et al [32]. The interactions of free and bounded excitons with phonons in low temperature PL spectra of ZnO single crystals, nanorods and films are mostly attributed to the coupling of FX and bound excitons with A_1(LO) phonons. In most cases, the energy difference between FX or DX with their phonon replica in ZnO PL spectra reported in literature is equal to 72 meV (581 cm^{-1}). This energy corresponds to the coupling of free or bounded excitons with longitudinal phonons (LO) of A_1 and E_1 optical Raman modes [14, 22, 26-27, 33]. Jeong et al. [34] have really recently reported the broadening of linewidth of acceptor bound exciton line (A^0X) locating at 3.3581 eV at 13 K resulting of the E_2-high vibration phonon mode participating with A^0X line in ZnO crystals, for the first time.

According to Park et al. [35] taking into account the spin-orbit coupling, the conduction band belongs to the representation Γ_7 (we mark it Γ_7^c) and the valence band splits into 3 components A, B and C relating to representations Γ_9, Γ_7 and Γ_7 (we mark them Γ_9^v, Γ_7^c and Γ_7^c) respectively (Figure IV-7).

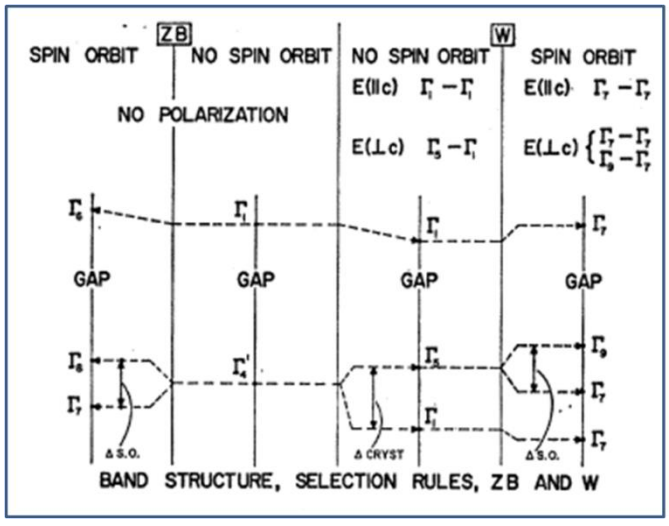

Figure IV-7. Band structure and selection rules for zinc blende and würtzite structures at the Γ symmetry point <k=0> [35].

In collaboration with Dr. Michel Couzi (ISM, Talence), we have studied the nature of the phonon mode and their potential coupling with the electronic transitions. The selection rules for the pure electronic transitions between conduction and valence zones are given by the direct products of representations of the initial state and the final state:

Band A: $\Gamma_9^v \otimes \Gamma_7^c = E_1 + E_2$, Band B and band C: $\Gamma_7^v \otimes \Gamma_7^c = A_1 + A_2 + E_1$

The active representations (polar) of the group C_{6v} are $A_1(z)$ and $E_1(x,y)$ in a way that in a monocrystal the band A is active in the polarization $E \perp c$ (E_1) and the bands B and C are active in two polarizations: $E \perp c$ (E_1) and $E \parallel c$ (A_1).The vibrational modes (phonons) of centre of crystal zone of ZnO (Wurtzite) distribute as: $\Gamma_{ph.}=A_1+2B_1+E_1+2E_2$. The modes A_1 and E_1 are active in both IR and Raman, the modes E_2 are active only in Raman and the modes B_1 are "silence" modes (inactive in both IR and Raman).The selection rules for the vibronic transition which involves one of electronic transitions A, B or C and a vibrational transition can be expressed as:

Band A:

Phonon A_1: $A_1^{ph.} \otimes \Gamma_9^v \otimes \Gamma_7^c = A_1^{ph.} \otimes (E_1 + E_2) = E_1 + E_2$ active $E \perp c$ (E_1)

Phonons B_1: $B_1^{ph.} \otimes \Gamma_9^v \otimes \Gamma_7^c = B_1^{ph.} \otimes (E_1 + E_2) = E_2 + E_1$ active $E \perp c$ (E_1)

Phonon E_1: $E_1^{ph.} \otimes \Gamma_9^v \otimes \Gamma_7^c = E_1^{ph.} \otimes (E_1 + E_2) = A_1 + A_2 + E_2 + B_1 + B_2 + E_1$

active $E \parallel c$ (A_1) et $E \perp c$ (E_1)

Phonons E_2: $E_2^{ph.} \otimes \Gamma_9^v \otimes \Gamma_7^c = E_2^{ph.} \otimes (E_1 + E_2) = B_1 + B_2 + E_1 + A_1 + A_2 + E_2$

active $E \parallel c$ (A_1) et $E \perp c$ (E_1)

Band B and band C:

Phonon A_1: $A_1^{ph.} \otimes \Gamma_7^v \otimes \Gamma_7^c = A_1^{ph.} \otimes (A_1 + A_2 + E_1) = A_1 + A_2 + E_1$ active $E \parallel c$ (A_1) et $E \perp c$ (E_1)

Phonons B_1: $B_1^{ph.} \otimes \Gamma_7^v \otimes \Gamma_7^c = B_1^{ph.} \otimes (A_1 + A_2 + E_1) = B_1 + B_2 + E_2$ inactive

Phonon E_1: $E_1^{ph.} \otimes \Gamma_7^v \otimes \Gamma_7^c = E_1^{ph.} \otimes (A_1 + A_2 + E_1) = 2E_1 + A_1 + A_2 + E_2$

activeE$\parallel$c (A_1) et E$\perp$c (E_1)

Phonons E_2: $E_2^{ph.} \otimes \Gamma_7^v \otimes \Gamma_7^c = E_2^{ph.} \otimes (A_1 + A_2 + E_1) = 2E_2 + B_1 + B_2 + E_1$ active E$\perp$c (E_1)

Thereby, the coupling between free excitons and E_2-high optical phonons is possible. PL spectrum of ZnO NCs measured at 10 K has been superposed with Raman shift on Figure IV-8.

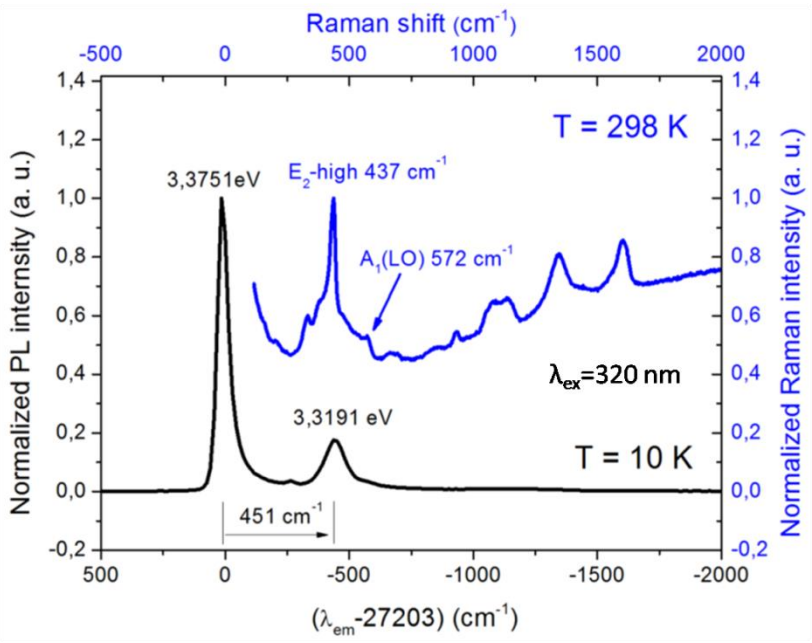

Figure IV-8. The superposition of PL spectrum measured at 10 K and room temperature Raman spectrum of ZnO NCs, both spectra are plotted in cm^{-1}.

One can clearly observed that the line at 3.3191 eV is perfectly matching with E_2-high frequency vibration in Raman spectrum. Thus, we can conclude that the origin of 3.3191 eV line results from a coupling of first emission line with E_2-high phonons.

As it was described in Chapter I, ZnO generally exhibits several types of emissions locating at different energies in UV region of its PL spectrum (Figure IV-9) [16]. As a reminder, the emission originated from free excitons is located at highest energy region at 3.7-3.9 eV. After free excitons the emissions from bounded excitons and deep centers could be observed locating at 3.35-3.37 eV and 3.34-3.35 eV, respectively.

In addition to FX and bounded excitons, some authors report the existence of lines between 3.32 eV and 3.34 eV [21, 36-37]. This emission is so-called two-electron satellite (TES) transitions (written as two-electron transistors on Figure IV-9). TES is originated from the radiative recombination of a neutral donor bound exciton (DX) to a neutral donor and excited free excitons. Therefore, TES emission could be observed only in the case of presence of neutral donor bound excitons emission.

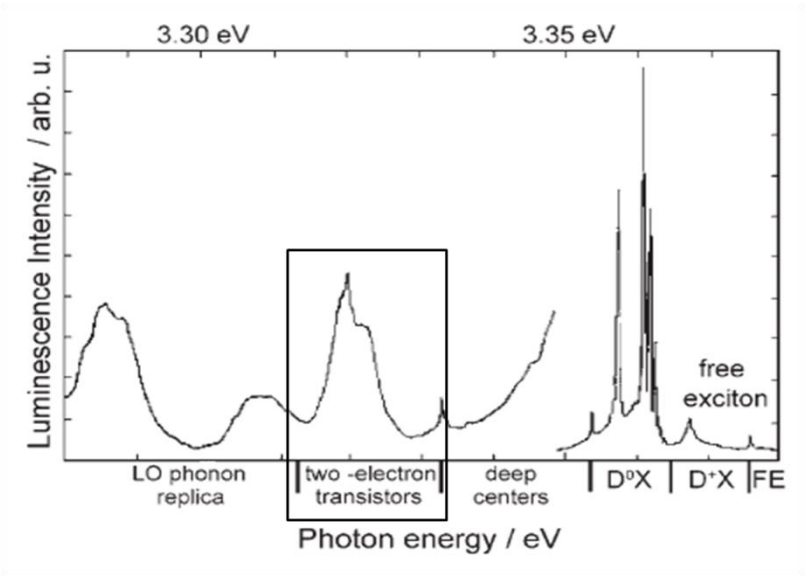

Figure IV-9. Low temperature (1.8 K) PL spectrum of a ZnO bulk sample in UV region [16].

TES radiative transitions is quite often process in a wide variety of semiconductors including direct band gap as GaAs [38], InP [39] and wide gap GaN [40]. In our case, a small peak at 3.3405 eV in PL spectrum at 10 K is located close to TES energy region (inset of Figure IV-4). But, on the other hand, no emission corresponding to the energy of a neutral donor bound excitons was observed on ZnO NCs spectra. In this case, the nature of 3.3405 eV small peak is still unknown.

Figure IV-4-B shows PL spectrum of ZnO NCs measured at 60 K. This spectrum demonstrates several changes in comparison with 10 K spectrum: (i) a new shoulder of the first line which is centered at 3.3653 eV appears at higher energy region (3.3676 eV) with increasing temperature as already commented. The energy difference between the two lines is equal to 2.3 meV, which is

smaller than the expected energy difference between FX and D^0X, (ii) the intensity of the first lines is strongly quenched in favor of E_2-high vibronic line and (iii) a new band at 3.2371 eV is observed. The energy difference between the first line and 3.2371 eV band is equal to 128.2 meV. As it was mentioned before, the coupling between FX, DX or AX lines and optical phonons in ZnO nanostructures is mostly attributed to longitudinal optical phonons (LO). The energy difference between these lines and LO is equal to ~72 meV corresponding to A_1(LO) and E_1(LO) Raman optical modes of ZnO. In our case, 128.2meV is approximately equal to 56 meV (E_2-high) plus 74 meV A_1(LO). This band centered at 3.2371 eV could be a two phonons assisted transition, and since 128.2 eV is approximately two times more than the E_2-high phonon value, we could attribute this band to second order interaction of the first line with E_2-high optical phonon mode. As the ZnO NCs are randomly distributed on the support with no specific orientation, the effect of polarization cannot be studied to close the first or the second hypothesis.

In collaboration with Dr. P. Martin (CELIA, Talence) who provides us a ZnO single crystal, additional luminescent measurements were performed at low temperature. The goal was to compare the exact position of the emission peaks in both materials, using a Hg lamp as an etalon. Figure IV-10 illustrates the emission graphs obtained at 17 K on the single crystals. We can observe well structured lines between 3.2 eV and 3.4 eV. A zoom in the visible range reveals a large band consistent with potential defect described on Chapter I. But the intensity of this band is really weak.

Figure IV-11 shows the superposition of the emission curves of the single crystal (red curve) and the NCs (black curve) at 23 K, 50 K and 100 K. At 23 K, the main emission observed on single crystal peaks at lower energy (3.3645 eV) than the NCs one's.

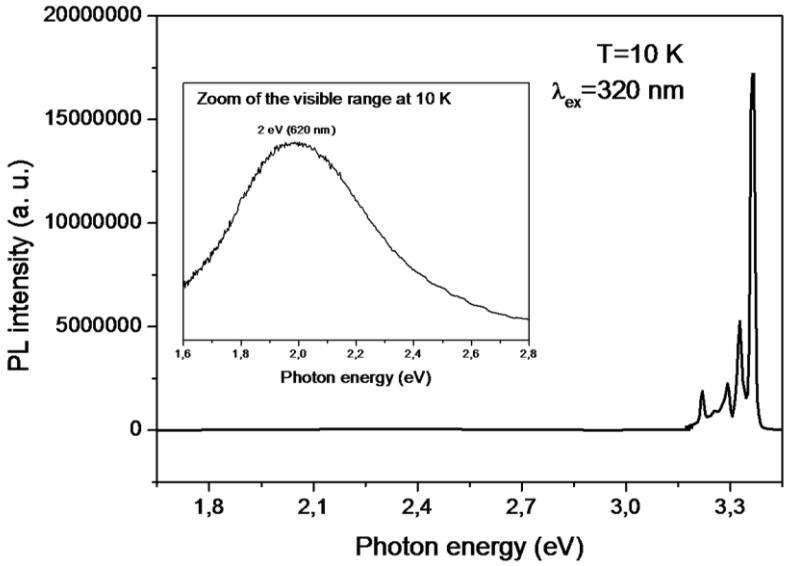

Figure IV-10. PL spectrum of ZnO single crystal (CELIA) measured at 10 K.

This corresponds to a bounded excitons emission. An additional weak contribution appears at higher energy (3.3792 eV) and can be attributed to FX excitons.

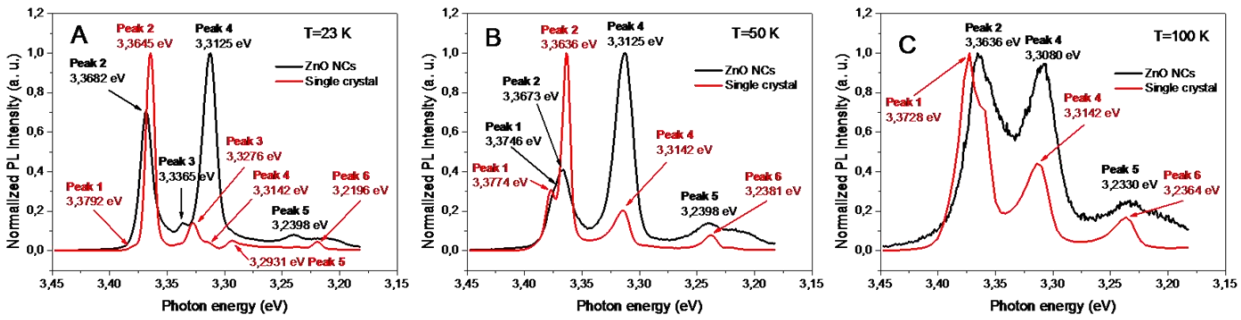

Figure IV-11. The superposition of PL spectra measured for ZnO NCs and ZnO single crystal at 23 K (B), 50 K (B) and 100 K (C), excitation wavelength is 320 nm.

Other small peaks are also detected at 3.3276 eV, 3.3142 eV, 3.2931 eV and 3.2196 eV at 23 K. But these lines don't peak at the same energy as the NCs' ones. At 50 K, contribution of the FX excitons is higher as well as the phonons replica intensity at 3.3142 eV, whereas the main peak decreases as expected when considering a thermal depopulation of the trap. The energy differences between the lines are reported in Table IV-1 for both materials. Because, the energy difference in ZnO single crystal spectra between lines (in table IV-1 the distance between Peak 2 and Peaks 5

and 6) is approximately equal to 72 meV and 150 meV at 23 K, these last two peaks can be attributed to D^0-A_1(LO) and $2D^0$-A_1(LO). As temperature reaches 50 K, emission curves of crystal is quite similar to that of NCs at 23 K or lower temperature but with a weaker electron-phonon coupling.

Table IV-1. Energy differences between the lines in PL spectra of ZnO NCs and single crystal measured at 23 K, 50 K and 100 K.

ZnO nanocrystals							
T, K		Peak 1	Peak 2	Peak 3	Peak 4	Peak 5	Peak 6
23	Peak 1	0					
	Peak 2	-	0				
	Peak 3	-	31.7	0			
	Peak 4	-	55.7	24	0		
	Peak 5	-	128.4	96.7	72.7	0	
	Peak 6	-	-	-	-	-	0
50	Peak 1	0					
	Peak 2	7.3	0				
	Peak 3	-	-	0			
	Peak 4	62.1	54.8	-	0		
	Peak 5	134.8	127.5	-	72.7	0	
	Peak 6	-	-	-	-	-	0
100	Peak 1	0					
	Peak 2	-	0				
	Peak 3	-	-	0			
	Peak 4	-	55.6	-	0		
	Peak 5	-	130.6	-	75	0	
	Peak 6	-	-	-	-	-	0
ZnO single crystal							
T, K		Peak 1	Peak 2	Peak 3	Peak 4	Peak 5	Peak 6
23	Peak 1	0					
	Peak 2	14.7	0				
	Peak 3	51.6	37.1	0			
	Peak 4	65	50.3	13.4	0		
	Peak 5	86.1	71.4	34.5	21.1	0	
	Peak 6	159.6	144.9	108	94.6	73.5	0
50	Peak 1	0					
	Peak 2	13.8	0				
	Peak 3	-	-	0			
	Peak 4	63.2	49.4	-	0		
	Peak 5	-	-	-	-	0	
	Peak 6	139.3	125.5	-	76.1	-	0
100	Peak 1	0					
	Peak 2	-	0				
	Peak 3	-	-	0			
	Peak 4	58.6	-	-	0		
	Peak 5	-	-	-	-	0	
	Peak 6	136.4	-	-	77.8	-	0

Table IV-2 lists the ratio of the highest energy lines FX (peak 1) and D^0X (peak 2) over the first vibronic line at about 3.3142 eV and 3.2381 eV (50 K, single crystal).

Table IV-2. The intensity ratio of FX and D^0X associated lined over the vibronic lines in ZnO NCs and single crystal PL spectra measured at 23 K, 50 K and 100 K.

	ZnO nanocrystals		ZnO single crystal			
	FX/replica		FX/replica		D^0X/replica	
T(K)	I_{peak2}/I_{peak4}	I_{peak2}/I_{peak5}	I_{peak1}/I_{peak4}	I_{peak1}/I_{peak6}	I_{peak2}/I_{peak4}	I_{peak2}/I_{peak6}
23	0.7	8.75	-	-	7.14	22.7
50	0.41	2.92	1.55	3.97	5	12.8
100	1.06	4	2.27	5.6	-	-

The intensities of the vibronic lines are much intense in NCs than in the single crystal. Regarding the single crystal luminescence, this coupling is less efficient and the ratio is superior to 1. We can imagine that when the D^0X trap level is thermally depopulated in favor of the FX levels, the coupling between FX electron hole-pair radiative recombination and the phonons becomes more efficient.

Taking into account the spectral distribution of the emission in the single crystals and the NCs, we can definitively discard the existence of bounded excitons in the studied nanoparticles. In all ZnO nanostructures investigated in literature, FX_A and FX_B free excitons lines are always observed at 2-13 meV above the bounded excitons lines when temperature increasing [12-14, 22, 36, 41-42]. Thereby, the difference of 7.3 meV observed at 50 Kin our ZnO NCs between the first line and its shoulder clearly fits with the energy difference between FX_A and FX_B. In addition, similarity observed between the 50 K emission curve of single crystal and the lower temperature emission spectra of NCs seems to confirm that the attribution of the observed lines in the 3.368-3.378 eV range as FX_A and FX_B free excitonic emission is correct. Thereby, the lines located at 3.3676 eV,

3.3653 eV, 3.3125 eV and 3.2371 eV in 60 K spectrum could be attributed to FX_B, FX_A, $1E_{2high}$-$FX_{A,B}$ and $1E_{2high}$, A_1LO-$FX_{A,B}$ or $2E_{2high}$-$FX_{A,B}$,respectively.

For a definitive attribution of the origin of the two observed main lines at 3.3751 eV and 3.3191 eV, the global temperature dependence of the emission was performed for ZnO NCs. Figure IV-12 shows PL spectra in the region of the band edge emission measured at the temperatures from 10 K to 90 K. As it was expected, the intensities of all peaks are strongly affected by temperature. The shoulder of the first line which is situated at higher energy can be distinguished approximately at 50 K and no addition line appears at higher energy.

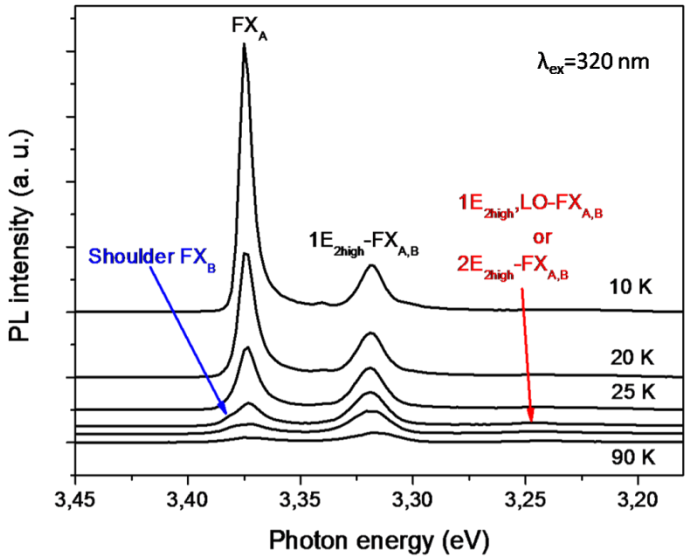

Figure IV-12. PL spectra of ZnO NCs measured from 10 K to 90 K (all data are shifted in the vertical direction for clarity).

To complete the temperature evolution of PL spectra, Figure IV-13 shows normalized spectra measured from 10 K up to room temperature. FX_A and FX_B emissions shift to the lower energy region with increasing temperature. The existence of FX_A and FX_B emission at the high temperature region also confirms the free excitonic nature of these emissions, because neutral

donor and acceptor bounded excitonic emission in ZnO is quenched at the temperature above 150 K [13-14, 16-17, 22, 26-27]. $1E_{2high}$-$FX_{A,B}$ emission line is also shifted to the lower energy region of the spectra with increasing temperature. Finally, FX_A, FX_B and $1E_{2high}$-$FX_{A,B}$ form one unstructured PL emission band at the room temperature with a maximum at 377 nm confirming the free excitonic nature of PL emission observed for room temperature PL spectra of ZnO NCs.

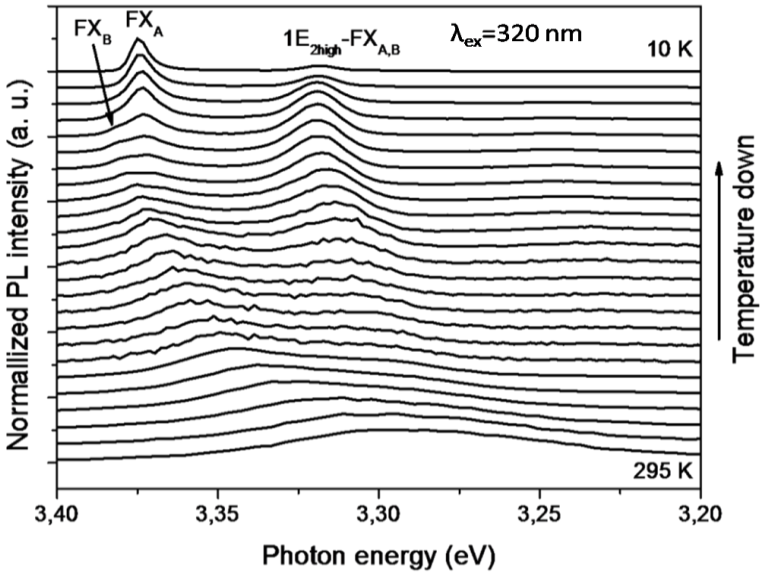

Figure IV-13. Normalized PL spectra of ZnO NCs measured at temperatures from 10 K to 295 K.

These additional analyses have revealed that all spectra can be fitted by four/five Gaussian peaks corresponding to FX_A, FX_B, $1E_{2high}$-$FX_{A,B}$, $1E_{2high}$-A_1LO-$FX_{A,B}$ or $2E_{2high}$-$FX_{A,B}$and a last contribution which correspond to the unidentified peak pointed at 3.22 eV at 70 K (Figure IV-14-A).

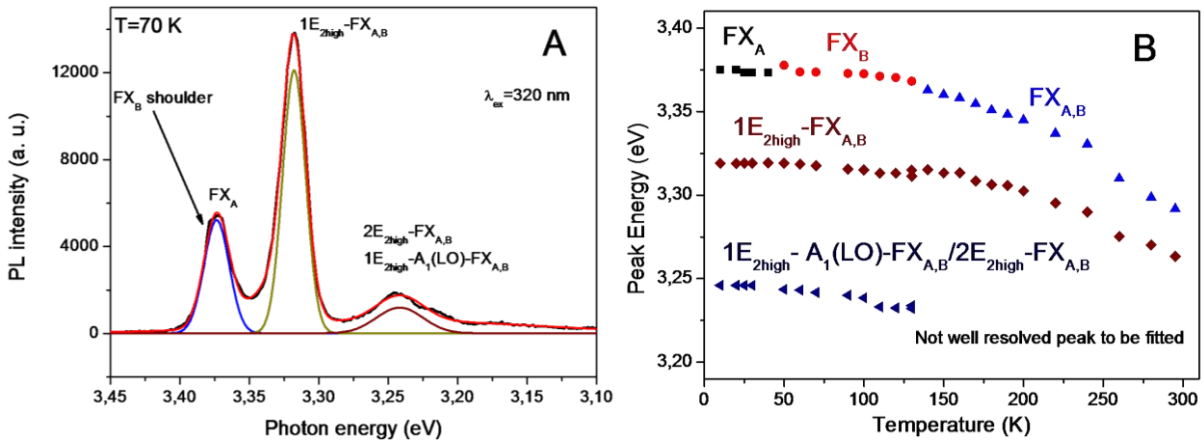

Figure IV-14. Typical Gaussian fitting analysis of the PL spectrum measured at 70 K (A), the temperature dependent peak position of $FX_{A,B}$, $1E_{2high}$-$FX_{A,B}$ and $1E_{2high}$-A_1(LO)-$FX_{A,B}$ or $2E_{2high}$-$FX_{A,B}$ emissions of ZnO NCs (B).

Figure IV-14-B shows the $FX_{A,B}$, $1E_2$-$FX_{A,B}$ and $1E_{2high}$-A_1LO-$FX_{A,B}$ or $2E_{2high}$-$FX_{A,B}$peak position dynamics as a function of temperature. The last contribution of$1E_{2high}$-A_1LO-$FX_{A,B}$ or $2E_{2high}$-$FX_{A,B}$emission could not be fitted well due to poor resolution of this band. However, $FX_{A,B}$ and $1E_2$-$FX_{A,B}$ emissions are fitted for all temperature region. The peak position remains really unchanged up to 100 K. From this temperature both emissions demonstrate the same dynamic – both emission lines are shifted to lower energy region. $FX_{A,B}$ line is shifted by 78.8 meV with increasing temperature from 10 K up to 295 K, while $1E_{2high}$-$FX_{A,B}$ line shifts by 55.8 meV at the same temperature range corresponding to the coupling of free excitons with E_2-high Raman mode in ZnO NCs.

As it was previously discussed, FX emission corresponds to the recombination of free excitons thereby; this emission peak dynamic should follow the Varshni formula (eq. 1) due to the temperature induced lattice dilatation and electron-lattice interaction. Gap energy shift can be calculated as followed:

$$E_g(T) = E_g(0) - \frac{\alpha T^2}{T + \beta} \qquad \text{(eq. 1)}$$

where $E_g(T)$ is the band gap at an absolute temperature T; $E_g(0)$ is the band gap at 0 K; α and β are the Varshni thermal coefficients related with given materials [43].

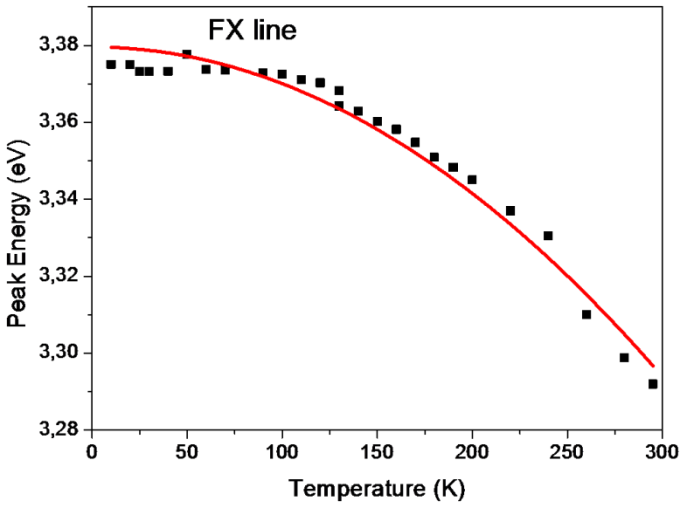

Figure IV-15. The fitting of $FX_{A,B}$ emission by the Varshni formula.

Figure IV-15 demonstrates the fitted results by Equation (1) for the FX emission line at the temperatures from 10 K to 295 K. The obtained fitting parameters of $E_g(0)$, α and β are 3.386 eV, $4.2 \cdot 10^{-5}$ eV/K and 704 K, respectively. These parameters are similar to the values previously reported for ZnO films [44], ZnO nanoneedle arrays [45] and for ZnO nanowires/nanowall [46] (Table IV-3).

Table IV-3.The parameters of Varshni formula of ZnO NCs in comparison with literature data.

	Eg(0), eV	α, eV/K	β, K
ZnO NCs (this work)	3.386	$4.2 \cdot 10^{-5}$	704
[44], ZnO film	3.3772	$7.2 \cdot 10^{-4}$	1077
[45], ZnOnanoneedle/nanorods	3,379	$7,5 \cdot 10^{-4}$	1050
[46], ZnO nanowire/nanowall	-	$4,9 \cdot 10^{-4}$	900

III. Low temperature photoluminescence properties of "ZnO_2" type NCs.

As it was mentioned before, room temperature PL spectra of the sample obtained at 6 s residence time corresponding to intermediate ZnO_2 nanoparticles with ZnO nuclei (Chapter III) exhibit UV emission line at 377 nm which is the same as in the case of ZnO NCs sample obtained at 40 s residence time. To confirm the absence of PL emission originated form ZnO_2 phase, low temperature PL spectra were measured for 6 s residence time sample. Figure IV-16 shows the superposed normalized spectra measured in the same conditions of excitation and emission slits to guarantee a valid comparison of the full width at half maximum of the samples obtained with a residence time of 6 s and 40 s.

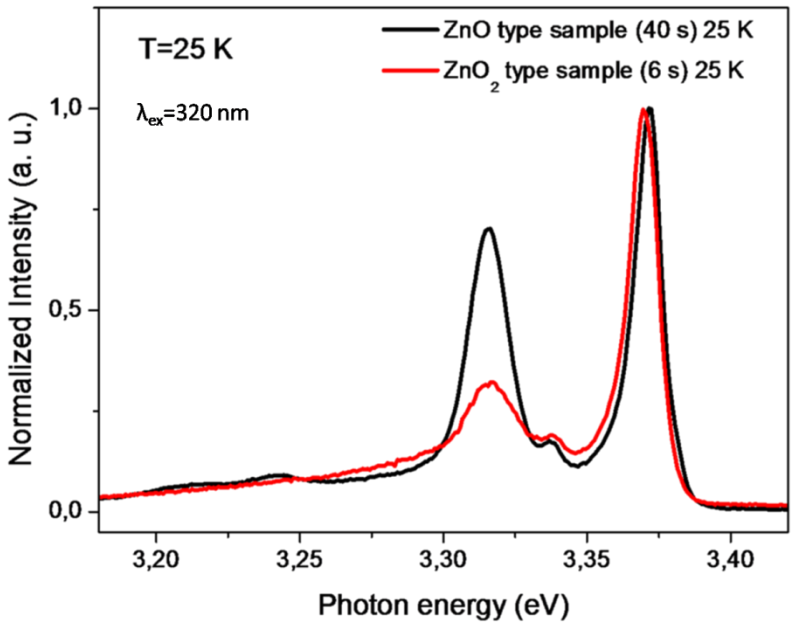

Figure IV-16. The superposition of PL spectra measured for the samples obtained at 6 s and 40 s residence times at temperature of 25 K.

As it can be seen for the spectra, the relative intensities of $1E_{2high}$-$FX_{A,B}$ line of 6 s and 40 s residence time samples are different and correspond to ratio $I_{max}(40s)/I_{max}(6s)$ equal to 2.3. Such difference shows that the exciton-phonon coupling is less effective in the case of 6 s residence

time sample because of smaller size and crystallinity of these nanoparticles. As it was discussed in Paragraph II, the emission of 6 s residence time sample is originated from ZnO nuclei while the emission from ZnO_2 phase is not detected. For remaining the corresponding XRD patterns only show characteristic diffraction peaks from ZnO_2 particles. As expected, low temperature PL spectrum of the sample obtained at 6 s residence time also exhibits emission lines originated from ZnO nuclei.

IV. Decay time measurements

Decay time dynamics of free and bounded excitons features in ZnO single crystals and different nanostructures have been investigated by a number of groups to attribute the emission line [36, 47-57]. However, in the literature, there is a large dispersion of measured decay time values for ZnO single crystals and nanostructures. The recombination decay time of free excitons in ZnO single crystals at low temperature have been observed as biexponential decay by Teke at al. [36] equal to 286.8 ps and 1000 ps for fast and slow decay, respectively. The authors attributed the fast decay constant to the effective nonradiative recombination and slow decay component to the radiative free excitons recombination lifetime. Reynolds et al. [47] have reported the shorter single-exponential radiative recombination decay of the free excitons – 322 ps at 2 K for ZnO single crystals. Koida et al. [48] have measured decay time for ZnO single crystal and epitaxial films, all ZnO films show a single exponential decay in the range of 0.036-0.11 ns, while the single crystal demonstrates biexponential behavior with a fast decay value of 0.97 ns and a slower decay of 14 ns. In this case, the fast decay constant was attributed to the recombination lifetime of free excitons and slow constant to free carrier decay including trapping and emission processes.

Decay time dynamic of the recombination lifetime of free and bounded excitons have also been reported for ZnO nanostructures [49-57]. Xing et al. [49] have reported decay time measurements for well-aligned ZnO nanowire arrays at 10 K; the observed biexponential decay shows two components equal to be 49.5 ps and 382.7 ps for fast and slow component, respectively. The authors attributed the fast component to bounded excitons recombination lifetime, while slow component is attributed to the free excitonic recombination. The biexponential decay time of ZnO nanorods at 1.9 K has been reported by Zhao et al. [50]. It was demonstrated that ZnO nanorods exhibit a very fast (a few tens of ps) decay. They have also demonstrated that the fast component of decay time which is attributed to the surface recombination of free excitons decreases with decreasing the diameter of nanorods. The very short radiative single exponential decay time (65 ps) of free excitonic recombination was observed in ZnO quantum dots [51].

The study of decay time dynamic of donor bounded excitons (D^0X) in ZnO nanowires has been reported by Reparaz et al. [52]; observed decay time of D^0X varies from 67 ps to 200 ps. Kwok et al. [53] have reported longer biexponential decay time of D^0X for ZnO rods equally to 116 ps and 1.2 ns for fast and slow component of decay, respectively. The same group has measured decay time of different ZnO nanostructures [54]. They reported that different types of ZnO nanostructures could have very different decay times with biexponential decay, e.g., ZnO nanorods and shells show very fast decay – 7 ps and 44 ps and 10 ps and 37 ps, respectively, while tetrapods exhibit comparatively slow decay time – 91 ps and 708 ps. Sun et al. [55] have also observed a very small biexponential lifetime of D^0X in ZnO nanopillars equally to 15 ps and 58 ps at 5 K. However, Chen et al. [56] has observed a much longer biexponential decay time of D^0X emission at 5 K in bulk ZnO from 0.20 ns to 0.26 ns and from 0.75 ns to 1.1 ns for fast and slow constant, respectively.

Decay time measurements were carried out for ZnO NCs sample, which exhibits two populations of morphology (nanospheres and nanorods)in collaboration with Dr. P. Martin (CELIA). Decay time signal for only spherical ZnO NCs sample have not been detected due to small size of these NCs (discussion will be provided below).

Figure IV-17 shows typical PL decay dynamics of 369 nm emission peak for the PL spectrum of ZnO NCs performed at 10 K. Figure IV-17-A demonstrates decay dynamic at VUV excitation energy corresponding to the absorption on ZnO NCs surface. The decay time curve fits well to a biexponential decay function with a fast component τ_1 and slow component τ_2. By a least-square fitting, τ_1 and τ_2 are 83.8 ps and 527.3 ps, respectively. Decay time dynamic with the absorption near the surface of ZnO NCs at UV excitation energy is shown on the Figure IV-17-B.

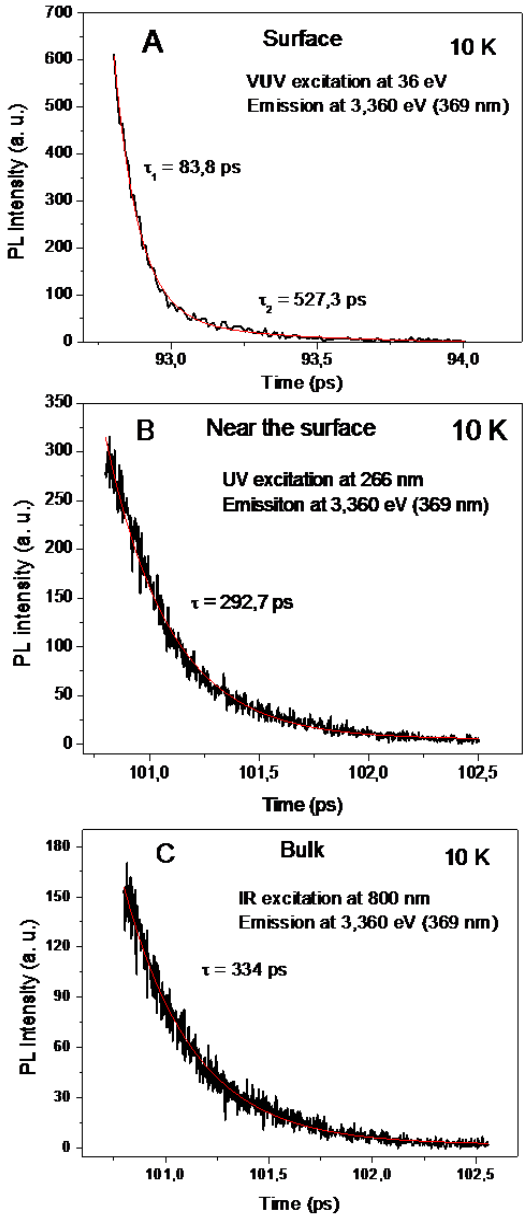

Figure IV-17. Decay time kinetics of 369 nm emission of ZnO NCs at 10 K under VUV (A), UV (B) and IR (C).

In this case (B decay curve), decay time dynamic curve could be fitted by monoexponential decay function with 292.7 ps decay value. Decay time value equally to 334 ps has been obtained with IR excitation energy corresponding to the absorption in the bulk region of ZnO NCs (Figure 17-C).

Decay time signal for the sample with only spherical ZnO NCs morphology is not detected because of experimental set-up characteristics. It should be noted that for the start-stop system of decay

time measurements the maximal PMT resolution which can be measured is approximately of 50 ps FWHM. Thereby, the smallest decay time which could be measured is about 100 ps. Yamamoto et al. [57] have studied colloidal ZnO nanocrystals size dependence of the decay time dynamics. It was demonstrated that the lifetime is increasing with particle size diameter as D^3. Decay time is less than 100 ps for ZnO NCs with size smallest than 3 nm. Thereby, in our case, small spherical ZnO NCs could also have decay time value faster than 100 ps. Therefore, decay time signal could not be detected for small spherical ZnO NCs by experimental equipment which was used in this work.

In the previous paragraph, all emission lines in low temperature PL spectrum of ZnO NCs have been attributed to free excitonic emission and the exciton-phonon coupling. However, as it shown before, the big dispersion of decay time parameters for free and bounded excitons in ZnO single crystals and nanostructures in literature makes it difficult to understand the nature of observed decay time parameters in this work. However, except for the VUV excitation for which two components are necessary to fit the curve, the UV and IR excitations converge to a unique 300 ps decay time in a good agreement with values obtained in ref. [39, 47, 59] for a free excitonic radiative recombination. One can imagine that because of the high absorption coefficient and the short component observed for the VUV excitation, the decay curve reflects the energy transfer from the ZnO_2-like surface to the ZnO nanocrystal. Therefore, for deeper understanding of the decay time behavior of ZnO NCs obtained by supercritical fluids approach, further decay time investigations are needed.

Conclusion:

As it was discussed before, low temperature PL spectra of ZnO exhibit several emissions originated from free and bounded excitons and their associated emissions from phonon coupling and TES. Table IV-4 summarizes literature survey for PL emissions of ZnO measured at low temperature.

Table IV-4.Peak positions of ZnO nanorods, nanowires, films and single crystals in their near band edge PL spectra measured at low temperature (from literature).

ZnO shape	Ref.	Nature of PL emission							
		FX_C	FX_B	FX_A	D^0X	A^0X	TES	LO-DX	LO-FX
Nanorods	14		3.388	3.380	3.363				3.310
	17			3.376	3.364 3.360 3.359				
	28			3.377	3.351		3.326		
Nanowires	26				3.3737 3.3693 3.3645				
	46			3.366	3.3557 3.3586 3.3598				
	49			3.370	3.363 3.360				
	52			3.375	3.365				
Films	18			3.38	3.365	3.336		3.29 3.22 3.266 3.192	3.29
	23				3.360				
	24				3.364				
	12		3.384	3.377					3.25
	13		3.386	3.376	3.376 3.367 3.364 3.360 3.332		3.322		
	27				3.403 3.391 3.387				
	44			3.391	3.366				
Single crystal	56				3.357		3.32		
	22			3.378	3.358 3.361 3.362 3.364 3.365 3.368				
	41	3.4335	3.3938	3.3773					
	42	3.4214	3.3830	3.4214					
	19			3.3772	3.3636 3.3614 3.3570		3.3220 3.3189 3.3137 3.3058		
	15		3.378	3.386					

Energy range of these lines are reported on the Figure IV-18 and compared with the emissions observed in our samples at low temperature.

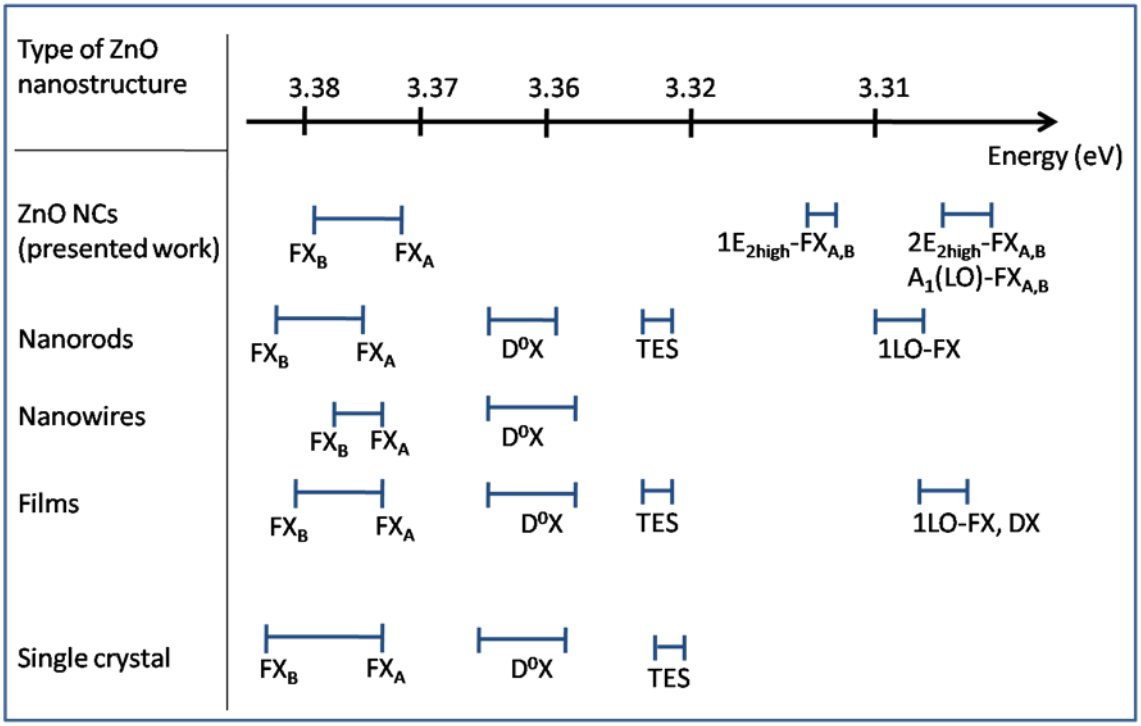

Figure IV-18. Scheme of the energy range of the emissions originated from different types of features in ZnO compared with these observed in our samples

In conclusion, low temperature PL measurements show that ZnO NCs prepared via supercritical fluids method exhibit a unique emission in UV region and no emission associated with defects was observed in the visible range. This emission was attributed to the recombination of free excitons (FX_A, FX_B) and their coupling with the first order E_{2high} optical phonon modes of ZnO ($1E_{2high}$-$FX_{A,B}$ and E_{2high}+A_1(LO)-$FX_{A,B}$) and/or second order $2E_{2high}$-$FX_{A,B}$ coupling. No emission which could be associated with bounded excitons with different types of donors and acceptors was observed as it usually takes place in ZnO materials. Low temperature PL spectra of "ZnO_2" type sample have the same spectral distribution as those measured for ZnO NCs due to the emission coming from ZnO nucleus but a lower phonon coupling is observed. The temperature evolution of

PL spectra was also provided. These measurements shows that the 10 K lines become one unstructured emission at room temperature as observed in literature. Deeper investigations are required to understand the decay time measurements and the influence of the surface states of the electron-hole recombination leading to the UV emission. The 300 ps value calculated from the decay time curve under UV and IR irradiation seems also to confirm the free excitonic nature of the lines observed at 10 K.

All the observations confirm the unique optical behavior of such small ZnO NCs, which optical properties are strongly linked to the synthetic route. They also show the high influence of the ZnO_2 phase as a precursor to precipitate a würtzite defects-free bulk and avoid the creation of the surface defects from which a visible emission is generally observed at this scale. All the optical measurements illustrate the high purity and crystalline quality of ZnO NCs obtained through the supercritical fluids route in this investigation.

References:

1. Y. Roig et al. Angew. Chem., Int. Ed., 2011, 50, 12071.
2. W. Chen et al. J. Phys. Chem. C, 2009, 113, 1320.
3. A. L. Companion, J. Phys. Chem. Solids, 1962, 23, 1685.
4. C.-C. Hsu et al. J. Photochem. Photobiol. A: Chem., 2005, 172, 269.
5. S. Lindroos et al. Inorg. Mater., 2000, 2, 197.
6. T. H. Guo et al. Mater. Lett., 2011, 65, 639.
7. H. Bai, X. Liu, Mater. Lett., 2010, 64, 341.
8. G. Feng et al. Particuology, 2012, 10, 388.
9. K-A. Kim et al. Bull. Korean Chem. Soc., 2014, 35, 431.
10. N. Kiomarsipour et al. Ceramic Inter., 2014, 40, 11261.
11. N. Izu et al. Ceramic Inter., 2014, 40, 8775.
12. T. Makino et al. Appl. Phys. Lett., 2000, 76, 3549.
13. S. W. Jung et al. Appl. Phys. Lett., 2002, 80, 1924.
14. C. H. Ahn et al. Appl. Phys. Lett., 2009, 94, 261904.
15. W. Y. Liang et al. Phys. Rev. Lett., 1968, 20, 59.
16. C. Klingshirn, ChemPhysChem, 2007, 8, 782.
17. W. I. Park et al. Appl. Phys. Lett., 2003, 82, 964.
18. W. I. Park et al. J. Mater. Res., 2001, 16, 1358.
19. D. C. Reynolds et al. Phys. Rev. B, 1998, 57, 12151.
20. D. C. Reynolds et al. Phys. Rev. 1965, 140, A1726.
21. B. K. Meyer et al. Phys. Status Solidi B, 2004, 241, 231.
22. D. W. Hamby et al. J. Appl. Phys., 2003, 93, 3214.
23. W. I. Park et al. J. Electr. Mater., 2001, 30, L32.

24. W. I. Park et al. J. Appl. Phys. Lett., 2001, 79, 2022.

25. L. M. Li et al. Nanotechnology, 2007, 18, 225504.

26. V. Kharanovskyy et al. Nanotechnology, 2013, 24, 215202.

27. M. A. Borysiewicz et al. J. Lumin., 2014, 147, 361.

28. R. Zhang et al. Solid State Sci., 2009, 11, 856.

29. T. C. Damen et al. B. Tell, Phys. Rev., 1966, 142, 570.

30. C. A. Arguello et al. Phys. Rev., 1969, 181, 1351.

31. J. M. Calleja et al. Phys. Rev. B, 1977, 16, 3753.

32. R. Ciscó et al. Phys. Rev. B, 2007, 75, 165202.

33. R. Hauschild et al. Phys. Status Solidi C-Conference, 2006, 3-4, 976.

34. T. S. Jeong et al. J. Appl. Phys., 2014, 115, 053521.

35. Y. S. Park et al. Phys. Rev., 1966, 143, 512.

36. A. Teke et al. Phys. Rev. B, 2004, 70, 195207.

37. X. H. Wang et al. Appl. Phys. Lett., 2013, 102, 181909.

38. F. A. J. M. Driessen et al. J. Appl. Phys. 1991, 69, 906.

39. P. J. Dean et al. J. Appl. Phys., 1983, 54, 346.

40. P. P. Paskov et al. Phys. Status Solidi C, 2007, 4, 2601.

41. D. C. Reynolds et al. Phys. Rev. B, 1999, 60, 2340.

42. S. F. Chichibu et al. J. Appl. Phys., 2003. 93, 756.

43. Y. P. Varshni, Physica, 1967, 34, 149.

44. H. J. Ko et al. Appl. Phys. Lett., 2000, 76, 1905.

45. B. Cao et al. Appl. Phys. Lett., 2006, 88, 161101.

46. J. Grabowska et al. Phys. Rev. B, 2005, 71, 115439.

47. D. C. Reynolds et al. J. Appl. Phys., 2000, 88, 2152.

48. T. Koida et al. Appl. Phys. Lett., 2003, 82, 532.

49. C. Z. Xing et al. Chem. Phys. Lett., 2011, 515, 132.

50. Q. X. Zhao et al. J. Appl. Phys., 2008, 104, 073526.

51. X. H. Zhang et al. Appl. Phys. Lett., 2006, 88, 221903.

52. J. S. Reparaz et al. Appl. Phys. Lett., 2010, 96, 053105.

53. W. M. Kwok et al. Chem. Phys. Lett., 2005, 412, 141.

54. W. M. Kwok et al. Appl. Phys. Lett., 2005, 87, 223111.

55. J. M. Sun et al. J. Lumin., 2012, 132, 122.

56. S. L. Chen et al. Appl. Phys. Lett., 2013, 102, 121103.

57. S. Yamamoto et al. J. Lumin., 2007, 126, 257.

General conclusion

In this thesis, we investigated the synthesis of ZnO nanocrystals using a supercritical fluids approach and their optical properties.

The first objective as a scaling from micro- up to millireactor dimension of our continuous supercritical fluids based set up in order to produce a larger quantity of ZnO NCs (up to a gram scale per day) has been successfully provided. Whatever the experimental reactor, ZnO NCs exhibit an UV emission line and no visible photoluminescence was detected.

The second objective of this thesis as a deep characterization of ZnO NCs properties has been focused on NCs obtained with millireactor. In these conditions, due to a larger quantity of the powder available, the additional characterization techniques were performed. XRD patterns confirm the würtzite type-structure of the nanocrystals. FTIR, XPS spectroscopies and TG analysis show the existence of organics (with the average organics quantity of 6 wt.%) such as –OH, -CH_2, COO-, C-O, C=O and P=O which are originated from TOP and the traces of acetylacetonate from the precursor, at the surface.

The third objective was devoted to ZnO NCs size and morphology control. These can be controlled through the changing of two operating parameters of the process: the hydrodynamic regime and the H_2O_2 concentration. The hydrodynamic regime has a strong influence of TOP concentration into reactors which leads changing ZnO NCs morphology from small spherical NCs (at low TOP concentration) to bigger triangular and rods-like shaped NCs (at higher TOP concentration). The concentration of H_2O_2 also demonstrates a strong influence on ZnO NCs size and morphology. It was observed that very small and highly uniform spherical ZnO NCs are formed with high H_2O_2 concentration, while ZnO NCs size and morphology start to be not so uniform and contain some populations of triangular and hexagonal ZnO NCs with the decrease of H_2O_2 concentration. This

morphology behavior could be explained using homogeneous nucleation theory and LaMer diagram.

The fourth objective of this Ph.D. thesis has been devoted to the evaluation of ZnO NCs formation mechanism in a supercritical fluids based approach. We have demonstrated that the formation of ZnO NCs in our continuous supercritical fluids method goes through ZnO_2 intermediate phase. The following growth of ZnO NCs could be realized through the thermal decomposition of ZnO_2 intermediate nanoparticles forming final ZnO NCs with specific "ZnO_2"-like surface state. This "ZnO_2"-like surface states block/neutralize surface defects from which visible emission can occur. We cannot discard the fact that this ZnO_2 intermediate also favor the precipitation of stoichiometric ZnO nanocrystals which avoids the stabilization of punctual bulk defects such as oxygen vacancies. This is confirmed by the fact that emission spectra of ZnO NCs obtained without using H_2O_2 exhibits strong and intensive defect emission because in this case, it is impossible to construct such "ZnO_2"-like surface and quench surface defects.

The last objective of this thesis has been focused on a comprehensive investigation of ZnO NCs optical properties. Low temperature PL measurements were necessary to understand the nature of the excitonic emission lines. At low temperature, ZnO NCs exhibit several lines between 3.4 and 3.2 eV 3.4 and 3.2 eV. The positions of these lines were carefully calibrated using Hg lamp and compare to those observed in literature on several type of particles (nano- and macroscale). Additional measurements were performed on a single crystal provide by Dr. Patrick Martin (CELIA, Talence). Taking in to account the small size and high crystalline quality of NCs and considering, the energy position of the lines and their thermal behavior, we have rejected the possibility to observed trapped exciton luminescence as D^0X lines. These emission lines were attributed to the recombination of free excitons (FX_A, FX_B), their coupling with the first order E_{2high} and $E_{2high}+A_1(LO)$ optical phonon modes of ZnO ($1E_{2high}$-$FX_{A,B}$ and $E_{2high}+A_1(LO)$-$FX_{A,B}$)

and/or second order $2E_{2high}$-$FX_{A,B}$ coupling. The role of the ZnO_2 like surface state in the neutralization of the surface defect emission was also revealed after a heat treatment which decomposed this species and made possible the observation of a visible luminescence. The 300 ps value calculated from the decay time curve under UV and IR irradiation seems also to confirm the free excitonic nature of the lines observed at low temperature.

Finally, we can conclude that the supercritical fluids route allows the growth of high crystalline quality ZnO NCs covered by a thin layer of ZnO_2 atomic layers. In addition, the growing from an oxygen rich until unit cell favors the obtaining of oxygen vacancy free nanocrystals. The resulting optical properties are unique as only free excitonic emission and its phonon coupling replica are detected.